

Relative Sea- and Land- Level Change in Port Alberni, British Columbia Over the Last 700 Years

by
Louise Riou

B.Sc. (Hons.), Carleton University, 2020

Thesis Submitted in Partial Fulfillment of the
Requirements for the Degree of
Master of Science

in the
Department of Earth Sciences
Faculty of Science

© Louise Riou 2024
SIMON FRASER UNIVERSITY
Summer 2024

Copyright in this work is held by the author. Please ensure that any reproduction or re-use is done in accordance with the relevant national copyright legislation.

Declaration of Committee

Name: Louise Riou
Degree: Master of Science
Title: Relative Sea- and Land- Level Change in Port Alberni,
British Columbia Over the Last 700 Years

Committee: **Chair:** Gwenn Flowers
Professor, Earth Sciences

Jessica E. Pilarczyk
Supervisor
Associate Professor, Earth Sciences

Isabel Hong
Committee Member
Assistant Professor, Geography and the Environment
Villanova University

David Huntley
Committee Member
Research Scientist
Geological Survey of Canada

Andrea Hawkes
Committee Member
Professor, Earth and Ocean Sciences
University of North Carolina Wilmington

Michaela Spiske
Examiner
Researcher
State Museum of Natural History

Abstract

Sea-level change in Northern Cascadia is influenced by eustatic and tectonic processes. Tectonic processes from the Cascadia Subduction Zone are a major driving force of instantaneous and gradual sea-level change along Vancouver Island due to coseismic/interseismic (subsidence/uplift) periods. In this thesis, I use marsh stratigraphy, microfossils, and a Bayesian framework to reconstruct a 700-year-long record of relative sea-level change at Port Alberni, British Columbia, Canada. Results of a Bayesian Transfer function show that relative sea-level rose by 0.59 ± 0.35 mm/year over the past 700 years. Captured within this temporal range is the 1700 C.E. earthquake, and a second event between 1340 and 1402 C.E. which is only correlatable across Northern Cascadia, and that contributed to 42 ± 22 cm of coseismic and, or interseismic subsidence. These findings provide further evidence that Northern Cascadia is susceptible to both full-margin and partial ruptures, and shorter seismic reoccurrence intervals than previously estimated.

Keywords: Cascadia Subduction Zone; Salt Marsh; Foraminifera; Bayesian Transfer Function; Bayesian Age-depth Model; Relative Sea-level

Acknowledgements

I would first like to share my gratitude to the *cišaaʔath* (Tseshaht First Nation) who welcomed me as a guest on their lands. Allowing me to learn your natural history is a gesture for which I am very grateful.

A big thanks to my supervisor, Dr. Jessica Pilarczyk, for presenting me with the challenge this master's project. Your guidance, support, and encouragement have made these packed years unforgettable. The ambitions you have for me are remarkable, and the opportunities you have offered never imagined when I first started this journey. I will always remember the exciting moments we shared retrieving core sediments from Loon Jazz and the resulting relative sea-level reconstructions. You have been a major figure in forming the curious micropaleontologist that I am today.

Thanks to Dr. David Huntley, Dr. Isabel Hong, Dr. Andrew Kemp, Dr. Andrea Hawkes, Dr. Niamh Cahill, Dr. Carrie Garrison-Laney, Mr. Roger Macleod, and the many other researchers who offered their time, patience, and knowledge. This project would not have been possible without your collaborative efforts and mentorship. Each one of you have taught me to think more critically and have shaped me into a better scientist.

To the graduate students in Earth Sciences (Ariel, Katie, and Lea), the Coastal Hazard Research Lab (Anthony, Ayla, Stephen, and Brandon), the Teaching Support Staff Union (TSSU), and the friends I have made in Vancouver, thank you for being such a welcoming community. The many talks by the hammer and outings have helped me keep my head up during this rollercoaster ride. Meeting you all have made my move Vancouver memorable.

Thanks to my academic twin, Anthony Giang, who was always there for me. There is no one I would rather go through this journey than with you.

Most of all, thanks to my parents and my sister Geneviève for the emotional support. You always offer a positive outlook and tell me that I can achieve anything I set my mind to.

Table of Contents

Declaration of Committee	ii
Abstract	iii
Acknowledgements	iv
Table of Contents	v
List of Tables.....	vii
List of Figures	viii
List of Acronyms.....	xi
Chapter 1. Introduction	1
1.1. Subduction Zone Earthquakes	1
1.2. Cascadia Subduction Zone	1
1.3. Evidence of CSZ Paleearthquakes.....	4
1.4. Reconstructing Paleearthquakes from Records of Relative Sea-Level Change	5
1.5. Foraminifera as Sea-level Indicators	8
1.6. Thesis Motivation and Objectives	12
1.7. Thesis Structure.....	13
Chapter 2. Relative Sea-Level Change Over the Past 700 Years from Port Alberni, British Columbia (Canada): Implications for Cascadia Earthquakes and Associated Vertical Land Movement	15
2.1. Abstract	15
2.2. Introduction	16
2.3. Study Site	19
2.4. Methods.....	22
2.4.1. Field Sampling and Data Collection	22
2.4.2. Proxy Analysis of Surface Sediment Samples	25
Microfossil analysis	25
Loss-on-Ignition.....	26
Statistical Analyses of Modern Assemblages	26
2.4.3. Proxy Analysis and Chronology of Sediment Cores	27
2.5. Reconstructing Relative Sea-Level	29
2.5.1. Development of the Local Port Alberni Modern Training Set and Update to the Cascadia Regional Dataset	29
2.5.2. Relative Sea-Level Reconstruction	30
2.6. Results.....	32
2.6.1. Surface Distributions Within the Tidal Frame	32
Transect 1 (PA1).....	32
Transect 2 (PA2).....	33
Transect 3 (PA3).....	34
2.6.2. Species Flexible Response Curves	35
2.6.3. PAM Analysis	41
2.6.4. DCA Analysis	42
2.6.5. Port Alberni Marsh Stratigraphy	42

2.6.6.	Fossil assemblages	43
2.6.7.	Loss-on-ignition	45
2.6.8.	Chronology and Age-depth Model.....	45
2.6.9.	Variations in Transfer Functions.....	46
	Subsidence Estimates for Sand 2	48
	Subsidence Estimates for Sand 1	49
2.6.10.	Relative Sea-Level and Rates of Change	51
2.7.	Discussion	53
2.7.1.	Modern Microfossil Distributions: Local and Regional Training Sets.....	53
	Cascadia 2 Regional Training Set.....	53
	Local Training Set for Port Alberni	54
2.7.2.	Evidence for paleotsunamis and abrupt land-level change	59
	The 1964 Alaska and 1700 C.E. earthquakes	59
	Stratigraphic evidence for an earthquake and tsunami ~600 years ago	60
	Implications for understanding source mechanisms of Cascadia earthquakes.....	61
	Competing interpretations of the mud layer overlying Sand 1	64
2.7.3.	Relative Sea-level Rise at Port Alberni Over the Last Few Centuries	66
2.8.	Conclusions	67
Chapter 3.	Conclusions and Future Work	70
3.1.	Conclusions	70
3.2.	Future work	73
	References	76
Appendix A.	Supporting Information for Chapter 2	93
Appendix B.	Supporting Code.....	118

List of Tables

Table 2.1.	Model inputs and priors for the Bacon age-depth model for C1.....	28
Table 2.2.	Data for AMS radiocarbon age samples for C1 Port Alberni Marsh.	46
Table 2.3.	Calculated subsidence estimates based on local (Port Alberni) and regional (Cascadia 2) training sets with and without prior information.....	49

List of Figures

- Figure 1.1. Broadscale tectonics of the Cascadia Subduction Zone (CSZ). The Juan de Fuca Plate subducts beneath the North American plate along the Pacific Northwest (PNW) coast of North America from British Columbia to Northern California at an average rate of 40-45 mm/year, causing shortening and upwarping to the North American Plate. The convergence of the two plates along this boundary has resulted in at least 19 earthquakes over the past 10 kyr as revealed by geologic investigations. Thesis field site location in Port Alberni, British Columbia is indicated by a red dot. 4
- Figure 1.2. Geologic evidence of earthquakes preserved in salt marsh stratigraphy. (a) Interseismic period of an earthquake where deciduous trees grow in the upland outside of the tidal frame. (b) Coseismic subsidence resulting from large subduction zone earthquakes often results in vertical movement of coastal areas. (c) The earthquake record at the Niawiakum River in Washington after the 1700 C.E. earthquake. Drowned tree trunks are buried by intertidal mud as a result of coseismic subsidence..... 7
- Figure 1.3. The use of transfer functions to reconstruct past sea levels. (a) A training set is created using assemblages of modern foraminifera (relative abundance), field observations of plant vegetation, and tidal elevation along a transect (mean higher high water (MHHW), mean tide level (MTL), and mean lower low level (MLLW)). (b) Numerical techniques are used to determine the optimal elevation range of tidal inundation for each species of foraminifera within the marsh. (c) Fossil foraminifera (relative abundance) found in sediment cores and the transfer function used to reconstruct past sea level through the length of the core. The example shows a core containing sand (yellow), subsidence (grey) and post-earthquake peat (brown). 11
- Figure 2.1. (a) Plate tectonic setting of the Cascadia subduction zone (CSZ). The CSZ extends from Northern, Central and Southern Cascadia (white dotted line) Previous sea/land reconstructions reported in Kemp et al. (2018) are represented by a purple dot. Location of the study site (yellow dot) on Vancouver Island in British Columbia, Canada (red bounding box) is indicated. (b) Broadscale geomorphology of the area surrounding Port Alberni (yellow bounding box) located at the inland terminus of the 78 km long Alberni Inlet. (c) Zoomed in view of the Somass Estuary, including the Port Alberni Marsh showing locations of transects 1 to 3 relative to marsh geomorphology. 22
- Figure 2.2. Drone images and ground-level photographs of the Port Alberni Marsh study area. (a) Position of the landward terminus of the Alberni Inlet showing marsh development on the northern, southern, and eastern edges of the inlet. The location of surface transects 1 (b), 2 (c), 3 (d), and Core 2 (e) are indicated relative to vertical zonation within the marsh from the tidal flat to the upland environment. (f) High marsh to upland transition as revealed by marsh plant vegetation (white dashed lines). (g) Tidal flat to low marsh transition based on marsh vegetation and the abrupt change from minerogenic (tidal flat) and organic (low marsh) sediment composition. 24
- Figure 2.3. Species response curves (taxa-elevation relationship) for the six dominant species of foraminifera as predicted by the BTF using the local Port Alberni (red circles) and updated regional *Cascadia* 2 (blue dots) training sets relative to elevation

	(SWLI). The mean model is shown in the solid red line and the 95% credible intervals is shown as the grey shaded area.	36
Figure 2.4.	Microfossil (foraminifera and testate amoebae) and organic content for 18 stations along Transect 1 (PA1). (a) Relative abundances of microfossils and organic content relative to elevation (m MTL and SWLI) increasing distance inland (m) within the marsh. Tidal flat, low marsh, high marsh, and upland subenvironments are indicated and based on observed plant vegetation. (b) Results of partitioning around medoids (PAM) cluster analysis indicating that the optimal number of clusters (blue dotted line) is 3 based on the scenario with the highest average silhouette width. (c) Corresponding PAM clusters based on microfossil data. The average silhouette width is indicated by a grey dashed line. (d) Detrended correspondence analysis (DCA) showing associations between sample stations and microfossil species relative to tidal flat, low marsh, and upland clusters.	38
Figure 2.5.	Microfossil (foraminifera and testate amoebae) and organic content for 11 stations along Transect 2 (PA2). (a) Relative abundances of microfossils and organic content relative to elevation (m MTL and SWLI) increasing distance inland (m) within the marsh. Tidal flat, low marsh, and high marsh subenvironments are indicated and base on observed plant vegetation. (b) Results of partitioning around medoids (PAM) cluster analysis indicating that the optimal number of clusters (blue dotted line) is 2 based on the scenario with the highest average silhouette width. (c) Corresponding PAM clusters based on microfossil data. The average silhouette width is indicated by a grey dashed line. (d) Detrended correspondence analysis (DCA) showing associations between sample stations and microfossil species relative to tidal flat and high marsh clusters. ...	39
Figure 2.6.	Microfossil (foraminifera and testate amoebae) and organic content for 10 stations along Transect 3 (PA3). (a) Relative abundances of microfossils and organic content relative to elevation (m MTL and SWLI) increasing distance inland (m) within the marsh. Tidal flat, low marsh, and high marsh subenvironments are indicated and base on observed plant vegetation. (b) Results of partitioning around medoids (PAM) cluster analysis indicating that the optimal number of clusters (blue dotted line) is 3 based on the scenario with the highest average silhouette width. (c) Corresponding PAM clusters based on microfossil data. The average silhouette width is indicated by a grey dashed line. (d) Detrended correspondence analysis (DCA) showing associations between sample stations and microfossil species relative to tidal flat, low marsh and high marsh clusters.	41
Figure 2.7.	(a) Port Alberni Marsh stratigraphy. Correlated stratigraphic units along an east-west (a) and northeast-northwest (b) transect. Optical images and corresponding stratigraphic log based on Troels-Smith classification of eight cores collected along both transects. Black boxes show radiocarbon sampling location and calibrated ages in calendar years. Elevation are relative to MTL, m. (c) Inset map of the study area in Port Alberni indicating core transect 1 (pink dashed line) and core transect 2 (purple dashed line).	45
Figure 2.8.	Multiple predicted paleommarsh reconstructions based on the BTF using informative priors (a) and no priors (b) for the local (Port Alberni; red dots) and regional (<i>Cascadia 2</i> ; purple dots) foraminifera training sets (Fig. 2.9e).	48
Figure 2.9.	(a) Photograph and corresponding stratigraphic long for C1. (b) Relative abundance (%) of foraminifera and testate amoebae and (c) organic content. (d)	

Bacon age-depth model based on 12 radiocarbon samples from C1 (Fig. 2.7a). (e) Modelled paleommarsh elevation derived from an informed BTF. Backs dots indicate the tidal elevation expressed in SWLI (standarized water level index) with corresponding uncertainties. Coloured arrows indicate subsidence estimates for four possible subsidence scenarios. 50

Figure 2.10. RESLR relative sea-level modelling of (a) raw data of Port Alberni (black dots) with 1 sigma error (black box) and outlier data (pink dot) with 1 sigma error (pink box). (b) Relative sea-level (m) using the Errors in variable integrated Gaussian process model over the last ~700 years (C.E.). (c) Plot of yearly rate of relative sea-level change (mm per year) with posterior fit in solid green line and 95% credible interval in light green shading. 52

List of Acronyms

BTF	Bayesian Transfer Function
C.E.	Common Era
CSZ	Cascadia Subduction Zone
DCA	Detrended Correspondence Analysis
GIA	Glacio-isostatic Adjustment
GNSS	Global Navigation Satellite System
HOF	Highest Occurrence of Foraminifera
LOI	Loss-On-Ignition
LOT	Lowest Occurrence of Testate
MHHW	Mean Higher High Water
MLLW	Mean Lower Low Water
MTL	Mean Tide Level
NOSAMS	National Ocean Sciences Accelerator Mass Spectrometry
PAM	Partitioning Around Medoids
PNW	Pacific Northwest
RSL	Relative sea-level
RTK	Real-Time Kinematic
SWLI	Standard Water Level Index

Chapter 1.

Introduction

1.1. Subduction Zone Earthquakes

Subduction zone earthquakes of magnitude 8 and higher are known to produce some of the most destructive natural hazards. Their impacts, including strong shaking, tsunami inundation, subsidence, landslides, and liquefaction are especially detrimental to coastal communities facing subduction zones; often resulting in loss of life, damage to critical infrastructure, and subsequent economic losses (Ao et al., 2021). Recent subduction zone earthquakes and their resulting tsunamis that wreaked havoc in major cities include those occurring in Chile (1960), Alaska (1964), the Indian Ocean (2004), and Japan (2011). The Chilean earthquake was one of the most powerful earthquakes recorded in human history (9.5 M_w) and caused a portion of the city of Valdivia to subside by 2.2 m, exposing it to significant marine inundation (Kanamori, 1977; Aguirre, 2018). The impacts of the 2004 Indian Ocean earthquake (M_w 9.1) include more than 230,000 fatalities (Ghobara et al., 2006; Shibayama., 2015). Lastly, the 2011 Tohoku earthquake of M_w 9 generated a tsunami with a maximum wave height of 40 m that inundated more than 5 km inland (Mori et al., 2011). These recent subduction zone earthquakes, all of which caught the world by surprise, highlight the importance of fully understanding seismic hazards (i.e., frequency, magnitude, areas impacted) so that coastal communities may prepare for future events.

1.2. Cascadia Subduction Zone

The Cascadia subduction zone (CSZ) is an active fault zone running almost parallel to the Pacific Northwest (PNW) coast of North America and is home to 23 million people from southern British Columbia, Canada to northern California, USA (U.S. Census Bureau, 2022; Statistics Canada, 2023). Along the CSZ, the Juan de Fuca Plate subducts beneath the North American Plate, resulting in interseismic uplift along with consequent crustal

shortening and upwarping at a rate of 40-45 mm/yr (Leonard et al., 2004; DeMets et al., 2010). The CSZ can be thought of as having three distinct regions: a Northern part (the Explorer plate and Northern portion of the Juan de Fuca Plate, from British Columbia to Northern Washington); a Central part (Central to Southern Juan de Fuca Plate, from Southern Washington to Northern Oregon); and a Southern part (Southern Juan de Fuca Plate to the Gorda Plate, in Northern California). The plates are locked in the Central part (with decreasing locking in the Northern and Southern sectors), and strain is accumulating along the fault zone (Fig. 1.1) (Leonard et al., 2004).

Plate boundary processes along subduction zones can be grouped into two broad phases that constitute a full earthquake deformation cycle. The first phase, where strain accumulates along a fault, is known as an interseismic period and lasts approximately 550 years in Cascadia (Walton et al., 2021). The second phase, the earthquake or coseismic phase, occurs when strain is instantaneously released, and the Earth's crust coseismically uplifts or subsides depending on distance from the rupture area. Coseismic slip is the sudden release of energy when plates slip, producing vertical displacement of the crust. The amount of vertical displacement (i.e., subsidence) along the coast can be recognized in coastal stratigraphy, and by the submergence of salt marshes and drowned coastal forests (Atwater, 1987; Dragert et al., 1994; Flück et al., 1997). The amount of coseismic slip during rupture relates to the earthquake magnitude and used to assess future seismic hazards in a region (Leonard et al., 2004).

Throughout the Holocene, there have been at least 19 great earthquakes (i.e., $>M_w$ 7) along the CSZ, with the last occurring in 1700 C.E. (Atwater, 1987; Walton et al., 2021). Geologic evidence of coseismic subsidence provides insight into the magnitude, recurrence interval, and rupture patterns of subduction zone earthquakes (e.g., Darienzo et al., 1994; Guilbault et al., 1995; 1996; Atwater & Hemphill-Haley, 1997; Nelson et al., 2008; Hawkes et al., 2010; 2011; Engelhart et al., 2013; Kemp et al., 2018; Padgett et al., 2022). Coastal marshes of the PNW record geological, geomorphological, and microfossil evidence of recurrent plate-boundary earthquakes, tsunamis, and associated coseismic subsidence over the last 10,000 years (10 kyr) (i.e., Atwater, 1987; Nelson et al., 2008; Hawkes et al., 2011; Nelson et al., 2021). However, the range of plate boundary processes

occurring along the CSZ remains unclear, particularly regarding whether large full-margin earthquakes are generated, or whether shorter sections of the CSZ can produce smaller Mw 8.0-8.7 earthquakes (Frankel et al., 2015; Melgar, 2021; Walton et al., 2021).

Additionally, most earthquake evidence is concentrated in the Central and Southern regions of Cascadia (i.e., Atwater, 1987; Hawkes et al., 2010, 2011; Kemp et al., 2018; Melgar, 2021; Walton et al., 2021; Padgett et al., 2022). Although limited in number, studies focusing on the Northern part of the CSZ document evidence for earthquakes and tsunamis on Vancouver Island. Previous ground-breaking research (e.g., Clague and Bobrowsky, 1993; 1994a; 1994b; Guilbault et al., 1995; 1996; Hutchinson and Clague, 2017) quantified coseismic subsidence and identified evidence for tsunami inundation on Vancouver Island, helping to expand the spatial and temporal extent of past earthquakes. The limited number of studies in Northern Cascadia quantifying coseismic subsidence hinders the accuracy of dynamic rupture (earthquake) models and inhibits a full examination of the extent of plate boundary processes (Wang et al., 2013). The northern spatial gap also hinders a complete understanding whether Cascadia produces only full-trench ruptures along the entire fault. These questions cannot be resolved without additional research in the Northern part of Cascadia to better constrain the age, timing, and intensity of these great earthquake events (Hutchinson and Clague, 2021; Walton et al., 2021).

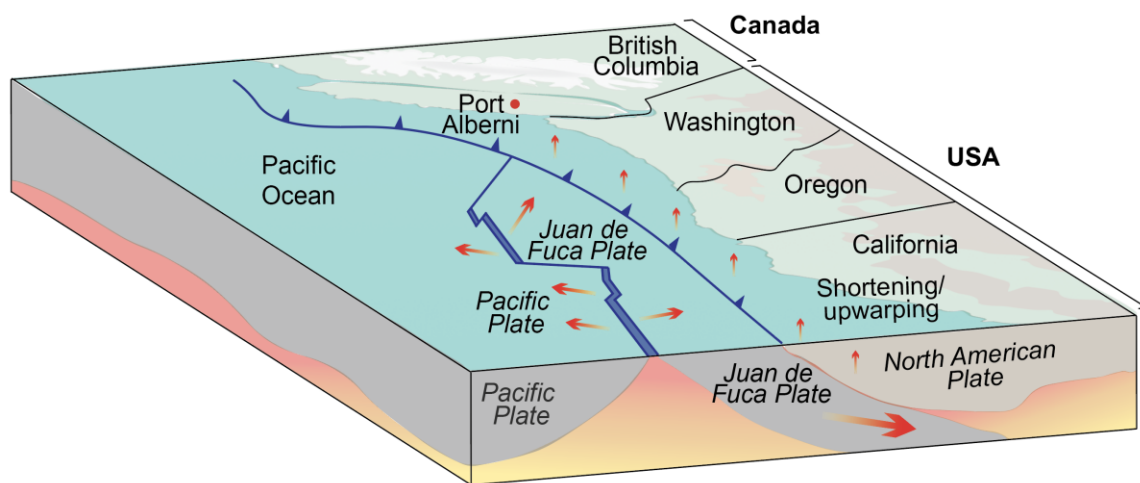


Figure 1.1. Broadscale tectonics of the Cascadia Subduction Zone (CSZ). The Juan de Fuca Plate subducts beneath the North American plate along the Pacific Northwest (PNW) coast of North America from British Columbia to Northern California at an average rate of 40-45 mm/year, causing shortening and upwarping to the North American Plate. The convergence of the two plates along this boundary has resulted in at least 19 earthquakes over the past 10 kyr as revealed by geologic investigations. Thesis field site location in Port Alberni, British Columbia is indicated by a red dot.

1.3. Evidence of CSZ Paleearthquakes

Along the PNW coast, historical narratives of indigenous people encountering great earthquakes and tsunamis are recorded in oral tradition (McMillan & Hutchinson, 2002). These indigenous oral traditions, the cultural practice of their perception of the world, are told as a way of passing on environmental events impacting the areas in which they live (McMillan & Hutchinson, 2002). Some of their stories provide insight into collective experiences related to various seismic events. The story of “Earth Quake Foot” is an example of an oral history told by one of the many coastal Indigenous groups that has led to improved understanding of the region’s earthquake history (McMillan & Hutchinson, 2002). Occupying the western portion of Vancouver Island, the Nuu-chah-nulth believe the mountain dwarves are responsible for sudden and intense ground shaking. Every time these dwarfs fall against drums, they became ill with the “earthquake foot” disease, and their stomping around causes the ground to shake.

Conventional scientific methods of recognizing paleoearthquakes along the PNW include using geologic evidence preserved along coasts that record sudden land-level change (i.e., coseismic subsidence) and tsunami inundation. Coastal salt marsh environments capture, particularly well, the occurrence of interseismic and coseismic periods of past earthquakes (Atwater, 1987). A typical earthquake sequence in a salt marsh generally appears as an organic-rich peat abruptly overlain by tsunami sand, followed by tidal mud resulting from rapid relative sea-level (RSL) rise (Atwater, 1987; Clague and Bobrowsky, 1994b). Researchers identify salt marshes impacted by earthquake subsidence and tsunami inundation by interpreting abrupt land-level changes from repeated peat-sand-

mud sequences in stratigraphic records (Atwater, 1987; Darienzo et al., 1994; Atwater and Hemphill-Haley, 1997).

Combining indigenous oral histories and geologic evidence improves our knowledge of the paleoearthquake history (i.e., earthquakes and tsunamis that predate the historical record) of a given region (Atwater, 1987; Satake and Atwater, 2007; Sawai, 2020). Understanding the patterns of tsunami inundation and coseismic subsidence is important because modellers use geologic evidence (e.g., thicknesses and volumes of tsunami sands and coseismic deformation) to model rupture styles (e.g., Leonard et al., 2004; Leonard et al., 2010; Wang et al., 2013; Melgar 2021). Older models predicted uniform slip along the Cascadia fault based on limited geologic evidence and large uncertainties were (Wang et al., 2013). In recent decades, the quantity, spatial extent, and availability of high-resolution geologic evidence generates realistic rupture models for Cascadia that explain the available lithologic, stratigraphic, chronologic, and microfossil evidence. Currently, the geologic evidence best supports a heterogenous rupture (Wang et al., 2013), or a sequence of ruptures along the CSZ (Melgar, 2021). It is important to determine the most plausible rupture model(s) for Cascadia since these will influence how hazard maps, tsunami risk-reduction plans, and seismic assessments are generated for a region, and will determine how coastal communities are prepared for future earthquake and tsunami hazards (Witter et al., 2013; Hutchinson and Clague, 2017; Melgar 2021).

1.4. Reconstructing Paleearthquakes from Records of Relative Sea-Level Change

Sequences of peat overlain by sand and mud preserved in salt marshes provide evidence for coseismic subsidence along the coast during tsunami inundation (Atwater, 1987; Atwater and Hemphill-Haley., 1997; Clague et al., 2000; Nelson et al., 2008). Coseismic subsidence causes a sudden drop in land elevation, resulting in instantaneous sea-level rise (Fig. 1.2a-b). Following the sudden sea-level rise of the coseismic period, the interseismic period allows marshes to gradually rebound from low elevation tidal flat muds to higher elevation intertidal peats. This rebuilding causes RSL to gradually fall (Nelson et

al., 1996; Guilbault et al., 1995; 1996). An example of an area impacted by earthquake-induced land-level change after the 1700 C.E. CSZ earthquake is Niawiakum River in Washington State (Fig. 1.2c). Here, freshwater forests found at elevations higher than the tidal frame were instantaneously lowered in elevation. Trees drowned and were subsequently killed by prolonged tidal inundation. Coseismic subsidence at the Niawiakum River resulted in a near instantaneous environmental change that was captured in the sedimentology and stratigraphy, by dead tree stumps buried in tidal mud, and a gradual RSL fall marking the re-establishment of marsh formation during the most recent interseismic interval.

The amount of land-level change (coseismic subsidence) during an earthquake can be quantified by reconstructing RSL (e.g., Guilbault et al., 1995,1996; Hawkes et al., 2010, 2011; Wang et al., 2013; Kemp et al., 2018; Nelson et al., 2020; Padgett et al., 2021). RSL reconstructions are used to delimit areas prone to subsidence during earthquakes (e.g., Atwater, 1987; Guilbault et al., 1995,1996), and to determine the recurrence intervals along the CSZ (e.g., Nelson et al., 2007; Nelson et al., 2020; Padgett et al., 2022). These RSL reconstructions are important since they determine the hazard potential in areas that are poorly constrained by earthquake models, such as Northern Cascadia (Leonard et al., 2010; Wang et al., 2013; Melgar 2021).

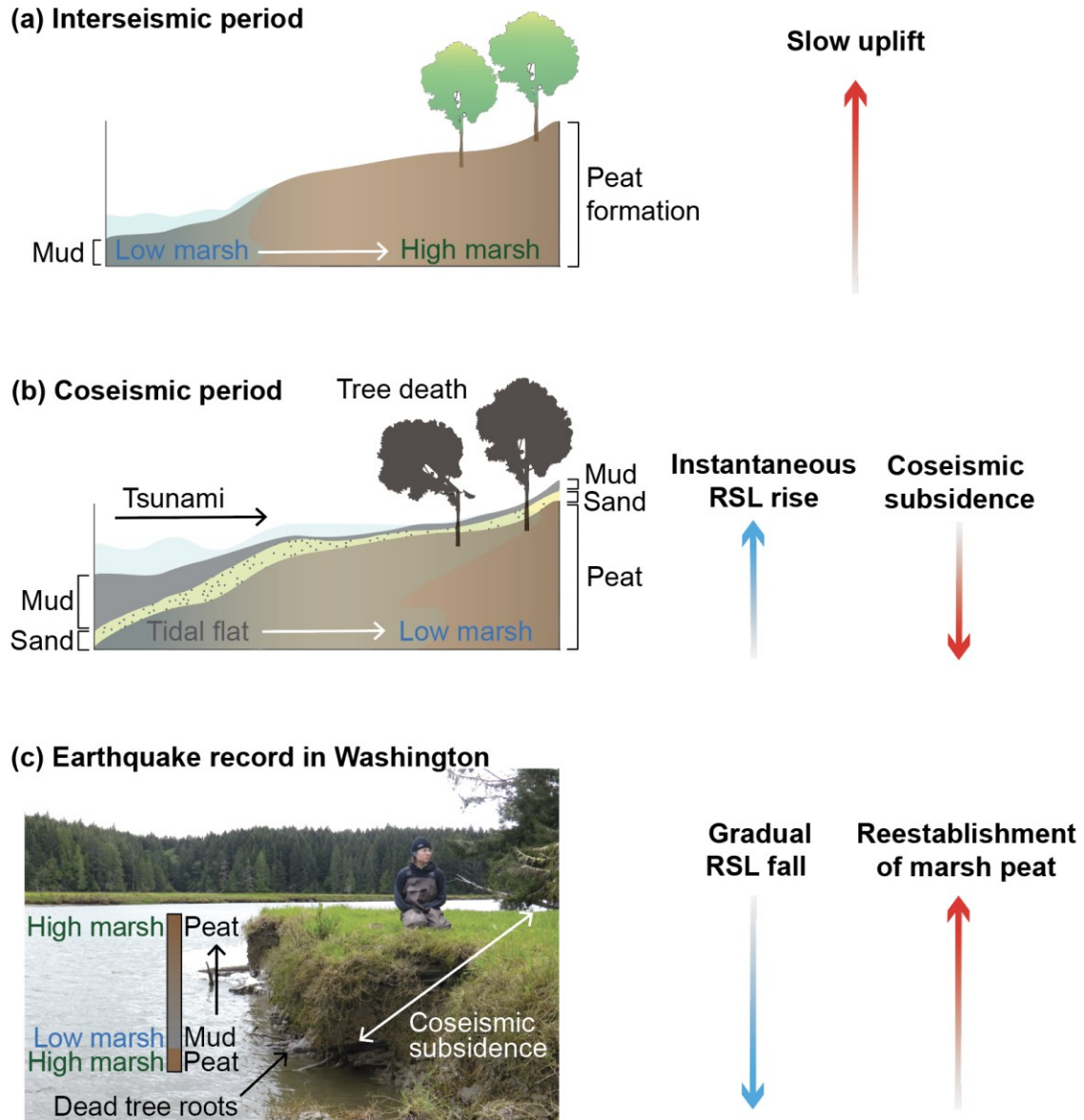


Figure 1.2. Geologic evidence of earthquakes preserved in salt marsh stratigraphy. (a) Interseismic period of an earthquake where deciduous trees grow in the upland outside of the tidal frame. (b) Coseismic subsidence resulting from large subduction zone earthquakes often results in vertical movement of coastal areas. (c) The earthquake record at the Niawiakum River in Washington after the 1700 C.E. earthquake. Drowned tree trunks are buried by intertidal mud as a result of coseismic subsidence.

1.5. Foraminifera as Sea-level Indicators

Holocene sea-level reconstructions document trends in past change in a variety of coastal environments, including estuaries, coastal lakes, salt marshes, and inlets (Lamb et al., 2006). The use of proxies, including those that are biological (pollen, microfossils, macrofossils, plants), chemical (loss-on-ignition, stable carbon isotope), and physical (archeological, grain size), are used to better understand past local and regional sea-level trends. For example, diatoms (a biological proxy) have been used to infer changes from marine to freshwater environments within coastal marshes (Palmer and Abbott, 1986; Plassche, 1986; Cooper et al., 2010). Chemical proxies, such as stable carbon isotopes, have been used to differentiate between C₃ and C₄ plants with a relationship to the tidal frame (Chmura and Aharon, 1995; Kemp et al., 2012). Lastly, physical proxies, such as grain size and lithologic composition, have been used to understand the type and energy of depositional processes impacting coastal environments (Shennan et al., 2015). The wide range of available sea-level proxies have been shown to be extremely important in answering specific questions to better inform us about future trends, including changes in RSL resulting from megathrust earthquakes (Atwater, 1987; Nelson et al., 1996).

One microfossil group widely used in sea-level research are foraminifera, common microfossils that are typically abundant in marine and coastal ecosystems (Murray, 1991; Scott et al., 2001). Foraminifera are single-celled amoeboid protozoans found in a range of environments from brackish to marine settings (Shennan et al., 2015). Their soft amoeboid bodies are protected by a test (shell) that is either secreted with a carbonate, organic, or siliceous composition by the organism (autogenous test) or built by the agglutination of materials in their surrounding environment (zenogenous test) (Chien et al., 2018). Foraminifera typically range in size from 50 μm to 1 mm in length, making them useful for coring studies where sample sizes are small, but foraminifera concentrations are abundant (Shennan et al., 2015). Foraminifera are especially useful for paleoenvironmental reconstructions as they are: (1) found in high concentrations; (2) rapid reproducers; (3) well-preserved in the geological record; and (4) sensitive to various environmental changes (i.e., salinity, elevation, and temperature) (De Rijk, 1995; Patterson et al., 1995). Testate amoebae, a freshwater biological proxy, have been used to complement foraminiferal

analysis to delineate between saline and freshwater environments (Scott and Medioli, 1980). Inclusion of a freshwater indicator, such as testate amoebae, in a modern training set extends the elevation range and the threshold of microfossils as a proxy. This is important because it determines the highest level of occurrence of foraminifera inhabiting the marsh while determining where the freshwater environment begins. It is easy to incorporate a testate amoebae count into the training set as sample preparation methods are identical to those used to analyse foraminifera.

The application of foraminifera counts in sea level research dates to the 1970's with pioneering work by Scott and Medioli (1978; 1986) and Scott et al. (1980; 1981), who were the first to document how foraminifera zonate vertically within salt marsh environments. The work of Scott and Medioli (1978; 1986) revealed distinct foraminiferal zones within marshes and determined that they were controlled by elevation relative to tides, making foraminifera useful indicators of past RSL. In general, Scott and Medioli (1978) found that calcareous tests were common at low elevations and unvegetated areas, whereas agglutinated tests were found in the more densely vegetated high elevation sections of the marsh. Specifically, they found the species *Balticammina pseudomacrescens*, *Haplophragmoides wilberi* and *Trochammina inflata* inhabited the upland to middle marsh, while *Miliammina fusca* inhabited the low marsh to tidal flat zone. Similar findings have been documented along the CSZ (Patterson et al., 1999; Hawkes et al., 2010; Milker et al., 2015), the Canadian and United States Atlantic seaboard (Scott and Medioli, 1978; Kemp et al., 2012; Kemp et al., 2013), United Kingdom (Horton and Edwards, 2006), and Australia (Horton et al., 2003) (Fig. 1.3a).

The relationship between foraminiferal assemblages and elevation has made this microfossil group a robust biological tool for estimating coseismic subsidence along the CSZ (Atwater and Hemphill-Haley, 1997). In the last three decades, foraminiferal research has expanded to incorporate mathematical transfer functions that reconstruct RSL more precisely (e.g., Kemp et al., 2018). Modern surface sediment samples containing foraminifera are collected at different elevations along a surface transect spanning the unvegetated tidal flat through to the low marsh, high marsh, upland, and freshwater environments (Fig. 1.3a). Modern salt marsh foraminifera assemblages and elevation

measurements related to tides form a modern training set. In order to resolve changes in sea level through time, transfer functions use the modern training set (comprising foraminifera, testate amoebae, and elevation) to statistically relate foraminifera to their analogous fossil record found in sediment cores (e.g., Guilbault et al., 1994; Milker et al., 2016; Kemp et al., 2018; Cahill et al., 2016; Nelson et al., 2020). Transfer functions allow for a continuous record of sea-level change that, in coastal locations such as Cascadia, may capture full earthquake cycles (Hawkes et al., 2011) (Fig. 1.3).

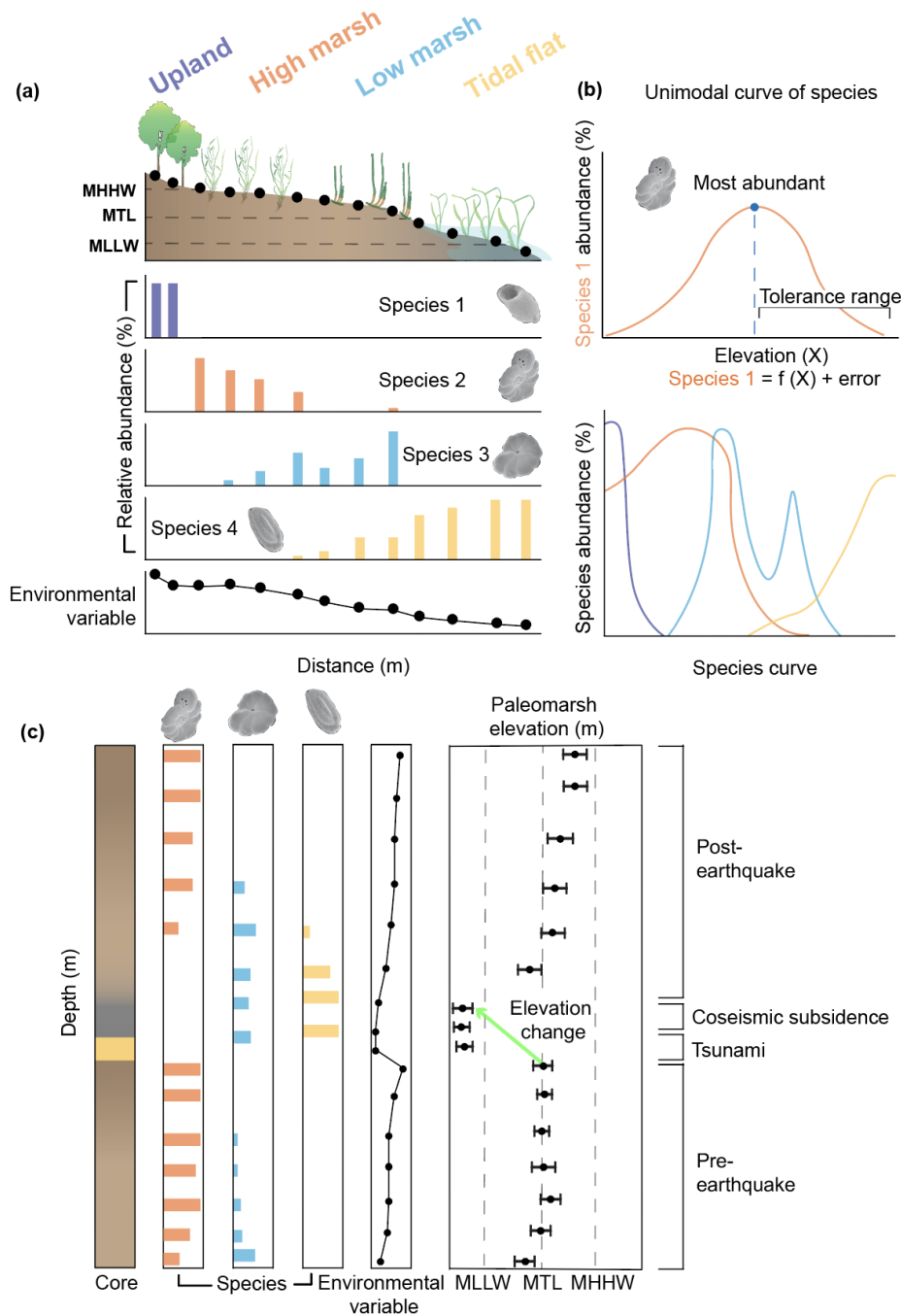


Figure 1.3. The use of transfer functions to reconstruct past sea levels. (a) A training set is created using assemblages of modern foraminifera (relative abundance), field observations of plant vegetation, and tidal elevation along a transect (mean higher high water (MHHW), mean tide level (MTL), and mean lower low level (MLLW)). (b) Numerical techniques are used to determine the optimal elevation range of tidal inundation for each species of foraminifera within the marsh. (c) Fossil foraminifera (relative abundance) found in sediment cores and the transfer function used to reconstruct past sea level through the length of the core. The example shows a core containing sand (yellow), subsidence (grey) and post-earthquake peat (brown).

1.6. Thesis Motivation and Objectives

In Cascadia, a long-term record of paleoearthquakes recorded in oral histories and the geologic record offers context for understanding the seismic potential in areas of interest. Paleogeographic reconstructions invoking a rapid RSL rise from coseismic subsidence are used in rupture models inferring slip variations along the fault zone. Unfortunately, the distribution of sea-level reconstructions used in these rupture models is not uniform throughout Cascadia, with the majority concentrated in Central and Southern Cascadia. The limited number of studies along the Northern part of the CSZ (offshore Vancouver Island) inhibits a full examination of the extent of plate boundary processes accompanying subduction zone great earthquakes. The rupture extent of past CSZ earthquakes cannot be properly assessed without mapping and quantifying the distribution of coseismic subsidence.

The primary motivations for the thesis are to improve understanding of the spatial extent of coseismic subsidence from past CSZ earthquakes, and to better constrain the extent of rupture areas and characteristics of the earthquake such as magnitude, slip, and amount of coseismic subsidence or uplift. Improved spatial resolution of records from Northern Cascadia will enable researchers to address key questions related to Cascadia rupture styles, and whether the CSZ produces only full-trench ruptures along the entire fault system, or whether other plate boundary scenarios should be considered.

In this thesis, biological proxies (foraminifera and testate amoebae), stratigraphic information, loss-on-ignition, a Bayesian Transfer Function (BTF), and a Bayesian age-depth model are used to reconstruct a 700-year record of relative sea-level change in Port Alberni, British Columbia, Canada (Fig. 2.1). The research objectives are to: (1) determine if modern foraminifera and testate amoebae zonate along the Port Alberni Marsh, and if they can be used as analogs for RSL reconstructions; (2) resolve whether Port Alberni has previously experienced coseismic subsidence during past earthquakes, including the great 1700 C.E. and earlier events; and (3) establish a RSL history for Port Alberni.

This study provides improved understanding of the seismic hazard (magnitude and reoccurrence interval) for Vancouver Island, British Columbia, and Northern Cascadia. This research partly fills the spatial gap existing in current rupture models for all of Cascadia (Wang et al., 2013), leading to a better understand of the extent and plate boundary processes of the CSZ, and helps to validate the current full-trench rupture (Wang et al., 2013) and, or multi-rupture (Melgar, 2021) models of Cascadia.

1.7. Thesis Structure

The thesis is divided into 3 chapters. Chapter 1 provides a general background of Cascadia Subduction Zone plate boundary processes, evidence of Holocene paleoearthquakes along the PNW coast of North America, and methods for using foraminifera as a sea-level indicator that can be applied to assess estimates of coseismic subsidence and tsunami inundation.

Chapter 2 represents the main part of the thesis and is formatted as a manuscript for *Quaternary Science Reviews*, a long-format geosciences journal intended for a broad geosciences audience. In Chapter 2, a 700-year record of relative sea-level change is developed using intertidal foraminifera at Port Alberni, British Columbia, Canada. My research contributions include fieldwork sample collection (modern surface samples, core retrieving, vegetation identification), all laboratory work (stratigraphy description, microfossil analysis, loss-on-ignition, radiocarbon dating sampling), statistical analysis of the proxy data (partitioning around medoids and detrended correspondence analysis), development of the modern training set based on three transects, (Bacon) age-depth modeling, RSL modelling (RESLR), cartography, and writing.

The manuscript is co-authored with seven researchers. Jessica Pilarczyk (Simon Fraser University) served as my supervisor, helping with the conceptualization of project, assisting in fieldwork and some laboratory analyses, and editing the manuscript. Isabel Hong (Villanova University), committee member, assisted in fieldwork, including sample collection and salt marsh vegetation identification. David Huntley (Geological Survey of Canada), committee member, collected elevation data via a RTK global navigation satellite

system and total station theodolite, assisted in fieldwork, provided knowledge concerning the Quaternary history, geomorphology and sedimentology of Vancouver Island, and helped edit the manuscript. Niamh Cahill (Maynooth University), creator of the Cascadia foraminifera-based BTF, generated species response curves based on modern foraminiferal distributions and re-ran the Cascadia BTF using my microfossil results to reconstruct relative sea-level at Port Alberni. Andrew Kemp (Tufts University) assisted in the standardization of tidal datums, and elevations collected as part of this study, and provided guidance concerning priors used in the BTF and the RESLR package. Roger Macleod (Geological Survey of Canada) collected RTK elevation data, assisted in fieldwork, and provided boat access. Andrea Hawkes (University of North Carolina Wilmington), committee member, provided guidance regarding sampling strategy and methods. I would also like to acknowledge the following members from the Coastal Hazards Research Lab for their assistance: Anthony Giang (drone operator, sediment core retriever, and optical imaging of sediment cores), Stephen Bartlett (sediment core retriever), and Courtney Whitehead (loss-on-ignition for sediment core intervals).

My thesis concludes with Chapter 3, in which the main findings are summarized, outstanding research questions are formulated, and recommendations are suggested for future work on Vancouver Island and in the Northern part of CSZ.

Chapter 2.

Relative Sea-Level Change Over the Past 700 Years from Port Alberni, British Columbia (Canada): Implications for Cascadia Earthquakes and Associated Vertical Land Movement

2.1. Abstract

Sea-level change in Northern Cascadia is influenced by eustatic, isostatic, and tectonic processes. Tectonic processes originating from the Cascadia Subduction Zone are the major driving force of sea-level change along the west coast of Vancouver Island due to coseismic/interseismic (subsidence/uplift), which causes changes in relative sea-level along the coast. Here, a microfossil-based relative sea-level reconstruction for Port Alberni located on Vancouver Island (Canada) spanning the past 700 years is presented, based on an updated Cascadia foraminiferal training set that includes three additional modern transects from Northern Cascadia. The results of the reconstruction indicate that relative sea-level at Port Alberni increased by a mean rate of 0.57 ± 0.32 mm/year over the last 700 years, which is less than the global average of ~ 1 to 4 mm/year over the past century. Two tsunami deposits corresponding to the 1700 C.E. Cascadia earthquake, and an older event occurring sometime between 1340 and 1402 C.E., are recorded in the coastal stratigraphy of the salt marsh at this site, the latter of which is interpreted to be associated with 48 ± 22 cm of coseismic subsidence. This record complements a range of postglacial sea-level reconstructions from Northern Cascadia; however, it is among the few that captures centennial-scale variability.

Keywords: Cascadia subduction zone; Salt marsh; Foraminifera; Bayesian transfer function; Bayesian age-depth model; Relative sea-level

2.2. Introduction

Sea-level reconstructions from the Pacific Northwest (PNW) spanning the last ~20 kyr capture the onset of the Holocene, a warming interglacial climate, and isostatic adjustments resulting from the retreating Pleistocene Cordilleran Ice Sheet (Roe et al., 2013; McLaren et al., 2014; Shugar et al., 2014; Letham et al., 2024). However, short-lived climatic and environmental changes, such as the Medieval Climate Anomaly and Little Ice Age, occurring during the Common Era (i.e., 0 – 2000 C.E.) are often not captured in these sea-level records because they are often too coarse in resolution (e.g., Shugar et al., 2014; Letham et al., 2024). Sea-level reconstructions at the centennial and decadal timescale are particularly important as they capture abrupt changes in land-level associated with subduction zone earthquakes, including those occurring along the Cascadia Subduction Zone (CSZ) (Darienzo et al., 1994; Nelson et al., 1996; Hawkes et al., 2011).

Along the PNW coast of North America lies the CSZ, a 1000 km long megathrust fault that produces some of the greatest earthquakes, including the ~M 9.0 Cascadia earthquake in 1700 C.E. (Atwater, 1987, 1992; Darienzo & Peterson, 1990; Clague & Bobrowsky, 1994a; Guilbault et al., 1995; Nelson et al., 1996; Clague, 1997). Evidence for Holocene earthquakes found in salt marshes includes intertidal peat abruptly overlain by sand sheets and tidal mud (Darienzo and Peterson, 1990; Clague & Bobrowsky, 1994a; Clague et al., 1994a; Atwater et al., 1995). This stratigraphic sequence results when coseismic subsidence causes a lowering of the elevation of the marsh and a subsequent abrupt relative sea-level (RSL) rise (Atwater, 1987; Darienzo & Peterson, 1995; Guilbault et al., 1995).

Earthquake rupture models that incorporate coseismic subsidence estimates resulting from subduction zone earthquakes have been used to infer rupture slip behaviour, rheology, and recurrence intervals. Confidence in dynamic rupture models and understanding of plate boundary processes has improved by integrating geologic evidence from earthquakes and tsunamis that predate the historical record in locations such as Cascadia (Leonard et al., 2004; Wang et al., 2013; Luo & Wang, 2022), Alaska (Hamilton & Shennan, 2005; Briggs et al., 2014), Japan (Sawai et al., 2004; Pilarczyk et al., 2021),

Chile (Melnick et al., 2012; Wesson et al., 2015), and New Zealand (Cochran et al., 2006; Clark et al., 2019).

A great earthquake ($>M$ 8.0) has not occurred along the CSZ in over 300 years (Atwater, 2005). Evidence for the most recent earthquake in 1700 C.E. was captured by both indigenous oral traditions (McMillan & Hutchinson, 2002) and the geologic record (Atwater et al., 1987). Salt marshes adjacent to the CSZ, from Northern California (Padgett et al., 2021; 2022), Oregon (Jennings & Nelson, 1992; Hawkes et al., 2010, 2011; Engelhart et al., 2013; Nelson et al., 2020), Washington (Atwater, 1987, 1992; Atwater & Hemphill-Haley, 1997; Sabeau, 2004), and British Columbia (Clague & Bobrowsky, 1994a, 1994b; Guilbault et al., 1995, 1996; Peterson et al., 2013; Hutchinson & Clague, 2017; Goff et al., 2020; Tanigawa et al., 2022) reveal stratigraphic evidence for earthquakes and tsunamis occurring over the last \sim 8,000 years. Despite the wealth of earthquake reconstructions at many of these locations, spatial gaps exist where subsidence estimates associated with past earthquakes along the coast are lacking or are not quantified. One major spatial gap identified by Wang et al. (2013) is the Northern part of the subduction zone along western Vancouver Island in British Columbia. Here, the lack of high-resolution RSL reconstructions over the Common Era inhibits a full examination of the extent of plate boundary processes accompanying megathrust earthquakes.

The magnitude of coseismic subsidence associated with CSZ earthquakes on Vancouver Island (e.g., Clague and Bobrowsky, 1994a, 1994b; Guilbault et al., 1995, 1996; Benson et al., 1997; Clague et al., 2000) can be improved with numerical techniques (e.g., Bayesian Transfer Functions (BTF), Niamh et al., 2016) that estimate the amount of vertical land movement using biological proxies of RSL change (Kemp et al., 2018). The estimates of coseismic subsidence along a coastline are, in turn, used to validate the rupture models critical for a more complete understanding of recurrence intervals of different magnitude events, and hazard preparation for coastal communities in the PNW, and elsewhere around the Pacific Ocean basin (Wang et al., 2013; Peterson et al., 2014; Luo & Wang, 2022).

Foraminifera are some of the most widely used proxies for reconstructing Holocene RSL change from salt marsh sediments (Horton & Edwards, 2006; Barlow et al., 2013). Foraminifera are protists that are robust indicators of RSL because their assemblages respond to an elevation gradient within the tidal frame (Scott & Medioli, 1978; Scott & Medioli, 1980; Horton & Edwards, 2006; Edward and Wright, 2015). Modern assemblages of salt marsh foraminifera, which occupy distinct elevation zones within a marsh, can be linked to their fossil assemblages as analogues of former RSL (Scott and Medioli, 1978; Horton and Edwards, 2006; Edwards and Wright, 2015). The application of microfossils in empirically based transfer functions mathematically links modern foraminiferal distributions to their fossil assemblages in order to reconstruct RSL in many locations worldwide (e.g., Kemp et al., 2009; Walker et al., 2020; Williams et al., 2021; Garrett et al., 2023). BTFs are useful because they integrate prior information from associated environmental proxies and allow for non-unimodal species response curves, which assists in more accurately quantifying uncertainties, leading to more precise sea-level reconstructions (Niamh et al., 2016).

Within Cascadia, 19 training sets comprising modern foraminiferal distributions within salt marshes (Kemp et al., 2018) and 12 sea/land-level reconstructions have been completed, predominantly on coastlines facing the Central and Southern parts of the subduction zone (e.g., Hawkes et al., 2010, 2011; Nelson et al., 2020; Padgett et al., 2021). Only a small fraction of these training sets and corresponding sea/land-level reconstructions are from the Northern part of the CSZ facing Vancouver Island (Fig. 2.1) (Guilbault et al., 1995; 1996). Although there are several microfossil-based reconstructions of subsidence associated with the 1700 C.E. earthquake from coastal areas on Vancouver Island (Guilbault et al., 1995; 1996), up to 11 sand layers, which may represent paleoearthquakes and associated subsidence, have been documented in the region (Clague and Bobrowsky, 1994b; Hutchinson and Clague, 2017), have not been analysed using recent BTFs. The lack of detailed coseismic subsidence estimates for much of the Northern part of the CSZ leads to uncertainty surrounding the seismic hazard and questions about the extent of the rupture patch for great earthquakes, such as the 1700 C.E. event (Leonard et al., 2004, 2010; Wang et al., 2013; Kemp et al., 2018).

To investigate plate boundary processes in this region, we used a microfossil-based BTF to develop a 700-year RSL record at Port Alberni, British Columbia, Canada (Fig. 2.1). Port Alberni is the easternmost coastal city on the western side of Vancouver Island, and furthest from the trench. As such, this study area is well positioned to assess the maximum spatial extent of possible subsidence associated with CSZ ruptures. Improved knowledge at this location will assist in furthering understanding of important questions regarding the possibility of heterogenous (Wang et al., 2013) or multiple rupture sequences (Melgar, 2021) for the CSZ.

2.3. Study Site

The CSZ is a subduction zone consisting of a Northern (British Columbia to Northern Washington), Central (Southern Washington to Oregon) and Southern (Northern California) part (Fig. 2.1). The convergent boundary between the subducting Juan de Fuca and North American plates results in interseismic uplift of the crust, consisting of shortening and upwarping at an average rate of 40-45 mm/yr (DeMets et al., 2010). The CSZ has not experienced a M_w 9 earthquake since 1700 C.E., which has resulted in strain accumulation over the last ~324 years (Walton et al., 2021).

In Northern Cascadia, Vancouver Island's coastline is characterized by rocky headlands, fjords, and inlets (Jawanda, 1954). Salt marshes form in the low-lying and protected areas on the windward coastline but are often smaller and younger than salt marshes in Central and Southern Cascadia because of antecedent geomorphology and glacio-isostatic adjustment (GIA) (Dura et al., 2016). Despite differences in spatial and temporal extent, marshes in Northern Cascadia are similar to those elsewhere along the PNW coast in terms of distinct vegetation zones and their relationship to the frequency of tidal inundation (Pojar & Alaback, 1994). For example, the tidal flat, existing below mean tide level (MTL), is characterized by low densities of the aquatic plant *Zostera* spp. (Pojar & Alaback, 1994). Sections of the salt marsh between MTL and mean higher high water (MHHW) are commonly composed of higher density stands of vascular plants including *Juncus balticus*, *Carex lyngbyei*, *Potentilla pacifica*, *Distichlis spicata*, and *Salicornia* spp.

(Pojar & Alaback, 1994). The uplands, the zone with the highest elevation, includes freshwater coniferous and deciduous trees and shrubs, such as alders, cedars, pines, and spruces (Parish & Thomson, 1994; Pojar & Alaback, 1994; Hughes & Mathewes, 2003).

Facing the Northern part of the CSZ, Port Alberni is a coastal city on Vancouver Island connected to the Alberni Inlet, a 78 km fjord that feeds into Barkley Sound and the Pacific Ocean (Fig. 2.1a-b). The location of the Somass River relative to the City of Port Alberni provides freshwater and terrestrial sediment input to the marsh system. Sediments deposited by the Somass River are composed of clastic fragments of basaltic Triassic Karmutsen formation, and shale, sandstone, cobble-rich conglomerate and coal of the Late Cretaceous Nanaimo group (Morris & Leaney, 1980; Yorath, 2005). Anthropogenic impacts to the study site include clear-cut logging to tidewater and timber processing beginning in the late 19th Century, and construction of wastewater treatment catalyst lagoons (Fig.2.1c) in 1958 to provide a centralized wastewater service for the region (City of Port Alberni, 2016).

Tides at Port Alberni are semidiurnal with a mean range of 2.59 m (difference between mean higher high water [MHHW, 3.13 m] and mean lower low water [MLLW, 0.54 m]) (DFO, 2023). Atmospheric circulation patterns influencing Port Alberni originate from the Pacific High-Pressure System (British Columbia Ministry of Environment, 2016). The Pacific High is strongest in the summer, resulting in well-defined warm and dry season in the summer (average summer temperature is 16°C) and cool, wet conditions in the winter (average winter temperature 3°C). Annual rainfall averages ~277 mm, with most rainfall occurring between November and January as intense storm events (Environment Canada, 2023). Other key ocean-atmosphere circulation patterns influencing Port Alberni include the El Niño-Southern Oscillation and the Pacific Decadal Oscillation. The El Niño-Southern Oscillation consists of warming from the tropical Pacific and occurs every 3-7 years and results in extreme floods or droughts and enhance storms that originate from the Pacific (Heathfield et al., 2013). The Pacific Decadal Oscillation produces similar climatic anomalies as El Niño-Southern Oscillation but over a longer duration (20-30 years) (Heathfield et al., 2013).

Coastal sediments at Port Alberni document geologic evidence for past tsunamis originating from the CSZ, including the 1700 C.E. earthquake (Clague & Bobrowsky, 1994b; Clague et al., 1994; Huntley & Clague, 1996; Hutchinson & Clague, 2017; Goff et al., 2020; Tanigawa et al., 2017; Tanigawa et al., 2022). Port Alberni is a unique field site because it is the easternmost point relative to the CSZ that records evidence of tsunami inundation (Fig. 2.1), making the area an important location for assessing the spatial distribution of tsunami inundation and coseismic subsidence.

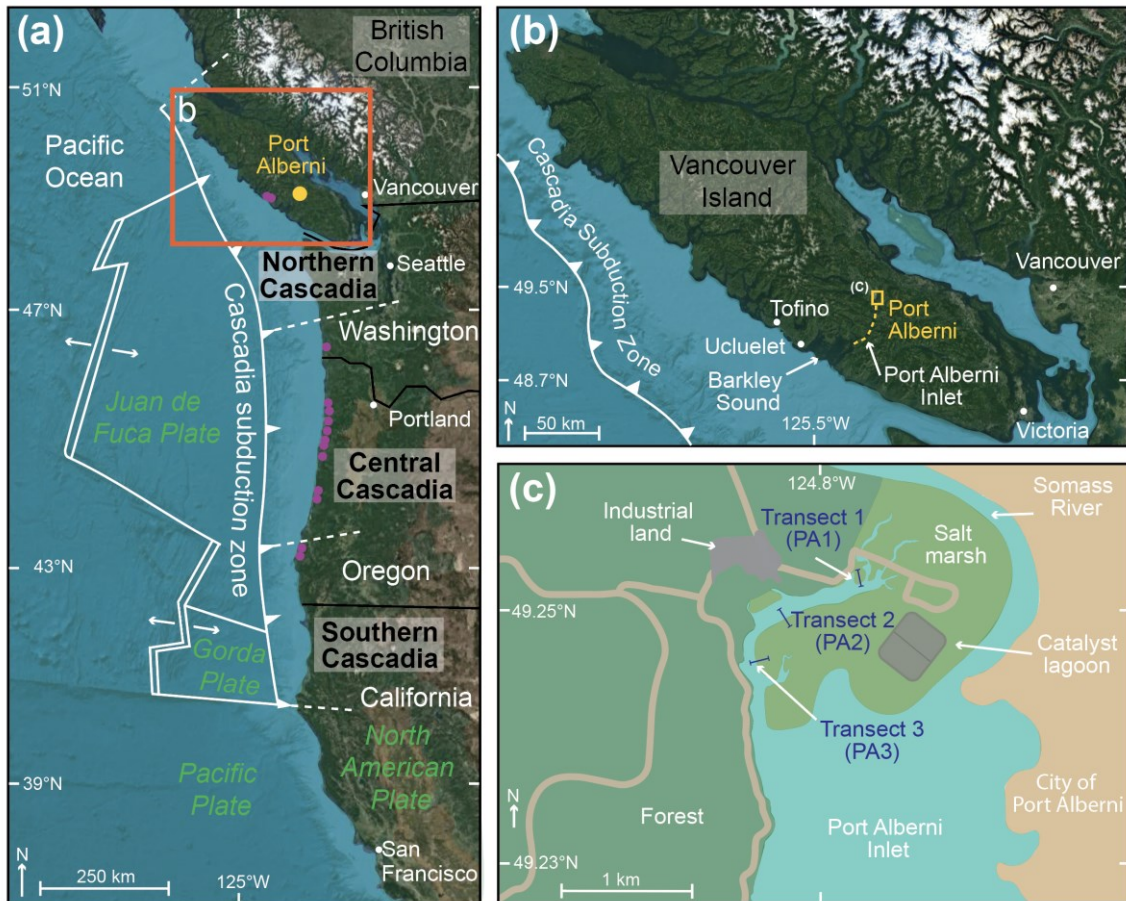


Figure 2.1. (a) Plate tectonic setting of the Cascadia subduction zone (CSZ). The CSZ extends from Northern, Central and Southern Cascadia (white dotted line) Previous sea/land reconstructions reported in Kemp et al. (2018) are represented by a purple dot. Location of the study site (yellow dot) on Vancouver Island in British Columbia, Canada (red bounding box) is indicated. (b) Broadscale geomorphology of the area surrounding Port Alberni (yellow bounding box) located at the inland terminus of the 78 km long Alberni Inlet. (c) Zoomed in view of the Somass Estuary, including the Port Alberni Marsh showing locations of transects 1 to 3 relative to marsh geomorphology.

2.4. Methods

2.4.1. Field Sampling and Data Collection

A modern training set consisting of 39 stations (Table A.1) from the Port Alberni Marsh was developed by establishing three shore-perpendicular transects that captured the full vegetation gradient from the submerged tidal flat to the forested uplands (Fig. 2.2). At each station, the top 1 cm (approximately 10 cm³) of surface sediment was collected every 3 - 10 m for subsequent microfossil (foraminifera and testate amoeba) and loss-on-ignition (LOI) analyses. Samples were treated in the field with Rose Bengal solution (20 mL of ethyl ethanol mixed with 5 mL Rose Bengal powder per 1L of H₂O) stained the cytoplasm of the foraminifera living at the time of collection in order to differentiate between the living and death assemblages (Bernard, 2000). All collected sediment samples were stored in a diluted ethanol solution with ~3 calcium carbonate (CaCO₃) chips to buffer the solution and prevent degradation of calcareous foraminifera. Samples were kept in refrigerated storage at 4 °C until subsampled for laboratory analyses.

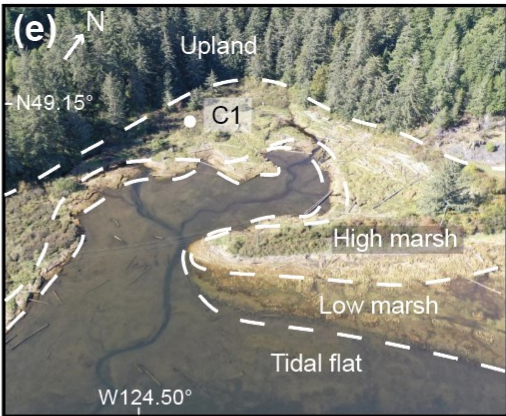
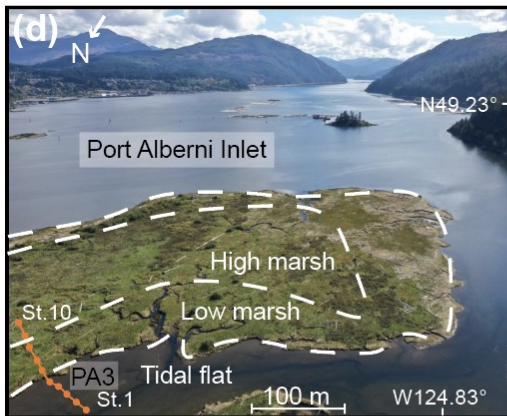
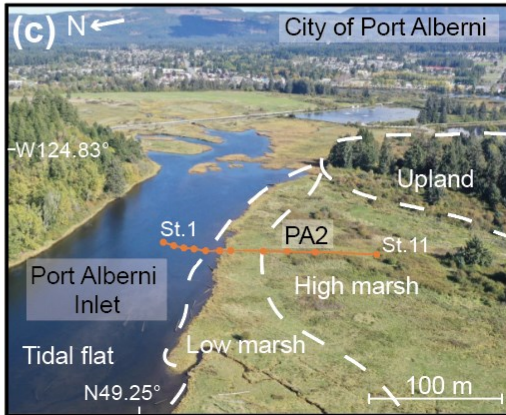
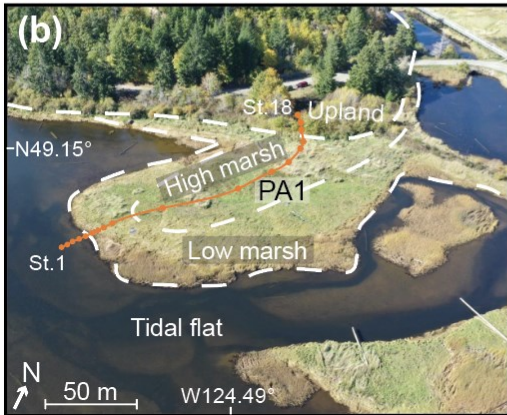
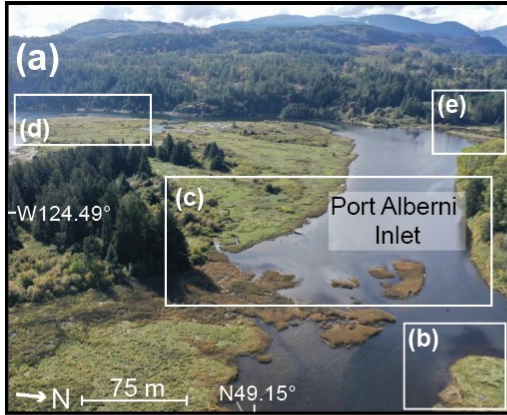


Figure 2.2. Drone images and ground-level photographs of the Port Alberni Marsh study area. (a) Position of the landward terminus of the Alberni Inlet showing marsh development on the northern, southern, and eastern edges of the inlet. The location of surface transects 1 (b), 2 (c), 3 (d), and Core 2 (e) are indicated relative to vertical zonation within the marsh from the tidal flat to the upland environment. (f) High marsh to upland transition as revealed by marsh plant vegetation (white dashed lines). (g) Tidal flat to low marsh transition based on marsh vegetation and the abrupt change from minerogenic (tidal flat) and organic (low marsh) sediment composition.

To reconstruct relative sea-level change over time, eight cores were collected, varying in length from 0.5 to 1 m throughout the salt marsh and near the transects (Fig. 2.7). Cores were retrieved from the marsh surface using an Eijkelpkamp Russian corer, a method that minimizes soil compaction (DeLaune et al., 2013). Each of the eight sediment cores were photographed, logged, and described in the field using the Troels-Smith classification system (Troels-Smith, 1955). C1 was selected as a representative core for detailed microfossil, LOI, and radiocarbon analysis (Table A.2). All cores and surface samples were packaged in plastic wrap in the field and stored in a refrigerator at 4 °C until subsequent analyses.

The location and elevation for each surface sample and sediment core was obtained using a Spectra SP80 Real-Time Kinematic (RTK) Global Navigation Satellite System (GNSS). Each elevation measurement, tied to the Port Alberni benchmark (59C9001), was collected over a one-minute interval to achieve accuracies of ± 3.9 cm. Each sampled station was calibrated to tidal elevation at the time of collection to formalize its relationship to tides. To relate the elevation of each station to the benchmark's tidal datum, measured elevations were referenced to the benchmark chart datum using the National Oceanic and Atmospheric Administration's definition of water level measurements: MHHW (mean higher high water), MTL (mean tide level) and MLLW (mean lower low water) (NOAA Tides & Currents, 2023). Elevations tied to chart datum were referenced to mean tide level using hourly water-level observations from 2011-2022 (encompassing all available data

from the latest National Tidal Datum Epoch) accessed through the Fisheries and Oceans Canada Station Inventory Data website (Fisheries and Oceans Canada (DFO), 2023).

Tidal elevation measurements were then converted to a standardized water level index (SWLI) following the methods of Horton et al. (1999). Measurements converted to SWLI were used to compare the elevation of collection stations in Port Alberni with those from other salt marshes in Cascadia with different tidal frames. SWLI values were calculated using the following equation:

$$SWLI_n = \frac{100(h_n - h_{MTL})}{h_{MHHW} - h_{MTL}} + 100 \quad (1)$$

Where $SWLI_n$ is the standardized water level index for sample n , h_n is the sample elevation for sample n , h_{MTL} is the elevation of mean tide level according to chart datum, and h_{MHHW} is the height of mean higher high water according to chart datum. A SWLI value of 100 is equivalent to MTL and a value of 200 corresponds to the MHHW mark.

2.4.2. Proxy Analysis of Surface Sediment Samples

Microfossil analysis

Surface sediment samples were prepared for micropaleontological analysis by wet sieving 5 cm³ of subsampled sediment through 500 µm and 45 µm sieves following the methods of De Rijk (1995) and Horton & Edwards (2006). Using stacked sieves in this way ensured that both foraminifera and testate amoebae were concentrated by removing larger and smaller fractions of the sediment sample (Charman, 2001). Once sieved, samples were split into 8 equal aliquots following the methods of Scott and Hermelin (1993). Individual aliquots containing foraminifera and testate amoebae were counted under a Nikon SMA 725 microscope. Each analyzed aliquot was counted in its entirety to avoid any species bias associated with species-specific settling dynamics (Patterson and Kumar, 2002), ensure a conservative count of at least 100 individuals per sample were reached

(Kemp et al., 2020), and obtain a concentration value (i.e., number of microfossils per volume of sediment). Foraminifera and testate amoebae were identified following the taxonomy of Jonasson & Patterson (1992), Blais-Stevens & Patterson (1998) and Hawkes et al. (2010) (Fig. A.1).

Loss-on-Ignition

Salt marsh zones were further discriminated by subsampling approximately 5 cm³ of surface sediment for LOI analysis to assess sediment composition (Roe et al., 2009; Kemp et al. 2018). Surface sediments were prepared following the methods of Ball (1964), where samples were dried in a drying oven at 100°C for 12 hours then subsequently burned in a Thermo Scientific Thermolyne Furnace (model type: F6000) at 550°C for 4 hours and 900°C for 2 hours to determine the percent moisture, organic content, and minerogenic content, respectively.

Statistical Analyses of Modern Assemblages

Partitioning around medoids (PAM) cluster analysis was first used to assess how well foraminifera and testate amoebae zoned within the Port Alberni Marsh. PAM cluster analysis, an ordination technique, was used to determine groups by clustering datapoints (i.e., station samples) to medoids (Kaufman & Rousseeuw, 2005). PAM analysis was used to identify groupings of foraminifera and testate amoebae from each of the sample stations (Fig. 2.2). The “cluster” package in R software (Maechler et al., 2012) and “factoextra” (Kassambara & Mundt, 2016), a visualizing package for multivariate data, were used to group sampled stations within specific medoid groups. The “cluster” algorithm assigned a silhouette width (Si) that reflected how well-suited each station was within a group; where a value of 1 indicated a station belonging perfectly within a group, and a value of -1 indicating the station sample belonged imperfectly within a group. To assess which clustered scenario was most probable, scenarios were tested ranging between 1 and 4 clusters to determine which produced the highest average silhouette width (e.g., Pilarczyk et al., 2020). The scenario with the highest average silhouette width was selected for further multivariate analyses and interpretations because it was recognized as an indication of the strongest structure within the dataset (i.e., a strong grouping of foraminiferal and testate amoebae assemblages).

Following PAM cluster analysis, detrended correspondence analysis (DCA) (Hill & Gauch, 1980) was used to plot datapoints (i.e., sampled stations) and items (i.e., species). DCA employed PAM-derived clusters to determine the dominant species represented in each cluster. Species and stations that plotted the furthest away within multi-dimensional space were the most dissimilar from one another; whereas species and stations that plotted close to one another were most similar (Hill & Gauch, 1980, Edwards & Wright, 2015). Environmental variables (i.e., elevation expressed as SWLI) were plotted to determine whether elevation was an environmental control for the distribution of microfossils within the marsh .

2.4.3. Proxy Analysis and Chronology of Sediment Cores

Eight sediment cores (C1-C8) were collected from various locations within the Port Alberni Marsh (Fig. 2.7). High resolution optical images for each core were obtained using an ITRAX Core Scanner (Fig. 2.7). C1 was selected for detailed microfossil (sampling resolution = every 1 cm), LOI (sampling resolution = every 1 cm), and chronologic analyses (sampling resolution = every 0.5 cm) because it captured two anomalous sandy deposits and was the least reworked of all cores. The eight collected sediment cores were correlated along East-West and Northeast-Southwest transects (Fig. 2.7) to assess the spatial extent of major stratigraphic units.

To resolve the timing of both gradual and abrupt environmental change occurring within the salt marsh stratigraphy, C1 was subsampled at 0.5 cm intervals above and below each sand layer (15-25 cm and 50-60 cm core depth), and between sand units (27-56 cm core depth) for radiocarbon analysis. Subsampled intervals were examined under a Nikon SMA 725 microscope for *in situ* material (material in growth-position, e.g., *Triglochin maritima* rhizomes) and detrital or bulk material (undifferentiated sediment interval) (Shroder & Shroder, 2013). Samples for radiocarbon dating were rinsed with deionized water and subsequently dried at 100°C. A total of 12 radiocarbon samples (10 *in situ*, 2 detrital) were sent to the National Ocean Sciences Accelerator Mass Spectrometry (NOSAMS) Laboratory for AMS radiocarbon dating (Fig. 2.7, Table 2.2, Table A.3).

A Bayesian age-depth model (Bacon, version 3.2.0) was used to assist in resolving the rate of RSL change as well as the timing of possible earthquakes and tsunamis preserved within C1 (Blaauw & Christen, 2011; Fig. 2.9, Table A.3). Radiocarbon ages were first calibrated to calendar dates (years C.E.) using the IntCal20 Northern Hemisphere calibration curve (Reimer et al., 2020), and then accompanied by prior information to produce modelled ages for every 1 cm depth interval. Prior information, including a “slump prior” applied to intervals containing instantaneous sedimentation (i.e., tsunami sand layers) were detailed in Table 2.1. Absolute known ages were used to constrain the model by adding the dates of core collection (2021) and the historical 1964 Alaska tsunami contained within sediment cores (Fig. 2.7) and described by Tanigawa et al. (2022).

Table 2.1. Model inputs and priors for the Bacon age-depth model for C1.

Bacon input function	Prior input argument explanation
cc = 0	Known absolute age for surface age (modern age at 0 cm) and historical events (4 cm for 1964 Alaska tsunami)
cc = 1	IntCal20 calibration curve for northern hemisphere terrestrial for 14C dates
thick = 1	Thickness for core division. Small thickness for shorter core depths
mem.mean = 0.1	Prior for the memory ranging from 0 (no assumed memory) and 1(assumed memory)
mem.strength = 10 (default setting)	Prior for the memory (independence of accumulation rate between thickness depths)
slump = c(25, 21, 58, 53)	Sections of instantaneous sedimentation for tsunami sands including lower and upper depth with a slump at 58-53 cm and 25-21 cm.
acc.mean = 10 (suggested setting)	Accumulation rate for each thickness depth (cm/yr)
acc.shape = 1.5 (default setting)	Prior for the accumulation rate shape kept at default setting
Ssize = 5000	Number of iterations to store at the end of MCMC run. Higher value for more reliable runs

2.5. Reconstructing Relative Sea-Level

2.5.1. Development of the Local Port Alberni Modern Training Set and Update to the Cascadia Regional Dataset

To reconstruct changes in relative sea-level over time, the Cascadia Regional Foraminifera Database (Kemp et al., 2018) was first updated by: (1) removing transects outside of the CSZ; (2) standardizing the dataset to only include the death assemblage; and (3) expanding the dataset to include three new local transects (n = 37) in Northern Cascadia from Port Alberni (PA1, PA2, and PA3, Fig. 2.4-2.6).

Datasets outside of the CSZ (i.e., south of the Gorda Plate) were removed from the regional training set as they were too far south of the CSZ and represented environments not analogous to the temperate marshes that characterise the Cascadia coastline. The removed samples included those documented by Avnaim-Katav et al. (2017) from Seal Beach, California and Tijuana, Mexico.

In the first iteration of the Cascadia Regional Foraminifera Database (now referred to as *Cascadia I*; i.e., Kemp et al., 2018), data from Jennings and Nelson (1992) was reported as the total assemblage and included both living and dead individuals. Living individuals (i.e., those with a cytoplasm stained by Rose Bengal solution) can be problematic because of seasonal changes in the assemblage (Jones and Ross, 1979). To maintain consistency over all reported local training sets, the Jennings and Nelson (1992) data was standardized to reflect only the death assemblage.

A new local training set was developed for the Port Alberni Marsh based on 39 sampled stations over three transects (PA1, PA2, PA3) that characterized the relationship between microfossil distributions and tidal inundation at this location. Two station samples (Transect 1, st.17 and st.18) at the furthest inland extent along Transect 1, were removed from the local and regional training set and subsequent statistical analyses (PAM and DCA) because they lacked statistically significant counts of both foraminifera and testate amoebae. When adding the Port Alberni local training set to Kemp et al. (2018)'s *Cascadia I* Database, the species standardization of Kemp et al. (2018) was adopted. For example,

Haplophragmoides wilberti and *Haplophragmoides manilaensis* were grouped together as *Haplophragmoides* spp. Similarly, calcareous foraminifera were grouped together, as were species within the *Ammobaculites* and *Trochammina* genera. The updated Cascadia Regional Foraminifera Database, now called “*Cascadia 2*” was detailed in Table A.4.

2.5.2. Relative Sea-Level Reconstruction

RSL at Port Alberni was reconstructed by relating the microfossil assemblages from the modern surface samples with those contained within C1 using a BTF (Cahill et al., 2016). The BTF applied to the RSL reconstruction modelled the relationship between modern microfossil assemblages and elevation, then related this relationship to their analogous fossil assemblages within the core (Imbrie and Kipp, 1971; Kemp et al., 2018).

Two informative priors were assigned: (1) the percentage of freshwater testate amoebae (>7% relative abundance within sediment core intervals); and (2) the percent organic content from LOI (<12% for tidal flats and >35% for high marsh). Informative priors were determined using surface samples from stations along all three transects and compared to regional studies (e.g., Roe et al., 2009; Douglas et al., 2022). The lowest occurrence of testate amoebae (LOT) was the lowest elevation where freshwater testate amoebae were present. Conversely, the highest occurrence of foraminifera (HOF) was determined by the highest elevation where foraminifera were found within modern surface samples. Using the LOT-HOF range, core intervals containing both testate amoebae and foraminifera were given a prior range of 200-223 SWLI (Table A.2). Sediment intervals containing the same LOI values as modern tidal flat samples (<12% LOI) were given a prior range of 0-100 SWLI, and sediment samples containing the same LOI values as modern high marsh samples (>35% LOI) were given a prior range of 143-223 SWLI. Sediment intervals containing LOI values between 12-35% were given an uninformative prior of 100-223 SWLI, which assumed to have formed between low and high marsh. Informative priors such as LOT, HOF, and LOI assisted to increase the probability that a sample would fall within range without forcing a sample into range (Cahill et al., 2016; Kemp et al., 2018; Nelson et al., 2020; Padgett et al., 2022).

To ensure the most precise relative sea-level reconstruction, four iterations of the BTF were assessed: (1) local Port Alberni training set without informative priors; (2) local Port Alberni training set using informative priors; (3) *Cascadia 2* training set without informative priors; and (4), *Cascadia 2* training set using informative priors. The BTF with the least uncertainty was used to estimate changes in paleommarsh elevation (PME) and RSL over time (Fig. 2.9, 2.10). Where stratigraphic evidence for possible abrupt land-level change was present in C1, the elevation difference between the peat underlying the anomalous sand and the overlying mud layer was calculated using the corresponding PMEs for each unit.

Once PMEs were estimated using the BTF, RSL was converted to m MTL using equation (2):

$$RSL_n = Altitude_n - PME_n \quad (2)$$

Where RSL_n is the RSL at core depth n , $Altitude_n$ is the altitude at core depth n (relative to MTL), and PME_n is the paleommarsh elevation at core depth n (m MTL). A constant of 0.701 was applied to all final RSL values to adjust RSL core top to 0 m MTL.

RSL at Port Alberni over the last 700 years was modelled using the RESLR package in R (version 0.1.1; Upton et al., 2023). RESLR uses paleommarsh elevations obtained from the BTF and modelled ages obtained from Bacon age-depth estimates to determine changes in RSL and annual rates of change through time. Within the RESLR package, the errors in variable integrated Gaussian process model were employed to account for inherent uncertainties. Non-linear fits using a gaussian process prior on the rate of sea-level change was most appropriate when examining data from a single site location (Upton et al., 2023). RESLR produced a sea-level curve at 95% confidence intervals and modelled yearly rates of change (mm/yr) (Fig. 2.10, Table A.5).

2.6. Results

2.6.1. Surface Distributions Within the Tidal Frame

Collectively, 39 surface samples collected over three transects across the Port Alberni Marsh display an elevation range from 48 to 330 SWLI, representing tidal flat, low marsh, high marsh, and the upland environments (Fig. 2.4-6). In general, subenvironments within the salt marsh correspond with marked changes in microfossil distributions, plant microvegetation, and organic content.

The tidal flat (48 - 100 SWLI) is predominantly characterized by low density strands of the seagrass *Zostera sp.*, low organic content (4-28%), and high abundances of the foraminifera *Miliammina fusca*. Similarly, the low marsh (84 – 197 SWLI) is characterized by denser and more diverse vegetation including the perennials *Glaux maritima* and *Juncus balticus*, organic content ranging from 3-54%, and a change in foraminiferal assemblage with the inclusion of higher abundances of *Jadammina macrescens* and *Balticammina pseudomacrescens* species. Increasing in plant diversity and organic content, the high marsh (176-261 SWLI) is characterized by *Carex lyngbyei*, *Potentilla pacifica*, *Deschampsia cesoitosa*, *Distichlis spicata*, *Cirsium arvense*, *Symphyotrichum subspicatum*, *Solidago multiradiata*, *Rosa nutkana*, organic content ranging from 34-68%, and the dominance of *Balticammina pseudomacrescens* and *Haplophragmoides wilberti*. Lastly, the upland region (283-330 SWLI) is dominated by the freshwater deciduous *Populus balsamifera*, contains 40-46% organic content, and testate amoebae (0-8 species/cm³).

Transect 1 (PA1)

Transect 1 consists of 18 surface samples spanning the tidal flat to the uplands, over a horizontal distance of 120 m and a vertical range of 2.89 m (95-330 SWLI; Fig. 2.4). A total of 16 species of foraminifera and testate amoebae are present along the transect (Fig. 2.4a). Two upland stations (stations 17 and 18) contain no foraminifera or testate amoebae and are removed from PAM, DCA, and the local Port Alberni training set. The concentration of foraminifera is highest in the tidal flat (100-499 species/cm³) and

progressively decreases within increasing elevation. The low marsh, high marsh, and uplands contain an average of 59-197 species/cm³, 4-97 species/cm³ and 0-1 species/cm³ respectively.

Surface samples collected from the tidal flat (st.1 and 2) occupy a SWLI range of 95 to 100 and are dominated by *M. fusca* (89 ± 4%). The low marsh at 115 - 197 SWLI (between MTL and MHHW) sees a decrease in the relative abundance of *M. fusca* (57 ± 17%), an increase in abundance of *J. macrescens* (20 ± 17%), and small numbers of *A. dilatatus* (0.4 ± 0.2%). The high marsh at 204 – 261 SWLI (above MHHW) is characterized by a further decrease in *M. fusca* (8 ± 7%), and a pronounced increase in *B. pseudomacrescens* (31 ± 20%) and *T. inflata* (19 ± 14%). Lastly, the upland, the section of the marsh that is outside of the tidal range, at 283 to 330 (above MHHW), is dominated by testate amoebae (33 ± 57%) and *T. irregularis* (33 ± 57%).

Transect 2 (PA2)

Transect 2 contains 11 surface stations from the tidal flat to the high marsh, spanning a horizontal distance of 125 m with a vertical range of 2.38 m (Fig. 2.5a). In general, Transect 2 (PA2) is similar to Transect 1 (PA1) in terms of foraminifera concentration within subenvironment with the highest concentrations observed in the tidal flat and gradually decreasing with increasing elevation. Specifically, PA2 concentrations range from 73-426 species/cm³, 81-86 species/cm³, to 5-48 species/cm³, in the tidal flat, low marsh, and high marsh, respectively. The dominant species in both PA2 and PA1 in the tidal flat and low marsh is *Miliammina fusca*, while *Balticammina pseudomacrescens* dominates the high marsh in both transects.

Surface samples collected from the tidal flat at 48 – 98 SWLI (below MTL) are dominated by *M. fusca* (96 ± 4%) and *A. dilatatus* (0.9 ± 0.5%). The low marsh with elevation range of 129 – 163 SWLI (between MTL and MHHW) decreases in *M. fusca* (52 ± 37%) abundances, while increasing in species abundances with *B. pseudomacrescens* (15 ± 13%), and *T. inflata* (16 ± 015%). The high marsh at 195 – 252 SWLI (above MHHW other than station 8), has the lowest abundances in *M. fusca* (2 ± 3%), and contains the

highest abundances of *B. pseudomacrescens* ($52 \pm 27\%$) and *H. wilberti* ($13 \pm 10\%$) of all three zones. Average foraminifera concentrations are highest in the tidal flat (231 species/cm³), and progressively decrease in the low marsh (71 species/cm³), and high marsh (19 species/cm³).

Transect 3 (PA3)

The third transect, PA3, totals 10 surface sediment samples from the tidal flat to the high marsh, over 34 m of distance with a vertical range of 1.70 m (Fig. 2.6a). PA3 exhibits similarities with PA1 and PA2 in terms of foraminiferal concentrations across subenvironments, with highest concentrations in the tidal flat, gradually decreasing toward the high marsh. Foraminifera and testate amoebae concentrations range from 118-210 species/cm³ in the tidal flat, to 41-91 species/cm³ in the low marsh, and 81-106 species/cm³ in the high marsh. However, PA3 differs from the other transects, consistently displaying lower organic content. The organic content in PA3 ranges from 2-12% in the tidal flat, to 3-9%, in the low marsh, and 34-35% in the high marsh. The organic content of PA1 and PA2 are similar with ranges from 12-28% in the tidal flat, to 23-54% in the low marsh, and 54-84% in the high marsh (PA1); and 3-10% in the tidal flat, 26-45% in the low marsh, and 49-62% in the high marsh (PA2).

Like Transect 2, Transect 3 has a plant zonation comprising a tidal flat, low marsh, and high marsh. The tidal flat at 62 – 78 SWLI (below MTL), is dominated by *M. fusca* ($94 \pm 3\%$). Moving up in elevation at 84 – 145 SWLI (around MTL), the low marsh contains lower abundances in *M. fusca* ($51 \pm 38\%$) compared to the tidal flat but higher abundances of *B. pseudomacrescens* ($29 \pm 27\%$), and *T. inflata* ($6 \pm 3\%$). The high marsh elevation at 176-200 (between MTL and MHHW), contained the lowest abundances in *M. fusca* ($18 \pm 6\%$), the highest abundances of *B. pseudomacrescens* ($61 \pm 10\%$), and the presence of testate amoebae ($4 \pm 5\%$). The highest average foraminifera concentrations are in the tidal flat (158 species/cm³), with decreasing concentration in the low marsh (60 species/cm³), and lowest in the high marsh (94 species/cm³).

2.6.2. Species Flexible Response Curves

The BTF estimates a response curve for all the observed foraminifera in the Port Alberni surface samples (Fig. A.2) and the *Cascadia 2* training set (Fig. A.3). Fig. 2.3 shows the response curve of the 6 most common species found in the local Port Alberni training set (red points) and the *Cascadia 2* training set (blue points), expressed in SWLI. *J. macrescens* and *T. inflata* exhibit a bimodal distribution curve, with two peaks found at 174 and 201 SWLI, and 191 and 211 SWLI, respectively. The other four species (*M. fusca*, *Haplophragmoides* spp., *Trochamminita* spp. and *B. pseudomacrescens*) form a skewed unimodal distribution curve. *M. fusca* contains the lowest elevation value at a maximum probability from 0 to 124 SWLI. *Haplophragmoides* spp. has a probability of 48% at 201 SWLI. *Trochamminita* spp. is found at higher elevations with probabilities of 37% at 236 SWLI, with *B. pseudomacrescens* found highest with probabilities of 41% at 241 SWLI.

Comparing the *Cascadia 2* training set plotted up in blue and the Port Alberni training set in red points, local observed data shows *J. macrescens* occurs within the 95% prediction intervals, with more samples near one of its peaks. The greatest difference in observed data is *Haplophragmoides* spp., with the local training set abundances found below the predicted probabilities (mean, 95% credible intervals), especially at higher elevations >200 SWLI. *T. inflata*, *M. fusca*, and *Trochamminita* spp. local observed data align close to their respective mean model, with many samples located near their highest probability. *B. pseudomacrescens* abundances are spatially variable along elevations, aligning close to the mean model at lower elevations (20-110 SWLI) and spanning out beyond 200 SWLI.

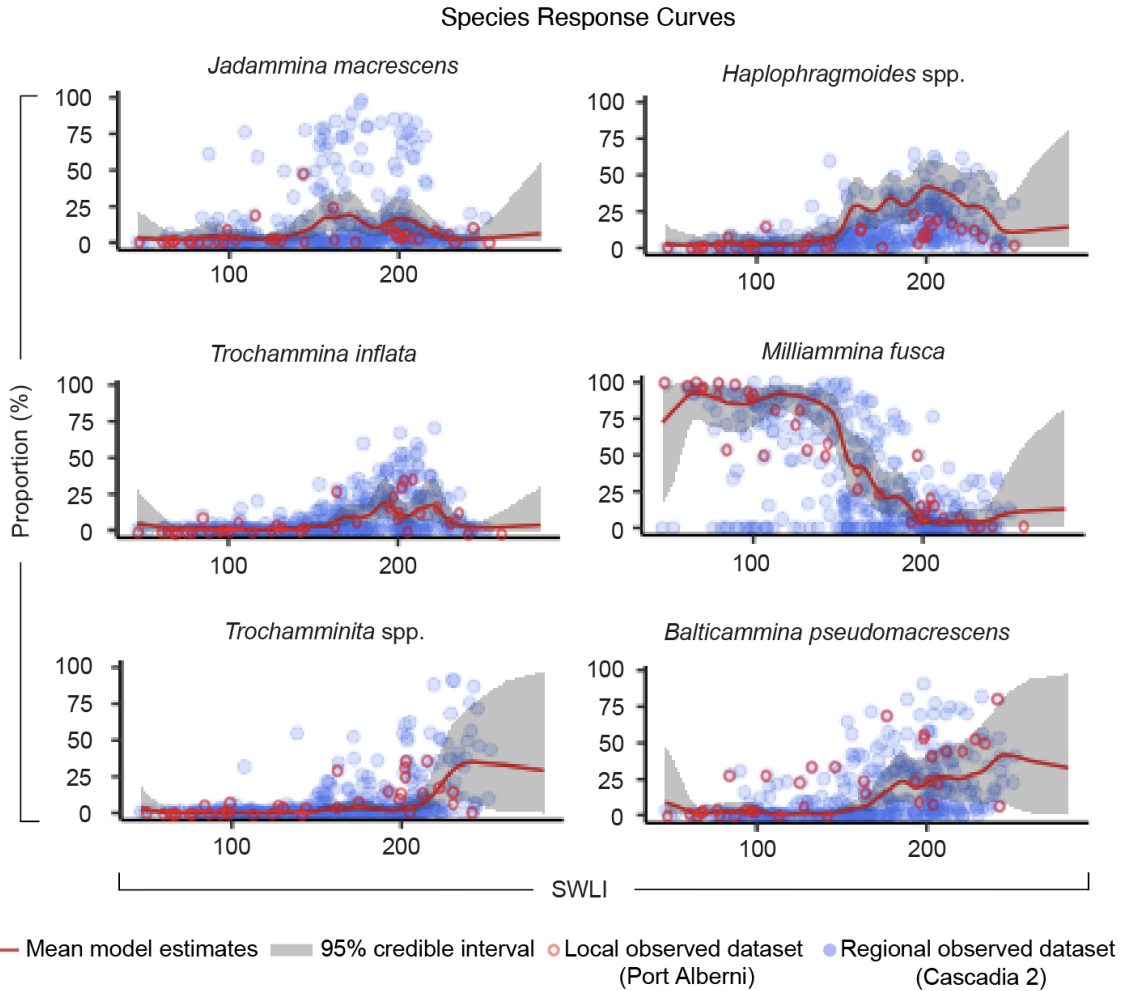


Figure 2.3. Species response curves (taxa-elevation relationship) for the six dominant species of foraminifera as predicted by the BTF using the local Port Alberni (red circles) and updated regional *Cascadia 2* (blue dots) training sets relative to elevation (SWLI). The mean model is shown in the solid red line and the 95% credible intervals is shown as the grey shaded area.

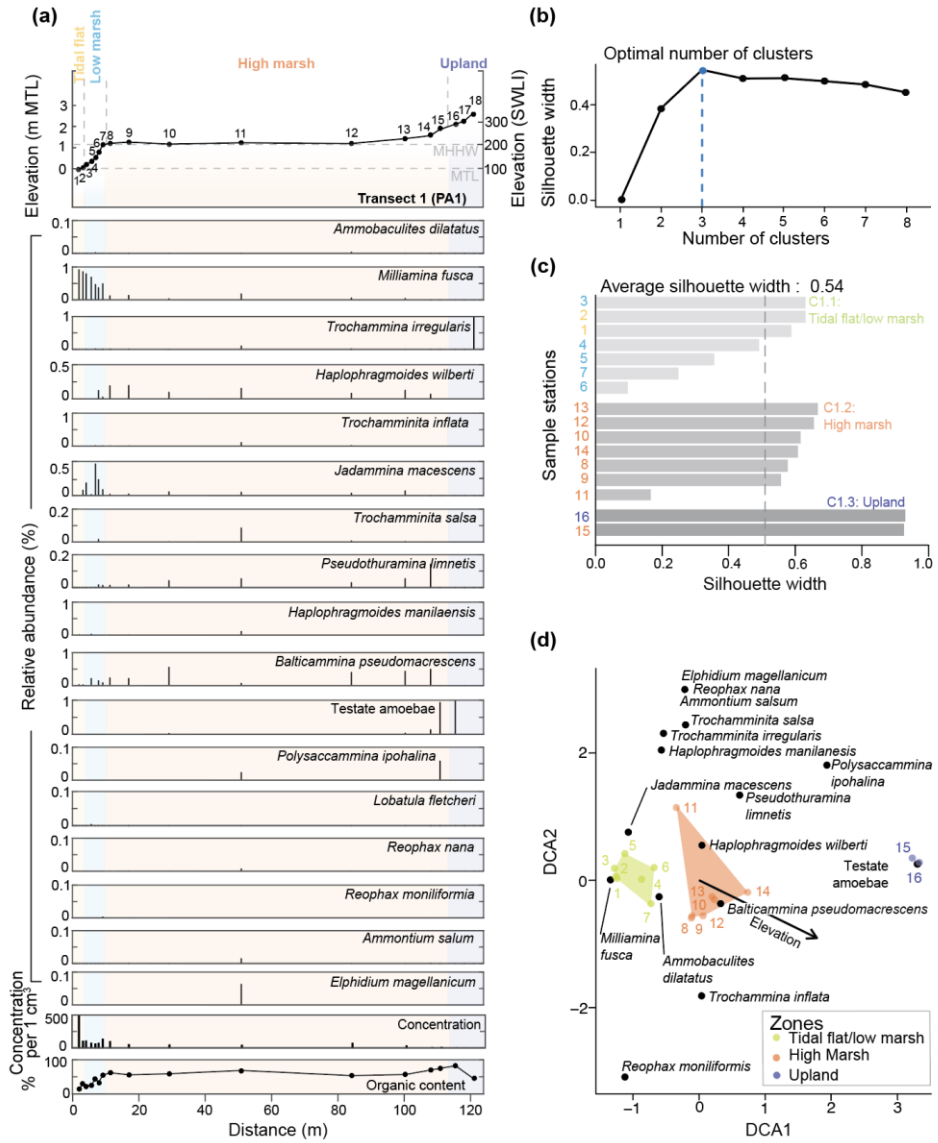


Figure 2.4. Microfossil (foraminifera and testate amoebae) and organic content for 18 stations along Transect 1 (PA1). (a) Relative abundances of microfossils and organic content relative to elevation (m MTL and SWLI) increasing distance inland (m) within the marsh. Tidal flat, low marsh, high marsh, and upland subenvironments are indicated and based on observed plant vegetation. (b) Results of partitioning around medoids (PAM) cluster analysis indicating that the optimal number of clusters (blue dotted line) is 3 based on the scenario with the highest average silhouette width. (c) Corresponding PAM clusters based on microfossil data. The average silhouette width is indicated by a grey dashed line. (d) Detrended correspondence analysis (DCA) showing associations between sample stations and microfossil species relative to tidal flat, low marsh, and upland clusters.

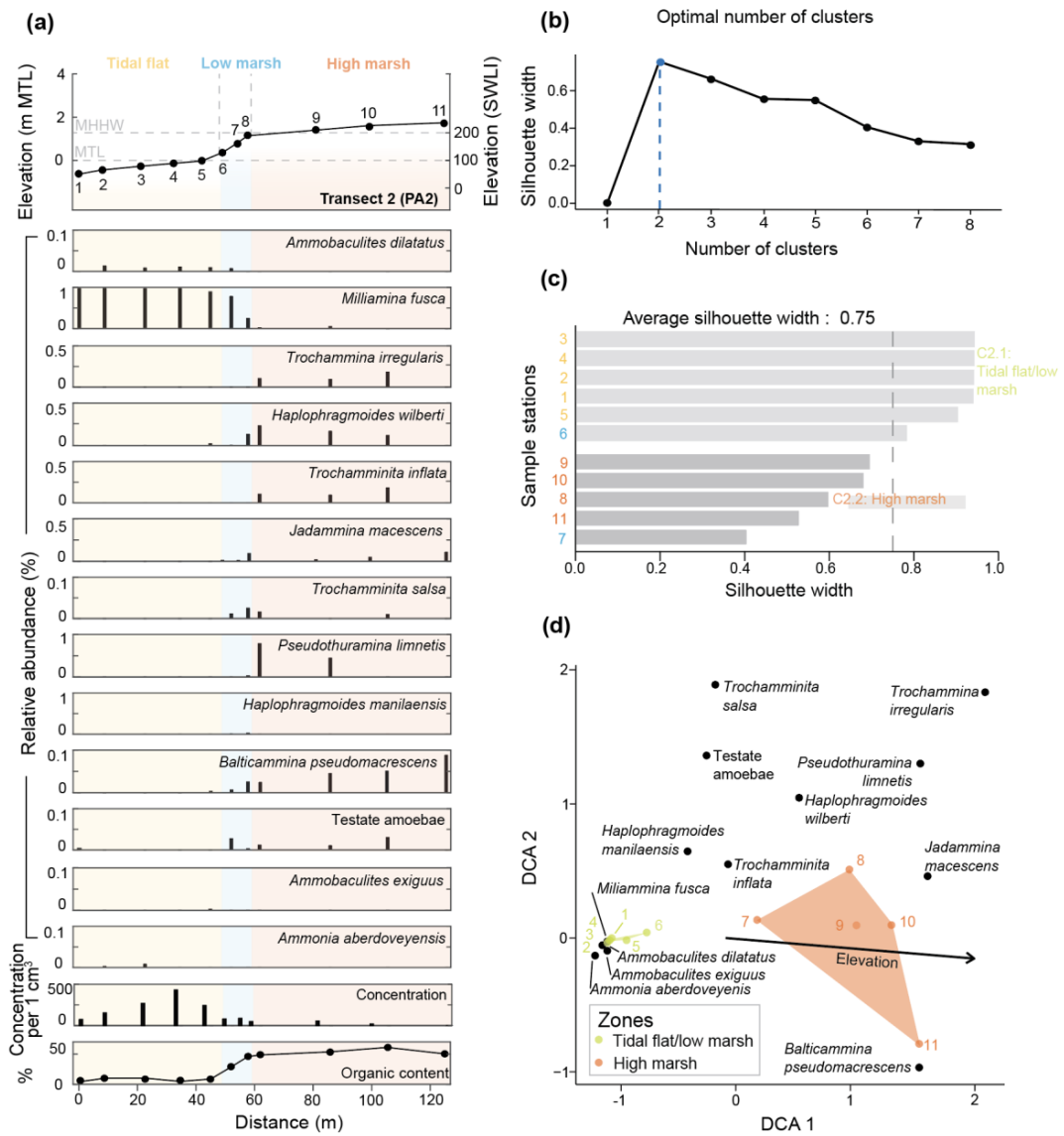


Figure 2.5. Microfossil (foraminifera and testate amoebae) and organic content for 11 stations along Transect 2 (PA2). (a) Relative abundances of microfossils and organic content relative to elevation (m MTL and SWLI) increasing distance inland (m) within the marsh. Tidal flat, low marsh, and high marsh subenvironments are indicated and base on observed plant vegetation. (b) Results of partitioning around medoids (PAM) cluster analysis indicating that the optimal number of clusters (blue dotted line) is 2 based on the scenario with the highest average silhouette width. (c) Corresponding PAM clusters based on microfossil data. The average silhouette width is indicated by a grey dashed line. (d) Detrended correspondence analysis (DCA) showing associations between sample stations and microfossil species relative to tidal flat and high marsh clusters.

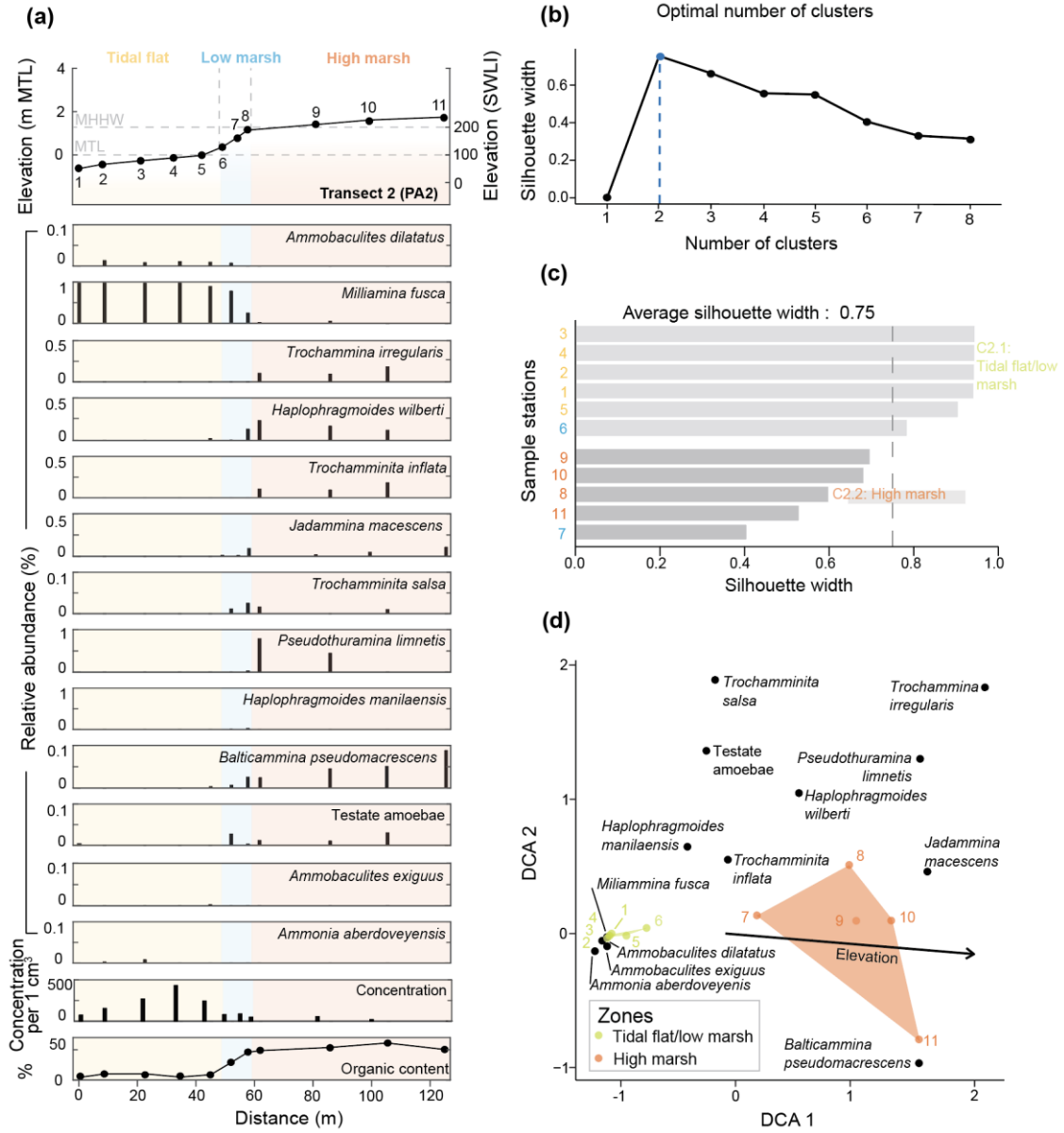


Figure 2.6. Microfossil (foraminifera and testate amoebae) and organic content for 10 stations along Transect 3 (PA3). (a) Relative abundances of microfossils and organic content relative to elevation (m MTL and SWLI) increasing distance inland (m) within the marsh. Tidal flat, low marsh, and high marsh subenvironments are indicated and base on observed plant vegetation. (b) Results of partitioning around medoids (PAM) cluster analysis indicating that the optimal number of clusters (blue dotted line) is 3 based on the scenario with the highest average silhouette width. (c) Corresponding PAM clusters based on microfossil data. The average silhouette width is indicated by a grey dashed line. (d) Detrended correspondence analysis (DCA) showing associations between sample stations and microfossil species relative to tidal flat, low marsh and high marsh clusters.

2.6.3. PAM Analysis

Transects stations cluster well, based on observations of plant vegetation and reported silhouette widths of 0.54, 0.75, and 0.79 for transect 1, 2, and 3, respectively. Transect 1 contains an optimal number of three clusters (Fig. 2.4b-c). C1.1: Tidal flat/low marsh ($Si = 0.43$), combines the tidal flat and low marsh into one cluster (Station 1-7). C1.2: High marsh ($Si = 0.54$) contains station 8-14. Lastly, C1.3: Upland ($Si = 0.92$), contains stations 15 and 16. In contrast, transect 2 contains two optimal clusters (Fig. 2.5b), grouping stations 1-6 in cluster C2.1: Tidal flat/low marsh ($Si = 0.90$), and station 7-11 in cluster C2.2: High marsh ($Si = 0.58$). The stations that do not group according to the vegetation is station 6 and 7. Instead, station 6 groups into the tidal flat/low marsh cluster (C2.1) and station 7 into high marsh cluster (C2.2). These results indicate that the foraminiferal assemblages of the low marsh (derived from vegetation) did neither closely resembles the tidal flat or the high marsh (Fig. 2.5c). Lastly, transect 3 reveals an optimal number of three clusters: C3.1: Tidal flat ($Si = 0.92$, stations 1-4), C3.2: Low marsh ($Si = 0.77$, stations 5-8), and C3.3: High marsh ($Si = 0.58$, stations 9-10). The three clusters in transect 3 perform the best, distinguishing observed plant zonation and placing all stations in their respective zones (Fig. 2.6c).

2.6.4. DCA Analysis

DCA analysis identifies two to three clusters, indicating the tidal flat/low marsh clusters plot furthest away in ordination space from high marsh clusters, indicating they are most dissimilar from one another (Fig. 2.4-2.6).

The low elevation cluster in transect 1 (C1.1) groups closely with *M. fusca*, *A. dilatatus*, and *J. macrescens*. The C1.2 high marsh cluster is dominated by *B. pseudomacrescens* and *H. wilberi* and the upland cluster (C1.3) is dominated by testate amoebae. Transect 2 tidal flat/low marsh (C2.1) aligns closely with *M. fusca*, *Ammonia aberdoveyensis*, and *Ammobaculites* spp. Located further on the DCA 1 axis, the high marsh cluster (C2.2) is found close to species *B. pseudomacrescens*, *J. macrescens*, and *T. inflata*. Lastly, transect 3 tidal flat clusters (C3.1) closely align to *M. fusca*, the low marsh cluster (C3.2) with *T. irregularis*, and high marsh cluster (C3.3) with *B. pseudomacrescens*.

2.6.5. Port Alberni Marsh Stratigraphy

C1 (75 cm), used for stratigraphic, microfossil, and chronological analysis, contains three earth material units: peat (Troels-Smith description: Th², Ag¹, As¹), sand (Troels-Smith description: Ga³, Ag¹), and mud (Troels-Smith description: Ag², Ga¹, As¹) (Fig. 2.7). The bottom of the core from 75-58 cm is composed of peat (Unit 1). It has a sharp contact over 1 mm with Unit 2 (henceforth called Sand 1) from 58-56 cm. Unit 3 (Mud 1) is a 3 cm-thick mud unit at 56-53 cm. On top of Mud 3 is a dark peat (Unit 4) that extends to Unit 5 (Sand 2), a 4 cm thick sand unit composed of sand and silt. Overlying Sand 2 is Unit 6 (Mud 2), which has a gradational contact over 3 mm from 20-19 cm. From 19-5 cm depth (Unit 7), there is a gradational change to a light brown coloured peat to the uppermost soil horizon (Unit 8), which is a dark brown, organic rich peat from 5 cm to the top of the core.

Similar stratigraphy is observed throughout the 1 cm² marsh (Fig. 2.7, Fig. A.4). All cores contain a topsoil unit/O-horizon (Unit 8), a dark peat that is organic rich with abundant in-situ roots, interpreted as modern marsh sediment. With the exception of C8, all cores contain one to three sand units, varying in thickness and composition from discontinuous layers of sandy silt to 5 cm-thick beds of coarse-grained sand abruptly

overlying brown peat. A lower Sand 1 is present in C1-C4, ranging in thicknesses from 3-4 cm depth. A middle Sand 2 (Unit 5) is present in multiple cores (C1-C7) containing similar thicknesses (2-4 cm) throughout depths. An upper Sand 3 (Unit 9), a 0-1 cm thick, is present in core C2, C6, and C7 at approximately 10 cm depth. These sand layers generally fine upwards into silty muds, gradually changing in colour and texture from minerogenic, grey mud to organic rich, brown peat. Sand-mud couplets are overlain by brown to dark peat, marking the return to marsh conditions dominated by organic accumulation and decomposition.

2.6.6. Fossil assemblages

Foraminiferal fossil assemblages vary within C1. The bottom of the core within Unit 1 contains a fossil assemblage dominated by *B. pseudomacrescens* (68%), testate amoebae (10%), and *H. wilberti* (8%), and concentrations averaging 197 species/cm³. Within Unit 2 (Sand 1), the dominant fossils include *B. pseudomacrescens* (42%), *M. fusca* (33%), *H. wilberti* (10%), testate amoebae (8%), and low concentrations of 8 species/cm³. The Unit 3 (Mud 1) above Sand 1 is dominated by the fossils *B. pseudomacrescens* (45%), *M. fusca* (27%), *J. macrescens* (4%), and concentrations are 9 species/cm³. Unit 4 contains a fossil assemblage dominated by *B. pseudomacrescens* (83%), *H. wilberti* (5%), and *J. macrescens* (4%), and concentrations averaging 119 species/cm³. Dominant fossils found in Unit 5 (Sand 2) consists of *B. pseudomacrescens* (64%), *H. wilberti* (14%), and *M. fusca* (8%). Here, the fossil concentrations are low, with an average concentration of 18 species/cm³. Unit 6 (Mud 2) below the topmost peat contains similar species and abundances of *B. pseudomacrescens* (74%), *H. wilberti* (11%), and *J. macrescens* (9%), with concentrations averaging 115 species/cm³. Lastly, Unit 7 and Unit 8 contains fossils dominated by *B. pseudomacrescens* (82%), *H. wilberti* (8%), and *J. macrescens* (5%). High concentrations of fossils are found within the uppermost peat, averaging 95 species/cm³ tests (Fig. 2.9).

The dominant fossil foraminifera within C1 are *B. pseudomacrescens*, *H. wilberti*, *J. macrescens*, and to a smaller extent, *M. fusca*. These dominant species are also the dominant species in the modern surface samples. However, species *E. magellanicum*, *R.*

nana, *P. ipohalina*, *A. dilatatus*, *A. exiguous*, and *A. Aberdoveyen* that are present in the modern surface samples, are not present in the fossil assemblage. Concentrations within the modern tidal flat (average of 229 species/cm³) have a much higher concentrations than the muds in C1, averaging 62 species/cm³. Concentrations within the modern high marsh (average of 52 species/cm³) have lower concentrations than C1 peat, averaging 135 species/cm³

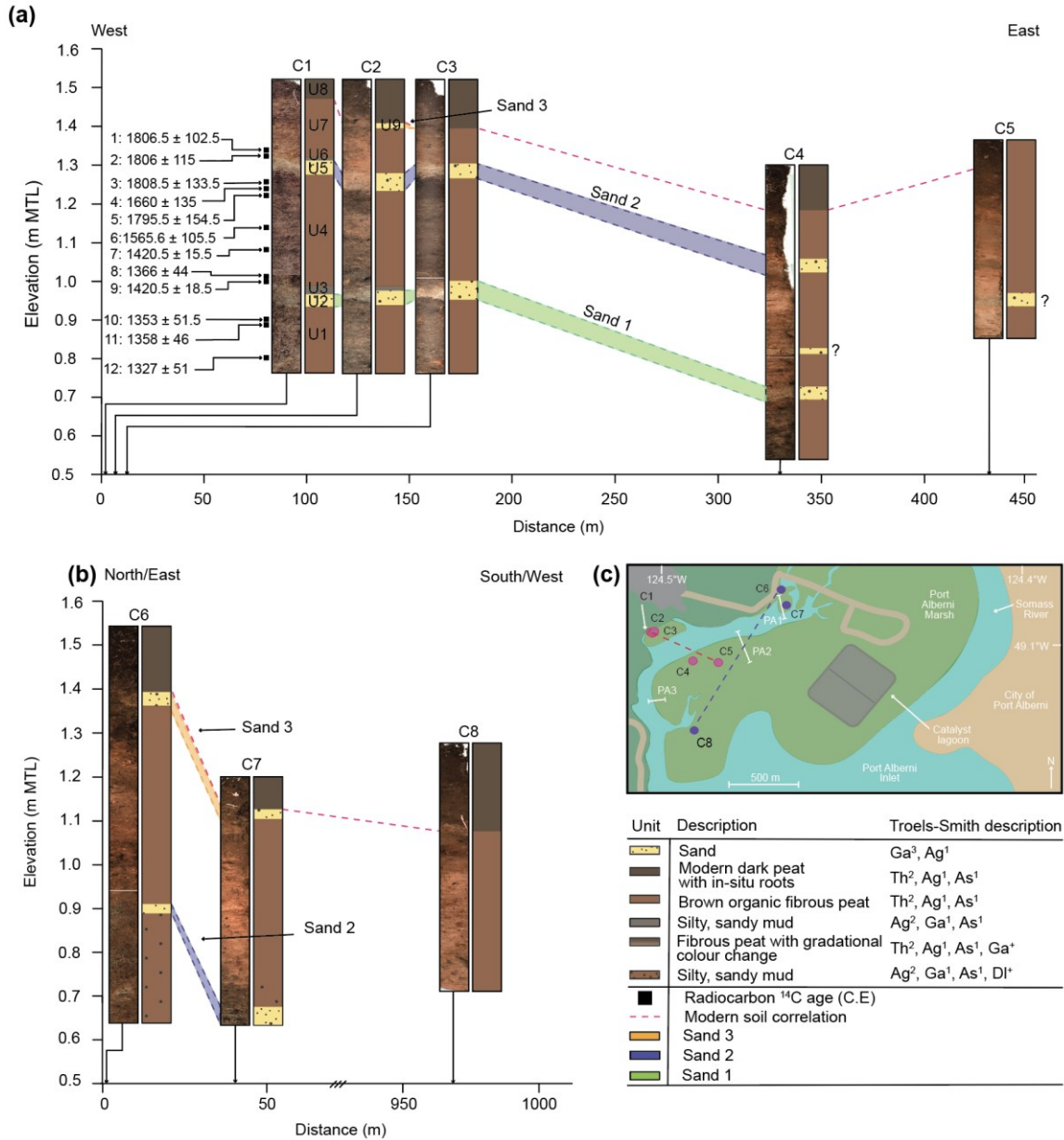


Figure 2.7. (a) Port Alberni Marsh stratigraphy. Correlated stratigraphic units along an east-west (a) and northeast-northwest (b) transect. Optical images and corresponding stratigraphic log based on Troels-Smith classification of eight cores collected along both transects. Black boxes show radiocarbon sampling location and calibrated ages in calendar years. Elevation are relative to MTL, m. (c) Inset map of the study area in Port Alberni indicating core transect 1 (pink dashed line) and core transect 2 (purple dashed line).

2.6.7. Loss-on-ignition

LOI results for C1 show organic content having high averages in the peat (39.4%), decreasing in value in the mud, averaging 28.9%, and lowest in the sands, averaging 10.5% (Fig. 2.9).

2.6.8. Chronology and Age-depth Model

A total of 12 samples (10 *in situ* and 2 detrital) were subsampled from C1 for AMS radiocarbon dating (Table 2.2, Fig. 2.9). Two bulk dates were the only dates used to constrain the upper age limit of Sand 2, having a combined calibrated age range from 1691-1921 C.E. Three radiocarbon samples (samples 3-5), (*Triglochin maritima* rhizome and seeds) used to date the peat below Sand 2 range from 1660 ± 135 to 1808.5 ± 133.5 C.E. Samples 6 and 7, collected at depths 39.5 cm and 45.5 cm below the surface, have ages of 1565.5 ± 104.5 and 1420.5 ± 15.5 C.E., respectively. Sample 9 is the only one to date above Sand 1, returning an age of 1420.5 ± 18.5 C.E. Lastly, samples 10-12 in the peat below Sand 1 have a combined calibrated age from 1327 ± 51 to 1353.5 ± 51.5 C.E.

The ages of Sand 2 and Sand 1 are constrained using a Bacon age-depth model of calibrated radiocarbon dates with a 95% confidence interval (Fig. 2.9, Table A.4). The modelled age for Sand 2 depths average 1699 C.E (1682-1721 C.E.) while Sand 1 depth has a mean modelled age of 1383 C.E (1340-1402 C.E).

Table 2.2. Data for AMS radiocarbon age samples for C1 Port Alberni Marsh.

Sample ID	Sample depth (cm)	Minimum or maximum limiting age ^a	Dated material and position relative to sands	Lab-reported ¹⁴ C age (yr BP)	Calibrated ¹⁴ C age ± 2σ C.E.	Radiocarbon laboratory No.	Used in Bacon model?
Core top	0	Minimum	Absolute age 21 cm above to Sand 2	N/A	2021 ± 1	N/A	Historical*
1964	4	Minimum	Absolute date 17 cm above Sand 2	N/A	1964 ± 1	N/A	Historical*
1	19	Minimum	Bulk peat 2 cm above Sand 2	35 ± 15	1806.5 ± 102.5	OS-171827	Yes
2	20.5	Minimum	Bulk peat 0.5 cm above Sand 2	115 ± 15	1806 ± 115	OS-171828	Yes
3	27.5	Maximum	<i>Triglochin</i> and seed 2.5 cm below Sand 2	100 ± 45	1808.5 ± 133.5	OS-171785	Yes
4	29	Maximum	<i>Triglochin</i> and seed 4 cm below Sand 2	265 ± 20	1660 ± 135	OS-171786	Yes
5	29.5	Maximum	<i>Triglochin</i> and seed 4.5 cm below Sand 2	225 ± 20	1795.5 ± 154.5	OS-171787	Yes
6	39.5	Maximum	<i>Triglochin</i> 13.5 cm below Sand 2	360 ± 15	1565.5 ± 104.5	OS-171758	Yes
7	45.5	Minimum	<i>Triglochin</i> 7.5 cm above Sand 1	515 ± 15	1420.5 ± 15.5	OS-171759	Yes
8	50.5	Minimum	<i>Triglochin</i> 2.5 cm above Sand 1	570 ± 15	1366 ± 44	OS-171760	Yes
9	51.5	Minimum	<i>Triglochin</i> 1.5 cm above Sand 1	515 ± 20	1420.5 ± 18.5	OS-171788	Yes
10	61.5	Maximum	<i>Triglochin</i> 2.5 cm below Sand 1	600 ± 25	1353.5 ± 51.5	OS-171789	Yes
11	62.5	Maximum	<i>Triglochin</i> 3.3 cm below Sand 1	590 ± 15	1358 ± 46	OS-171761	Yes
12	67	Maximum	<i>Triglochin</i> 8 cm below Sand 1	695 ± 15	1327 ± 51	OS-171757	Yes

^a Interpretation of dated radiocarbon sample relative to the time of deposited earthquake event. Minimum ages are interpreted as being younger than earthquake deposit while maximum ages are interpreted as being older than earthquake deposit.

*Historical dates used in Bacon age-depth model for absolute ages of known sediment intervals.

2.6.9. Variations in Transfer Functions

Four different iterations of modern training sets are used to predict past RSL (Fig. 2.8), comparing training set size and the use of priors. RSL reconstruction using informed priors on the Port Alberni and *Cascadia 2* training sets both produce similar SWLI values

lying close to one another, differing by only 1-43 SWLI (Fig. 2.8a). Uncertainties with both training sets using prior information contain the smallest uncertainties compared to training sets that do not use priors, with mean uncertainties of 22 SWLI for the *Cascadia 2* training set, and 23 SWLI for the Port Alberni training set (Fig. 2.8a). A noticeable difference when omitting priors between the Port Alberni and *Cascadia 2* training set, is that SWLI values from both training sets have large differences ranging from 14-109 SWLI (Fig. 2.8b). Uncertainties with both training sets have larger mean uncertainties compared to those with priors, with 39 SWLI for the *Cascadia 2* dataset, and 52 SWLI for the Port Alberni training set (Fig. 2.8b). The addition of priors results in a smaller uncertainty associated with their respective sea-level point, indicating better precision. This suggests that without priors, training set size greatly impacts species elevation range, resulting in different RSL reconstructions. Comparing the Port Alberni training set with and without priors, datapoints differ from one another by 4-164 SWLI (Fig. 2.8c), while the *Cascadia 2* training set has larger differences in datapoints from 1-111 SWLI (Fig.2.8d).

Four different iterations of the BTF are used to estimate the amount of coseismic subsidence above Sand 2 and Sand 1 (Table 2.3) and reconstruct RSL throughout the core. The intervals used to estimate coseismic subsidence above both sands include the last interval before the sand units (i.e., the pre-earthquake peat layer) and the intervals above the sand (i.e., the post-earthquake mud layer). We do not calculate elevation changes within the sand layers because units generated from tsunamis often transport microfossils from distant sources that do not inhabit the sampled location on land (Pilarczyk et al., 2012). Subsidence estimates are reported with 1σ uncertainties (Table 2.3).

LOI values, highest occurrence of foraminifera, and the lowest occurrence of testate amoebae are used to formally constrain the BTF as a prior to constrain former high-upland marsh zone. Modern stations containing >35% LOI, >7% of testate amoebae, and <30% foraminifera lie at MHHW, and at the maximum observed elevation at 223 SWLI. Using this constraint, sediment cores containing these attributes are given a prior of 200-223 SWLI to better constrain the former high-upland marsh zone in sediment cores.

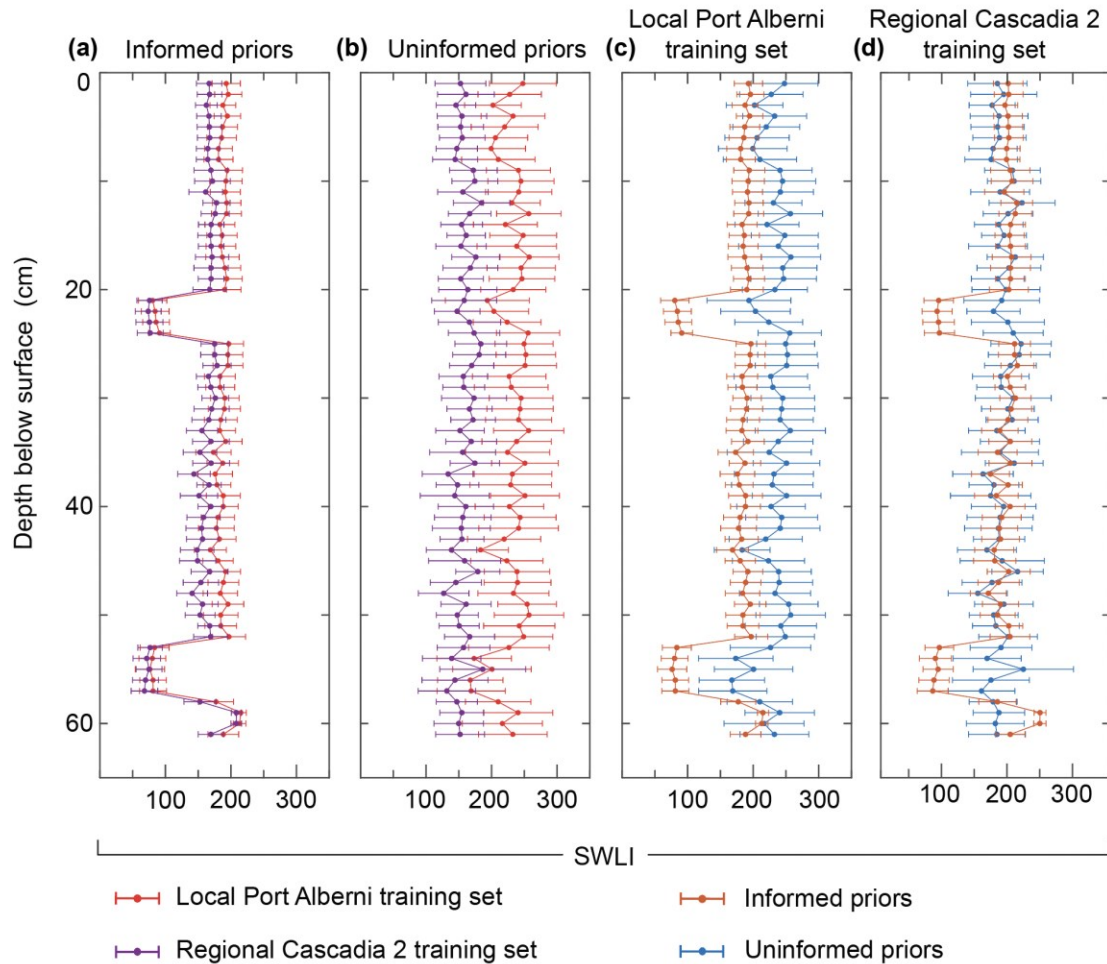


Figure 2.8. Multiple predicted paleommarsh reconstructions based on the BTF using informative priors (a) and no priors (b) for the local (Port Alberni; red dots) and regional (*Cascadia 2*; purple dots) foraminifera training sets (Fig. 2.9e).

Subsidence Estimates for Sand 2

Two sample intervals are used to calculate subsidence estimates of 20-25 cm for Sand 2 (Table 2.3). Subsidence estimates using the Port Alberni training set without priors are 18.2 ± 89 cm. Adding priors to the Port Alberni training set, subsidence estimates are 6.8 ± 41 cm, reducing estimate uncertainties. Using the regional *Cascadia 2* training set without priors, estimates are -4.6 ± 60 cm. Lastly, *Cascadia 2* training set with priors

produces estimates with smaller uncertainties of 6.9 ± 38 cm. In all instances, all estimates accompanied with uncertainties results in indistinguishable coseismic subsidence.

Subsidence Estimates for Sand 1

Using the *Cascadia 2* training set with priors, the amount of subsidence calculated at different intervals produces subsidence estimates from 53-59 cm depth of 160 ± 24 cm (Fig. 2.9, option 1), 48 ± 22 cm at 52-59 cm depth (Fig. 2.9, option 2), and 50 ± 24 cm at 51-59 cm depth (Fig. 2.9, option 2) (Table 2.3). The training sets that include priors contain the lowest uncertainties when compared to the training sets that do not included priors (Table 2.3). The *Cascadia 2* training set with prior information is used as the best model output for RSL reconstructions since it contains the lowest uncertainties of all the reconstructions (Table 2.3, Fig. 2.8)

Table 2.3. Calculated subsidence estimates based on local (Port Alberni) and regional (Cascadia 2) training sets with and without prior information.

Depth (cm)	Subsidence (cm)	Uncertainty (cm)	Sand unit	Training set	Priors
20-25	18	89	Sand 2	Port Alberni	No
20-25	6.8	41	Sand 2	Port Alberni	Informed
20-25	-4.6	60	Sand 2	<i>Cascadia 2</i>	No
20-25*	6.9	38	Sand 2	<i>Cascadia 2</i>	Informed
53-59	17	107	Sand 1	Port Alberni	No
52-59	-10	86	Sand 1	Port Alberni	No
51-59	-2.2	93	Sand 1	Port Alberni	No
53-59	160	29	Sand 1	Port Alberni	Informed
52-59-	22	32	Sand 1	Port Alberni	Informed
51-59	37	31	Sand 1	Port Alberni	Informed
53-59	-3.2	64	Sand 1	<i>Cascadia 2</i>	No
52-59	-14	63	Sand 1	<i>Cascadia 2</i>	No
51-59	5.0	59	Sand 1	<i>Cascadia 2</i>	No
53-59*	160	24	Sand 1	<i>Cascadia 2</i>	Informed
52-59*	48	22	Sand 1	<i>Cascadia 2</i>	Informed
51-59*	50	24	Sand 1	<i>Cascadia 2</i>	Informed

* Interval depths and training set that are included in Fig. 2.9.

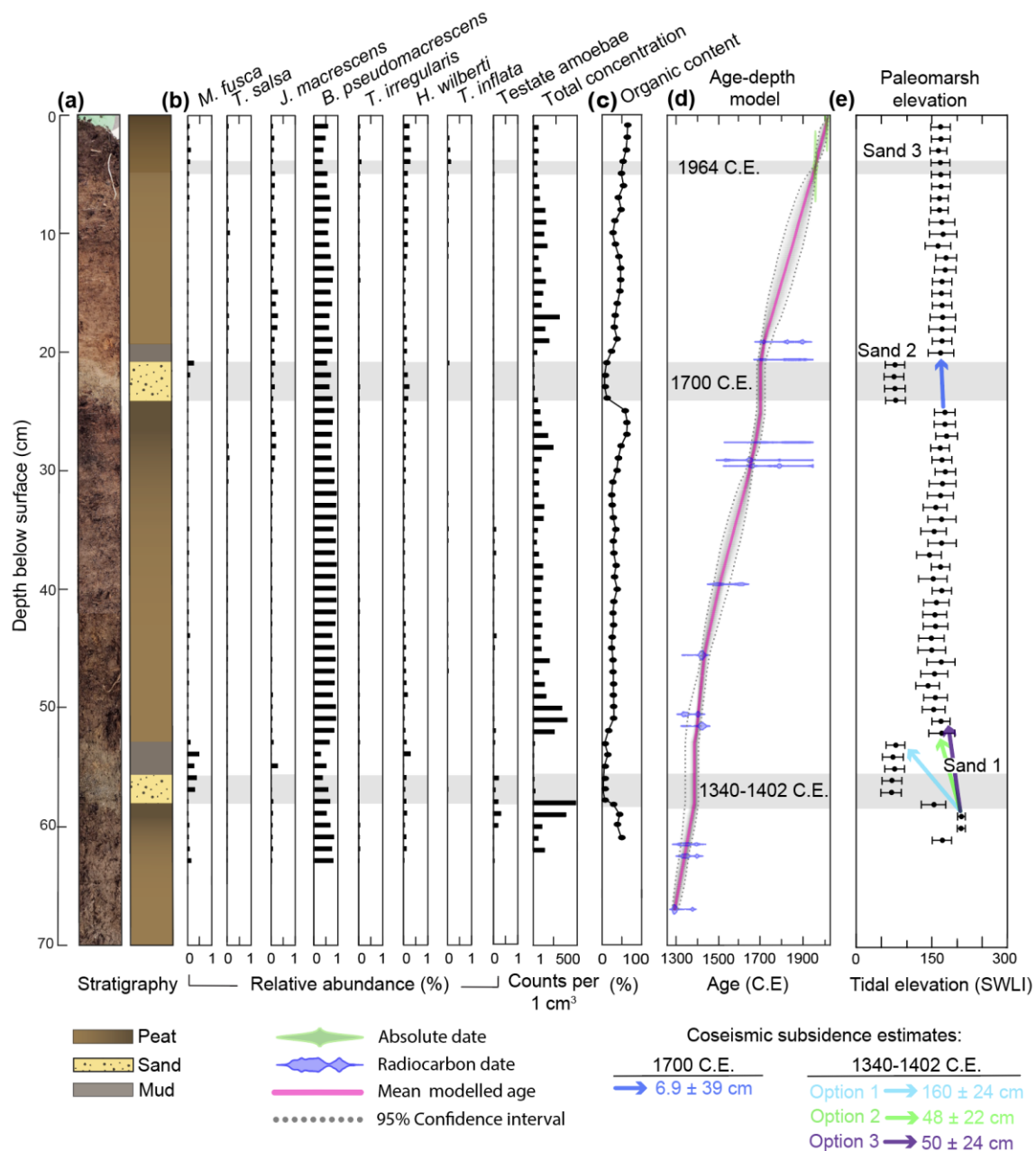


Figure 2.9. (a) Photograph and corresponding stratigraphic log for C1. (b) Relative abundance (%) of foraminifera and testate amoebae and (c) organic content. (d) Bacon age-depth model based on 12 radiocarbon samples from C1 (Fig. 2.7a). (e) Modelled paleomarrow elevation derived from an informed BTF. Backs dots indicate the tidal elevation expressed in SWLI (standardized water level index) with corresponding uncertainties. Coloured arrows indicate subsidence estimates for four possible subsidence scenarios.

2.6.10. Relative Sea-Level and Rates of Change

The RESLR relative sea-level model is used to reconstruct and determine changes in sea-level over the last 700 years (Fig. 2.10). The plotted raw data of RSL and respective modelled ages illustrate datapoints representing the sharp changes in RSL after two prehistorical events, in 1700 C.E. and another event ~600 years ago (Fig. 2.10a). Removing the pink datapoints, (Fig. 2.10b) the model indicates RSL rise of 0.41 ± 0.87 m over the last ~700 years, with an annual mean rate of 0.59 ± 0.35 mm/year (Fig. 2.10c). Annual rates of RSL rises from 1350 to the 1900s with a rate of 0.57 ± 0.32 mm/year, then accelerates to 0.69 ± 0.45 mm/year from 1900 to present day.

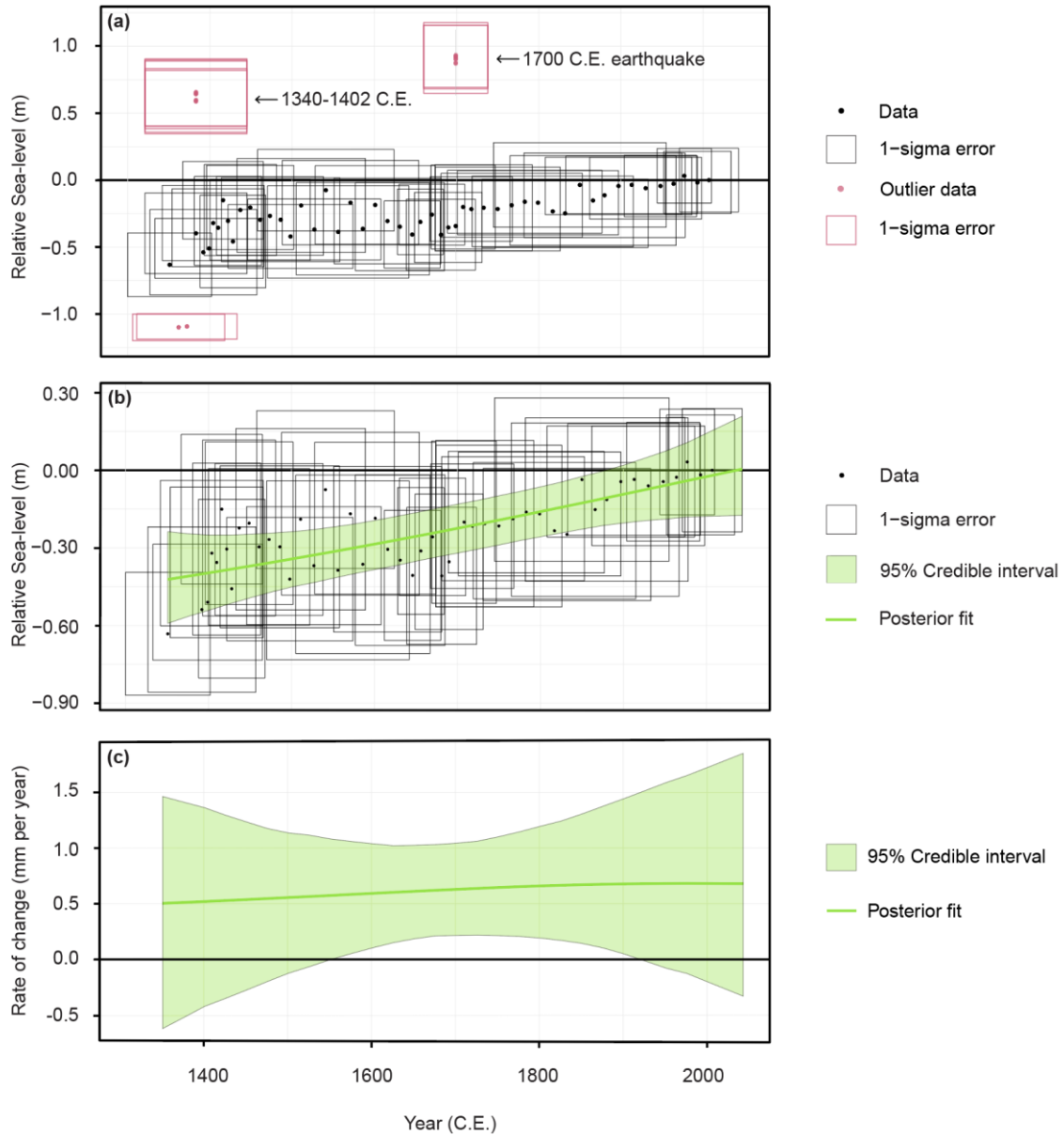


Figure 2.10. RESLR relative sea-level modelling of (a) raw data of Port Alberni (black dots) with 1 sigma error (black box) and outlier data (pink dot) with 1 sigma error (pink box). (b) Relative sea-level (m) using the Errors in variable integrated Gaussian process model over the last ~700 years (C.E.). (c) Plot of yearly rate of relative sea-level change (mm per year) with posterior fit in solid green line and 95% credible interval in light green shading.

2.7. Discussion

2.7.1. Modern Microfossil Distributions: Local and Regional Training Sets

Cascadia 2 Regional Training Set

Sea-level reconstructions are derived from proxy training sets that use modern microfossil distributions linked to tidal elevation (e.g., Guilbault et al., 1996; Horton and Edwards, 2005; Nelson et al., 2008; Kemp et al., 2009; Hawkes et al., 2010). Training sets can be local (within the same tidal frame and spaced a few kilometres apart) or regional (within different tidal frames and spaced tens to hundreds of kilometres apart) (e.g., Kemp et al., 2018; Williams et al., 2021; Garrett et al., 2022), with both potentially resulting in different sea-level reconstructions. Local training sets that span the full marsh gradient (tidal flat to upland) capture site-specific assemblages and are often associated with species-level taxonomic identification (Horton & Edwards, 2005; Wright et al., 2011). However, regional training sets capture a larger geographic range, the natural species variability attributed to environmental variables, and contain larger sample sizes; all of which contribute to a more robust modern analogue for fossil assemblages (Gehrels et al., 2001; Horton & Edwards, 2005; Hawkes et al., 2010; Watcham et al., 2013). A limitation of the regional training set is that standardized species identification from multiple sites (e.g., Horton & Edwards, 2005) requires that individual species are combined into broader genus level groups that reduces species-elevation precision (e.g., Kemp et al., 2018).

A regional training set for Cascadia salt marshes (referred to as “*Cascadia 1*” henceforth) developed by Kemp et al. (2018) consists of 393 sampled stations collected from 19 salt marsh sites from Vancouver Island to northern California. Some 37 new samples from three transects (PA1, PA2, PA3; Fig. 2.4-2.6) in Port Alberni (Vancouver Island) have been added to expand the *Cascadia 1* training set. The local training set from Port Alberni fills a spatial gap within the *Cascadia 1* regional training along a ~500 km stretch of Vancouver Island coastline.

The *Cascadia 2* regional database (Table A.4) includes the addition of the Port Alberni local training set, along with two other important updates: the removal of training

sets outside of the CSZ (e.g., Avnaim-Katav et al., 2017) and filtering the training set of Jennings and Nelson (1992) to produce a death assemblage. In general, distributions of foraminifera within the tidal frame at Port Alberni are consistent with those reported by Kemp et al. (2018), where *Miliammina fusca* is most abundant in SWLI ranges <150 and *Trochamminita* spp. and *Balticammina pseudomacrescens* abundances peak at SWLI ranges above 250. There is also agreement between the local Port Alberni dataset and the updated regional *Cascadia 2* dataset (red vs. blue dots in Fig. 2.3). In most cases, the local training set shows less variability than the broader *Cascadia 2* regional database with many sites from different environments.

To conform with the species standardization of the *Cascadia 1* database (Kemp et al. 2018), *Trochamminita irregularis* and *Trochamminita salsa* are combined into a single group (*Trochamminita* spp.) for inclusion in the *Cascadia 2* database. *T. irregularis* and *T. salsa* are similarly distributed over the Port Alberni marsh, being relatively low in abundance and found predominantly at SWLI ranges in the low and high marsh zones (Fig. A.3). Species standardization likely enhances the robustness of the training set since it combines into a single group two species that are independently low in abundance but occupy the same elevation niche (e.g., Horton and Edwards, 2005; Barlow et al., 2013).

Local Training Set for Port Alberni

A new local training set of modern salt marsh foraminifera and testate amoebae has been created for reconstructing sea-level and land-level change in Northern Cascadia. The relationship between tidal elevation and the distribution of foraminifera and testate amoebae within a salt marsh can be estimated using species flexible response curves (e.g., Cahill et al., 2016; Fig. 2.3). Flexible response curves model the natural variability of a particular species to tidal tolerances more precisely than regression-based techniques that force a species response to be either unimodal or linear (Cahill et al., 2016). Of the 6 dominant species of foraminifera found within the Port Alberni Marsh transects, species response curves for *M. fusca* reveal a skewed unimodal relationship between relative abundance and a tidal elevation of <124 SWLI. *Trochamminita* spp. and *B. pseudomacrescens* are most dominant at SWLI values <200; and *J. macrescens*, *Haplophragmoides* spp., and *T. inflata* are more abundant in the 150 to 250 SWLI range (Fig. 2.3). Using DCA and PAM cluster analysis on the microfossil data, a total of four zones within the three

transects are identified within the Port Alberni Marsh: tidal flat, tidal flat/low marsh, high marsh, and upland.

Tidal Flat Cluster

The tidal flat environment is sampled along PA1 (n = 2 stations in the tidal flat), PA2 (n = 5 stations), and PA3 (n = 4 stations), with clustering and separation from low marsh samples only in PA3 (e.g., C3.1; Fig. 2.6). The tidal flat cluster has an elevation range of 48-100 SWLI and is closely associated with low-density stands of *Zostera* sp., a seagrass common in salt marsh environments of Vancouver Island (Pojar and Alaback, 1994). LOI analysis on tidal flat sediment reveals low proportions of organic material (<12% organic) and a higher clastic/minerogenic component (Fig. 2.4-2.6). The low LOI values in the tidal flat at Port Alberni are the result of low-density vegetation and are similar to analogous environments elsewhere in coastal British Columbia. For example, Roe et al. (2009) and Douglas et al. (2022) report LOI values of 10-20% in tidal flat and low marsh environments from the Seymour-Belize Inlet Complex and Cowichan Estuary.

The concentration of testate amoebae (average concentration = 1 species/cm³) within sediments from the tidal flat cluster is among the lowest for all marsh zones. In contrast, the concentration of foraminifera (average concentration = 230 species/cm³) is higher relative to other zones within the marsh. DCA results (Fig. 2.6; C3.1) show a close association between the tidal flat cluster and *M. fusca*, a foraminifera known to inhabit low marsh to tidal flat areas that are inundated by marine waters more frequently than any other marsh zone (de Rijk, 1995). Tidal flats in Cascadia are also dominated by *M. fusca* (e.g., Jennings and Nelson, 1992; Guilbault et al., 1995; Hawkes et al., 2010). Many salt marshes in Cascadia report small abundances of calcareous species, a group of foraminifera found in marine environments (Guilbault et al., 1995; 1996; Patterson et al., 2005; Hawkes et al. 2010; Engelhart et al., 2013); however, calcareous species are not observed in samples that cluster in the tidal flat group (C3.1). Hawkes et al. (2010) suggests that low abundances of calcareous foraminifera in tidal flat areas may be the result of low pH that is often characteristic of salt marsh environments.

Tidal Flat/Low Marsh Cluster

Low marsh samples are collected from below the MHHW in all three transects: PA1 (n = 5); PA2 (n = 3); and PA3 (n = 4) (Figs. 2.4-2.6). The low marsh cluster has an elevation range higher than the tidal flat (84-197 SWLI) and contains different vegetation in terms of density and plant species. In general, the low marsh is dominated by denser stands of *Glaux maritima* and *Juncus balticus*, aquatic plant species that are often found colonizing the lower portions of tidal marshes throughout Cascadia (Clague and Bobrowsky, 1994b; Pojar and Alaback, 1994; Hong et al., 2021). Unlike clastic sediment-dominant tidal flats, surface sediment in the low marsh has a higher organic content (12-35%). The increase in LOI value from tidal flat to low marsh is indicative of an increase in organic matter from plant accumulation and decomposition (Hughes et al., 2002) and is similar to values reported in salt marshes elsewhere on Vancouver Island (e.g., Roe et al., 2009).

Although there are distinct changes in the sediment composition and plant vegetation between the tidal flat and low marsh, the microfossil assemblages show similarities, and samples from both subenvironments cluster together in the PA1 and PA2 transects (Fig. 2.4-2.5; C1.1 and C2.1). In contrast to the tidal flat samples, concentrations of foraminifera (average concentration = 189 species/cm³) are higher in the tidal flat/low marsh cluster. Diversity also increases from 8 species in the tidal flat cluster to 14 in the tidal flat/low marsh cluster.

DCA for C1.1 and C2.1 (tidal flat/low marsh clusters) group samples within this cluster close to *M. fusca*, *A. dilatatus*, *J. macrescens*, *Ammobaculites* spp., and *A. aberdoveyensis*. The extension of high abundances of *M. fusca* into the low marsh is common (Scott et al., 1996; Kemp et al., 2009; Walker et al., 2020; Williams et al., 2021; Garrett et al., 2023) and may be more pronounced at the Port Alberni Marsh due to the number of tidal channels intersecting the marsh. The presence of *A. aberdoveyensis* (Fig. 2.5; C2.1), a calcareous foraminifera that inhabits intertidal to subtidal environments, is present in the tidal flat/low marsh but not the tidal flat cluster (e.g., C3.1). This is likely why there is separation between the tidal flat and low marsh in some PAM and DCA results. Low abundances of calcareous tested foraminifera in tidal flat samples have also

been reported by others (e.g., Jennings & Nelson, 1992; Shennan et al., 1996; Patterson et al., 2005; Nelson et al., 2008; Engelhart et al. 2013).

Compared to transect PA3, the mixed assemblage comprising of low marsh and tidal flat species does not drive the separation of tidal flat and low marsh. The lack of separation between marsh zones may also be attributed to the narrow extent of the marsh system and low sample numbers collected in the tidal flat. Additional samples collected in the tidal flat may allow for a clearer separation between marsh zones. Similarly, Guilbault et al. (1995) found additional samples would have revealed clear marsh zones differentiation within their site.

High Marsh Cluster

The high marsh environment is sampled along each of the three transects at PA1 (n = 8 stations), PA2 (n = 3 stations), and PA3 (n = 2 stations). The high marsh cluster has an elevation range of 176-261 SWLI and is characterized by the most dense and diverse marsh vegetation. The upper part of the marsh at Port Alberni is dominated by species of marsh flora typical of high marsh environments, including *Carex lyngbyei*, *Potentilla pacifica*, and *Cirsium arvense*. These plants are also reported in other high marshes on Vancouver Island (Clague and Bobrowsky, 1994b; 1994b; Hughes et al., 2002; Tanigawa et al., 2021), Washington (Hong et al., 2021), Oregon (Hawkes et al., 2010), and California (Padgett et al., 2022). LOI analysis on surface samples from this subenvironment contain the highest organic values (>35%) owing to the presence of herbaceous peat. Microfossils are present in the high marsh samples, although their concentration is the lowest throughout the marsh with the exception of the upland environment outside of tidal range (average concentration of foraminifera = 53 cm³; average concentration of testate amoebae = 1 cm³).

Although concentrations are lower in the high marsh, the results of DCA reveal a distinct high marsh assemblage closely associated with *B. pseudomacrescens*, *J. macrescens*, *T. inflata*, *H. wilberti*, and *T. irregularis*. Species such as *B. pseudomacrescens* and *H. wilberti* are commonly found above MHHW in marshes across the PNW (Jennings and Nelson, 1992; Guilbault et al. 1995; Patterson et al., 1999; Riveiros et al. 2007; Nelson et al. 2008; Hawkes et al. 2010). *J. macrescens*, a species often found

near the tidal limit in marshes, is closely associated with the high marsh cluster at Port Alberni (e.g., Scott & Medioli, 1980; Gehrels, 1994; Murray and Alve, 1999; Edwards et al., 2004; Horton & Edwards, 2006; Southall et al. 2006). The distribution of *J. macrescens* is sensitive to anthropogenic impacts (Scott et al., 2001) and is a likely explanation as to why this particular species clusters near the C1.1 low marsh cluster and also near C2.2 (high marsh cluster). At the Port Alberni marsh, anthropogenic impacts associated with the nearby water treatment plant (Fig. 2.1) likely results in assemblages of *J. macrescens* that are site-specific because they are influenced by factors other than elevation within the tidal frame.

Upland cluster

The upland environment, characterized by elevations above MHHW (283 to 330 SWLI), is only sampled along PA1 (n =3). A gravel road built to service the water treatment plant confines the marsh to a defined width. In most cases, the high marsh extends up to the road, with little to no upland environment available to sample. The freshwater-dominated upland is characterized by markedly different vegetation than that of any marsh zone. *Populus balsamifera*, a freshwater deciduous tree found in disturbed upland sites (Parish & Thomson, 1994; Pojar & Alaback, 1994) is abundant in the upland section of the Port Alberni Marsh. Similar to other coastal regions in the PNW, salt intolerant trees, including *Picea sitchensis*, *Alnus rubra*, *Tsuga heterophylla*, and *Tsuga mertensiana* are the main constituents of the upland section (Hughes et al., 2002; Roe et al., 2009; Hawkes et al., 2010). Measured LOI values from upland surface sediment samples have the highest organic content (average % organic content = 66%), the result of soil formation and associated leaf litter (Hughes et al., 2001).

Of the three stations sampled in the upland environment (PA1 St. 16, 17, and 18), only station 16 contains statistically significant microfossils. In general, the total concentration of microfossils is low in this subenvironment and dominated mostly by testate amoebae (average concentration of testates = 4 cm³). Because stations 17 and 18 lacked statistically significant counts of foraminifera, they are removed from multivariate analyses (0 and 1 species, respectively). Station 16 is the only upland station that clusters,

and does so alongside station 15, the highest elevation sample from the high marsh (Fig. 2.4). DCA revealed a close association between stations 15 and 16 and the high proportions of testate amoebae. As indicators of freshwater environments in coastal and inland environments, testate amoebae are commonly found in moist and waterlogged systems, including lakes, ponds, and soils (Gehrels et al., 2001; Lloyd & Evans, 2002; Patterson and Kumar, 2002; Riou et al., 2021). By using the distributions of both foraminifera and testate amoebae in sea-level reconstructions, a full marsh gradient, from marine to intertidal to freshwater, can be captured (Gehrels et al., 2001). Modern distribution studies elsewhere in Cascadia report the occurrence of testates within salt marsh environments and, in doing so, capture the full extent of the intertidal marsh and the transition from tidally influenced to freshwater dominant (Guilbault et al. 1995, 1996).

2.7.2. Evidence for paleotsunamis and abrupt land-level change

Within the Port Alberni Marsh, three sand layers have stratigraphic features consistent with paleotsunami deposits found elsewhere in Cascadia (i.e., sharp upper and lower contacts and a wide spatial distribution; Goff et al., 2020). Two sand layers corresponding to the historical 1964 Alaska (Sand 3) and 1700 C.E. Cascadia (Sand 2) earthquakes are patchy in distribution but laterally extensive throughout the marsh over an area ~1 km². An older sand (Sand 1), deposited sometime between 1340 and 1402 C.E., is also found throughout the study area, with an overlying mud unit only observed in the northeast part of the marsh (Fig. 2.7).

The 1964 Alaska and 1700 C.E. earthquakes

Several studies have documented stratigraphic evidence for the 1964 Alaska and 1700 C.E. Cascadia earthquakes and their associated tsunamis within Vancouver Island salt marshes (e.g., Goff et al., 2020; Staisch et al., 2024). Clague and Bobrowsky (1994b) and Tanigawa et al. (2022) describe sand sheets preserved within the Port Alberni Marsh very close to the sampling sites under investigation. Both studies describe the tsunami deposit as being ~10 cm below the surface and consisting of massive, fine to medium sand with foraminifera, similar to Sand 3 in C2 (Fig. 2.7a). While Clague and Bobrowsky (1994b) infer a 1964 tsunami origin based on stratigraphic position and historical context,

Tanigawa et al. (2022) define the same deposit in Ucluelet by ^{137}Cs peaks within the sand layer and correlate it based on stratigraphic similarity to the upper sand (i.e., Sand 3) at the Port Alberni Marsh.

The 1700 C.E. tsunami deposit at Port Alberni shows similarities, as well as marked differences with the 1964 Alaska sand bed. While both deposits contain fine to medium sand with low concentrations of foraminifera, the 1700 C.E. Cascadia deposit sits at a depth of ~50 cm below the marsh surface and is generally ~5 – 7 cm thick, with similar depths and thickness reported by others (Clague and Bobrowsky, 1994b; Tanigawa et al., 2022). Clague and Bobrowsky, (1994b) and Tanigawa et al. (2022) observations of shows similar lithologic and stratigraphic trends for Sand 2 except that pebbles and thin silt-rich laminae are absent in our observations along transects 1-3 (Fig. 2.7). The modelled age for Sand 2, derived from plant macrofossils in C1, is 1682 - 1721 C.E. (Fig. 2.9, Table A.3), which is similar to Tanigawa et al. (2022), who report a modelled age of 1660-1690 C.E. for the same unit in the Port Alberni Marsh.

Stratigraphic evidence for an earthquake and tsunami ~600 years ago

At the coring sites, Sand 1 contain characteristics with the high-energy marine deposition common to tsunami deposits described from Cascadia and other temperate regions (Goff et al., 2020; Pilarczyk et al., 2021; Staisch et al., 2024). Found within most cores along the east-west transect (Fig. 2.7), the Sand 1 deposit is laterally extensive over several hundred metres and, in C1 and C2, is overlain by a thin (2-4 cm thick) grey mud layer (Mud 1). Stratigraphic logs presented in Clague and Bobrowsky (1994b) show mud units that directly overlie some of the anomalous sand units and indicate that the 1700 C.E. tsunami deposit is overlain by either a grey organic-rich mud or a brown, muddy peat depending on core location. However, previous geologic investigations of Cascadia tsunamis in the region of Port Alberni have reported no evidence for earthquake-induced land-level change within the Port Alberni Marsh (Clague and Bobrowsky, 1994b; Tanigawa et al., 2022).

Radiocarbon dates obtained from directly above and below the sand-mud unit in C1 (Fig. 2.7) provide a modelled age of 1340 – 1402 C.E. for Sand 1. In a similar study,

Tanigawa et al. (2022) use marsh stratigraphy and radiocarbon ages from the same site to develop a detailed chronology of three tsunamis, including the 1964 and 1700 C.E. events, that impacted Port Alberni. In their analysis, a sand unit underlying the inferred 1700 C.E. tsunami deposit dates to between 1330 and 1430 C.E, which overlaps considerably with our modelled age for Sand 1 (1340 – 1402 C.E.). At all three sites, radiocarbon ages that constrain the position of Sand 1 are strikingly similar and show that the tsunami deposit is widespread throughout the marsh.

Based on reported radiocarbon ages, the geographical extent of tsunami Sand 1 seems to be restricted to an earthquake in Northern Cascadia. A similar ~7 cm thick, muddy sand bed is reported in Discovery Bay along the Olympic Peninsula in Northern Washington (Williams et al., 2005; Garrison-Laney, 2017; Garrison-Laney and Miller, 2017). This sand deposited between 1320-1390 C.E (Garrison-Laney 2017; Garrison-Laney and Miller, 2017), clearly overlaps with reported ages for deposition of Sand 1 from Port Alberni. Detailed earthquake and tsunami reconstructions spanning the last few millennia have been completed south of the Olympic Peninsula; however, none report a sand sheet within this age range. The limited spatial distribution for the tsunami some 600 years ago suggests the triggering earthquake was smaller than the 1700 C.E. great earthquake, but large enough to generate a tsunami that impacted at least a 100 km stretch of coastline in Northern Cascadia.

Implications for understanding source mechanisms of Cascadia earthquakes

Sea-level reconstructions are established using modern sea-level indicators (i.e., foraminifera) to derive past sea-level changes using time-invariant assemblages in sediment cores. To quantify past sea-levels, mathematical transfer functions relate current day tidal information and foraminifera assemblages to observed trends in cores (Cahill et al., 2016). The use of transfer functions has been applied to tectonic coastlines where coseismic subsidence results in abrupt changes in sea level (Guilbault et al., 1996; Nelson et al., 2008; Hawkes et al., 2010; 2011; Engelhart et al., 2013; Kemp et al., 2018; Nelson et al., 2020; Padgett et al., 2022).

Transfer functions previously applied to marsh sediments from coastal locations in Cascadia are used to quantify the amount of coseismic subsidence with uncertainties of $0.3 - 0.5\text{ m}$ (e.g., Guilbault et al., 1995, 1996; Nelson et al., 2008; Hawkes et al., 2010, 2011; Engelhart et al., 2013; Wang et al., 2013). Cahill et al. (2016) developed a BTF incorporating a flexible species-response curve that better captures the relationship between foraminiferal assemblages and tidal frequency when compared to previous models that force species elevation optima into a unimodal Gaussian curve. Most notably, the Bayesian framework formally incorporates prior information using multiple proxies for elevation (e.g., a secondary microfossil group and LOI). It is on this basis that the BTF is employed to determine whether the Port Alberni Marsh subsided during the 1700 C.E. earthquake, and the earlier event approximately 600 years ago that deposited sand and mud layers from Northern Washington to at least as far north central Vancouver Island.

Using the *Cascadia 2* training set with informed priors for the 1700 C.E. earthquake estimates a land-level change of $6.9 \pm 38\text{ cm}$ (Fig. 2.9e, Table 2.3). This small value, accompanied with its large uncertainty, indicates a minimal to indistinguishable amount of subsidence. Three other variations of the BTF produce similar amounts of subsidence for the 1700 C.E. earthquake (Table 2.3). This new reconstruction indicates the 1700 C.E. earthquake generates a large tsunami, consistent with previous research in the area (e.g., Clague and Bobrowsky, 1994b; Clague et al., 1994; Hutchinson et al., 2017; Tanigawa et al., 2022), but does not cause significant coseismic subsidence at Port Alberni.

Elsewhere, evidence of coseismic subsidence on Vancouver Island following the 1700 C.E. earthquake records 39-102 cm of subsidence at Tofino and 29-80 cm at Meares Island (Guilbault et al., 1996). While subsidence estimates in this study greatly differ to those of Guilbault et al. (1996), this difference is attributed to the location of sites relative to the deformation front: Tofino is 2.5 km and Meares Island is <math><5\text{ km}</math> inland of the CSZ off Vancouver Island. Subsidence estimates at Port Alberni align with earthquake models such as Leonard et al. (2004, 2010), which use turbidite, stratigraphic evidence of marsh displacement, and dislocation model prediction. Leonard et al. (2010) uses stratigraphic evidence of mud from Clague and Bobrowsky (1994b) to estimate subsidence of $10 \pm 50\text{ cm}$. Results from this new study agree with the modeled estimates of Leonard et al. (2010)

while further improving coseismic subsidence estimates by decreasing the uncertainties to ± 38 cm.

Changes in RSL using the *Cascadia 2* training set with priors for Sand 1 at different depths below surface (53, 52, and 51 cm) result in subsidence estimates of 160 ± 24 cm (option 1), 48 ± 22 cm (option 2), and 50 ± 24 cm (option 3), respectively (Fig. 2.9). These findings highlight that reconstructions can have highly variable results depending on the interval chosen, raising questions regarding which interval to choose that best reflects the post-seismic interval. Milker et al. (2022) suggest sampling a few centimetres above the peat-mud contact at sites with high postseismic sedimentation rates (i.e., tsunami inundation), low abundances, and unrepresentative foraminiferal assemblages. Statistically significant counts of foraminifera for decadal-scale RSL reconstruction should contain >75 tests (Kemp et al., 2020). The interval at 53 cm depth (option 1) does not contain a statistically significant concentration of foraminifera (2 species/cm^3), so is not considered a reasonable post-seismic sample for calculating subsidence. The absence of environmental indicators, including drowned trees and mud above the peat (<3 cm) suggest that subsidence estimates of over 160 cm are unlikely (i.e., Nelson et al., 2020). Options 2 and 3 both contain statistically significant concentrations of fossils at 237 species/cm^3 and 382 species/cm^3 , respectively, suggesting around 50 cm of rapid subsidence and deposition of an extensive tsunami sand sheet across the Port Alberni Marsh during a large magnitude seismic event between 1340 and 1402 C.E.

The limited geographical extent of the 1340-1402 C.E. tsunami sand suggests a partial rupture of the CSZ over multiple decades extending from Vancouver Island to Northern Washington, in contrast to full trench rupture along the Cascadia fault in 1700 C.E. This scenario is consistent with Melgar's (2021) multi-earthquake sequence model, which indicate Cascadia may produce more than one single long rupture, such as a series of shorter ones. The addition of new paleoseismic data for the event between 1340-1402 C.E. have important implications for understanding the different plate-boundary processes accompanying Cascadia earthquakes. However, as this is the first estimate of land-level change in Northern Cascadia, more estimates from Vancouver Island and Washinton will

be needed to establish whether or not the 1340-1402 C.E. and 1700 C.E. are part of a multi-earthquake rupture sequence.

Competing interpretations of the mud layer overlying Sand 1

Mud caps are common features associated with tsunami deposits (e.g., Atwater et al., 2011; Pilarczyk et al., 2012; Ishizawa et al., 2019), and result when wave-transported sediment with a range of grain sizes settles out of suspension (Jaffe and Gelfenbaum, 2007). Mud caps can be stratigraphically thin (usually less than a few cm), are easily bioturbated, and often indistinguishable from overlying tidal or fluvial muds (Bondevik et al., 1997; Ishizawa et al., 2019). In the Port Alberni Marsh, the Mud 1 layer directly overlying Sand 1 ranges in thickness from 2 to 3 cm and is more than half the thickness of the underlying sand. Given that mud caps are typically a thin veneer overlying a sandy tsunami deposit, the relative thickness of the mud in C1 and C2 is unusual. Furthermore, the mud cap is devoid of laminations and organic material; common constituents of tsunami-deposited muds. The microfossil assemblages of the mud unit are dominated by *M. fusca*, a foraminifera that commonly inhabits low marsh and tidal flat environments (Scott et al., 1996; Guilbault et al., 1995; 1996; Patterson et al., 2005; Hawkes et al., 2010; Engelhart et al., 2013; Graehl et al., 2015), and a near complete absence of testate amoebae (Fig. 2.9). By contrast, Sand 1 contains a mixed assemblage of agglutinated foraminifera and testate amoebae. Tsunami sediments often contain a mixed microfossil assemblage that results from the erosion, transport, and deposition of sediments from multiple point sources (Pilarczyk et al., 2014). The absence of testate amoebae (a fresh- to brackish-water microfossil) in the mud cap is inconsistent with a mixed microfossil assemblage associated with tsunami deposition, and rather more aligned with a tidally deposited layer following coseismic or afterslip subsidence prior to interseismic uplift.

Post-depositional change within marshes often manifests as infaunal mixing and tidal channel infilling. Peat from the high marsh is often porous and allows for the downward mixing and infilling of lower elevation sediments (i.e., those derived from the tidal flat and low marsh) into high marsh peat following coseismic subsidence (e.g., Milker et al. 2016). This process can potentially bias the earthquake record through the mixing of the pre- and post-earthquake assemblages, and generally results in an underestimation of

the magnitude of subsidence (e.g., Engelhart et al., 2013). Post-depositional mixing also has the potential to artificially overestimate coseismic subsidence. The position of tidal channels eroded by tsunami inundation along the coastline can result in infilling of tidal mud linked to sediment transport by the channel itself and not land-level change (Peters et al., 2007). Within the cores collected from the Port Alberni Marsh, post-depositional change is stratigraphically evident and appears to be attributed in large part to bioturbation. Given the computed estimates for subsidence, it is more likely that post-depositional change results in an overestimation of land-level change; however, estimates from additional cores throughout the marsh are needed to confirm this postulation.

Along warm-slab subduction zones, such as the CSZ and the Nankai Trough, the gap between the seismogenic and Episodic Tremor and Slip (ETS) zones are prone to large afterslip events (Luo and Wang, 2022). The results of this study support various dislocation models indicating minimal to no subsidence at the landward extent of the Alberni Inlet during the 1700 C.E. Cascadia earthquake and deposition of tsunami Sand 2 (Leonard et al., 2004; Wang et al., 2013). In contrast, while the possibility exists that the 3 cm-thick mud layer directly overlying tsunami Sand 1 is attributed to earthquake-induced coseismic subsidence, aftershocks or continuing slip of the megathrust surrounding the rupture zone cannot be excluded. For example, pre- and post-seismic subsidence stratigraphic signals are reported by Sawai et al. (2004) and Natawidjaja et al. (2007). Luo and Wang (2022) show that afterslip associated with the 1700 C.E. earthquake can readily produce subsidence as far inland as Port Alberni if the assumed afterslip extends farther down the subducting slab, or if the slip magnitude is larger. Subsidence at Port Alberni associated with the 1340 to 1402 C.E. may have occurred instantaneously and coseismically, or over several years as a consequence of interseismic afterslip. While both mechanisms have direct impacts on short-term RSL change for coastal communities, the former has implications for paleoearthquake reconstructions, including the assessment of magnitude and rupture extent.

2.7.3. Relative Sea-level Rise at Port Alberni Over the Last Few Centuries

RSL change along western Vancouver Island is predominantly the net effect of eustatic factors, ocean dynamics, tectonic activity (i.e., instantaneous coseismic subsidence and slow interseismic uplift), hydro-isostatic and glacioisostatic (GIA) adjustment (Dura et al., 2016). Short scale (individual seismic cycle) interseismic uplift rates on Vancouver Island display 1-2 mm/yr with a maximum uplift rate at 5 mm/yr, while long term (over multiple seismic cycles) suggests 1 mm/yr of interseismic rates (Bodner et al., 2020). Sea level reconstructions from Cascadia capture millennial-scale changes since the Last Glacial Maximum and point to heterogeneous post-glacial RSL trends, largely linked to distance from the former Cordilleran Ice Sheet (e.g., Shugar et al., 2014). RSL heterogeneities on Vancouver Island indicate glacioisostatic rebound was mostly complete thousands of years ago and is now no longer a major contributor to sea level change (Benson et al., 1999; Shugar et al., 2015). Instead, eustatic and tectonic drivers have the greatest influence at Port Alberni. Millennial-scale sea-level reconstructions provide important insight into broadscale trends associated primarily with deglaciation (e.g., Shugar et al., 2015; Lethem et al., 2024). Centennial-scale records capture short-term climatic variations such as the Little Ice Age (Long et al., 2012), and instantaneous changes in RSL associated with earthquake-induced subsidence and rebound (Nelson et al., 2008; Hawkes et al., 2010; 2011; Engelhart et al., 2013).

The variability in postglacial RSL along the coast has an important influence on the preservation potential of earthquake and tsunami stratigraphy. Tectonic uplift and GIA in near-field regions (e.g., Vancouver Island, British Columbia to Northern Washington) contribute to a fall in RSL from ~6 ka to 1 ka, limiting accommodation space (Dura et al., 2016). The slowly falling RSL through the middle and late Holocene results in the minimal burial of low elevation soils and exposure to terrestrial and marine erosional processes. The increased reworking of coastal sediments in Northern Cascadia resulting from the fall in RSL over this approximately 5000-year interval impacts the preservation potential of deposits associated with paleoearthquakes and paleotsunamis (Dura et al., 2016).

Given its location at the landward terminus of the 78 km-long Alberni Inlet, the coastal city of Port Alberni is expected to have a distinctly different Common Era sea-level history compared to the majority of other coastal locations that are closer to the subduction zone and that subsided by larger amounts during past megathrust earthquakes. A centennial-scale history of RSL at this unique location, using the R software package “RESLR”, yields an annual mean rate of sea-level change of 0.59 ± 0.35 mm/year over the last ~700 years (Fig. 2.10). Rates of RSL rise increase in the 1900’s to present day, with an average rate of 0.69 ± 0.35 mm/year over the last 100 years at Port Alberni. The accelerated rates from 1900’s to present day suggest an increase in RSL from 20th century eustatic sea-level change and thermal expansion (He et al., 2022). However, this rate differs from the 20th Century global mean rate of 1.5 mm/year (1901 to 1971) and an accelerated rate of 3.7 mm/year from 2006 to 2018 (Masson-Delmotte et al., 2021; He et al., 2022). These reconstructions have important implications for the RSL history of Port Alberni and assist in a better understanding of RSL trends during interseismic periods that are largely influenced by crustal tectonic uplift and 20th century ocean thermal expansion (He et al., 2022).

2.8. Conclusions

This study describes the modern distribution of salt marsh foraminifera and testate amoebae in Port Alberni, British Columbia (Northern Cascadia) using 37 surface samples collected from three transects spanning the full marsh gradient from tidal flat to the upland environment. PAM cluster analysis generally groups the microfossil data into clusters corresponding to tidal flat, tidal flat/low marsh, high marsh, and upland environmental zones. Modern microfossil data from Port Alberni is incorporated into the regional Cascadia foraminifera database, originally reported by Kemp et al. (2018). The revised database, referred to as *Cascadia 2*, is used to reconstruct paleommarsh elevation from an Eijkelkamp Russian core spanning the last 700 years. To produce the most precise reconstruction, four scenarios are tested with a BTF: a local training set with and without prior information, and a regional training set with and without priors. The regional

foraminifera training set (*Cascadia 2*) is determined using a combination of three priors (lowest occurrence of testate amoebae, highest occurrence of foraminifera, and LOI) in order to limit the uncertainty.

Microfossil evidence consistent with coseismic subsidence of 48 ± 22 cm associated with the tsunami sand (Sand 1) and overlying mud layer (Mud 1) deposited sometime between 1340 and 1402 C.E. This older sand-mud couplet is found across the Port Alberni Marsh, but is also observed as far north as Tofino, British Columbia, and as far south as Discovery Bay, Northern Washington, USA. The stratigraphic features of Sand 1 and overlying Mud 1 layer are consistent with tsunami deposits described elsewhere in Cascadia (i.e., Clague and Bobrowsky, 1994b; Garrison-Laney 2017; Garrison-Laney and Miller, 2017; Tanigawa et al., 2022); but their spatial extent, limited to Northern Cascadia, suggests a different rupture mechanism to the great 1700 C.E. earthquake and tsunami. Alternative explanations for an origin of the mud layer directly overlying Sand 1 include the formation of a mud cap deposited during the waning stages of a tsunami, marine inundation following coseismic subsidence, subsidence related to afterslip of the subducting plate during the interseismic period, post-depositional infaunal mixing, and infilling by fluvial and tidal channels during storm events. The thickness of Mud 1, combined with the lack of stratigraphic and microfossil evidence for tsunami deposition favour a subsidence origin for the mud. However, the distance from the subduction zone makes it challenging to distinguish between earthquake- (i.e., coseismic) and afterslip- (i.e., interseismic) induced subsidence. The amount of coseismic or interseismic subsidence provides insight into the parent earthquake in terms of magnitude and rupture extent. However, biostratigraphic evidence for coseismic subsidence accompanying the 1700 C.E. earthquake, and the resulting tsunami sand (Sand 2) and mud cap (Mud 2) is absent.

BTFs using the modern training set of foraminifera, testate amoebae, and elevation, are used to statistically relate surface death assemblages to their analogous fossil record found in sediment cores. Transfer functions allow for a continuous record of sea-level change that, in coastal locations such as Cascadia, may capture full earthquake cycles (Fig. 1.4). Over the past 700 years, RSL at Port Alberni has risen at an annual mean rate of 0.59 ± 0.35 mm/year (95% confidence interval). Over the past 200 years, sea-level at this site

accelerated to a rate of 0.69 ± 0.45 mm/yr from tectonic activity, ocean thermal expansion, and eustacy. This rate is significantly less than the global rate of sea-level rise for the same time period, which exceeds 4 mm per year (Masson-Delmotte et al., 2021; He et al., 2022). The past events discussed in this study help inform scenarios for future crustal responses when land subsidence associated with a great earthquake (i.e., a coseismic event), or as a consequence of afterslip between the subducting plates (i.e., an interseismic event) will be problematic for coastal communities, resulting in relatively abrupt changes in sea level and temporary flooding of low-lying areas with vulnerable populations and socioeconomic infrastructure.

Chapter 3.

Conclusions and Future Work

3.1. Conclusions

Three timely objectives addressed in this thesis are: (1) to determine, from surface sampling, if modern foraminifera and testate amoebae zonate within the tidal frame, and whether these microfossils can be used as a training set to reconstruct RSL; (2) to resolve whether Port Alberni, British Columbia, Canada, has experienced coseismic subsidence during past Cascadia earthquakes through lithologic, stratigraphic, and chronological analysis of cores; and (3) to develop a RSL history for Port Alberni that quantifies annual rates of change. Biological proxies (foraminifera and testate amoebae), stratigraphic information, LOI, BTFs, and a Bayesian age-depth model are combined to reconstruct the last 700 years of RSL change at Port Alberni.

The Port Alberni local training set consisting of 37 surface samples that indicate modern assemblages zonate within the vegetated marsh in relation to tides. Multivariate statistical analysis (PAM and DCA) indicates four elevation-dependent zones: (a) a tidal flat dominated by *Miliammina fusca*; (b) a tidal flat/low marsh cluster dominated by *Miliammina fusca*, *Ammobaculites* spp., and *Jadammina macrescens*; (c) a high marsh dominated by *Balticammina pseudomacrescens*, *Haplophragmoides wilberti*, and *Trochammina inflata*; and (d) an upland, dominated by freshwater testate amoebae. This zonation is similar to the microfaunal distributions observed in salt marshes elsewhere along the PNW coast of North America.

As part of the thesis the *Cascadia 1* regional database developed by Kemp et al. (2018) is now updated. The Port Alberni training set is incorporated into the *Cascadia 2* training set, a database of modern transects from salt marshes spanning from Port Alberni, Vancouver Island to southern Coquille River, Oregon. The three transects in this study provide an important update by expanding the spatial cover of training sets. Resolution has been improved by removing training sets outside of the CSZ (i.e., south of the Gorda Plate),

and filtering training sets with total counts of foraminifera to include dead assemblages only (Table A.4). The updated *Cascadia 2* training set currently includes 395 station samples, 20 sites, and spans 2 countries. This expanded training set has a larger geographical extent, and better captures the natural variability of modern assemblages along Cascadia. An improved training set allows for more robust RSL reconstructions and coseismic subsidence estimates that will ultimately reinforce models of future earthquake ruptures in the PNW.

Cores recovered transects contain up to three subsurface sand layers sharply overlying interseismic peats (Fig. 2.7). In C2, the uppermost Sand 3 (<1 cm thick) occurs less than 10 cm below the modern marsh surface, and is the deposit associated with the 1964 C.E. Aleutian great earthquake (Sawai et al., 2020; Tanigawa et al., 2022; Fig. 2.7a). In C1 recovered from transect PA1 (Fig. 2.7a), Sand 2 (~20 cm depth; 4 cm thick) and Sand 3 (~55 cm depth; 4 cm thick) are overlain by organic-rich muds (Mud 3, 1 cm thick; Mud 2, 3 cm thick) that grade upward into peat. The occurrence of two sand-mud units interbedded with peat is consistent with onshore deposition from large earthquake-triggered paleotsunamis.

The two different training sets (Port Alberni [local] and *Cascadia 2* [regional]), accompanied with informative priors (loss-on-ignition, highest occurrence of foraminifera, and lowest occurrence of testate amoebae) in the BTF, are used to reconstruct paleomorph elevation from C1 (Fig. 2.7a). The local training set with and without priors, and regional training set with and without priors are tested to determine the most precise RSL reconstruction. A BTF using the *Cascadia 2* training set *with* priors reduces subsidence uncertainties the most (Fig. 2.8).

Modelled Bayesian (Bacon) ages for Sand 2 average from 1692-1751 C.E. This age range compares well with dates, stratigraphic evidence, and geographic extent of sand deposits reported elsewhere in the CSZ (e.g., Clague and Bobrowsky, 1994a; Sawai et al., 2020; Tanigawa et al., 2022), implying tsunami Sand 2 correlates with the 1700 C.E. subduction zone rupture (Fig. 2.9). Bacon modelled ages for Sand 3 range from 1340-1402 C.E. (Fig. 2.9), overlapping with ages of sand deposits in Ucluelet-Tofino (Tanigawa et al.,

2022), and Discover Bay (Garrison-Laney 2017; Garrison-Laney and Miller, 2017). The overlapping ages are confined to Northern Cascadia, suggesting this 600-year event was restricted to a rupture zone extending from Vancouver Island to Northern Washington (e.g., Walton et al., 2021).

These findings provide temporal constraints on estimates of coseismic subsidence associated with tsunami sands, building on the work of Hutchinson and Clague (2017). Estimates of coseismic subsidence associated with the 1700 C.E. earthquake using the *Cascadia 2* training set with priors produces minimal to no subsidence (6.9 ± 39 cm) during deposition of Sand 2 and Mud 2. In contrast, the earthquake approximately 1340-1402 C.E. yields subsidence estimates between 48 ± 24 cm within Sand 3 and Mud 3. The spatial extent of this older event extends from Vancouver Island to Northern Washington, suggesting a partial rupture limited to the Northern part of the CSZ that was large enough to trigger coseismic subsidence and tsunami inundation at Port Alberni. Alternative explanations for Mud 3 layer above Sand 3 include a tsunami-generated mud cap, post-depositional changes and infaunal mixing in an ephemeral tidal channel, or subsidence accompanying interseismic afterslip following the coseismic period. If the 1340-1402 C.E. event is the result of a Northern Cascadia rupture, then the seismic hazards and recurrence intervals will differ from previous estimates.

Understanding the RSL history of Port Alberni helps to better constrain the complex changes in the postglacial and late Holocene paleogeography of Vancouver Island. Changes in RSL through time in C1 were resolved by using the RESLR relative sea-level model and BTFs of modern training sets to statistically relate surface assemblages to their analogous fossil record found in the stratigraphic record. BTFs allow for a continuous record of sea-level change that capture full earthquake cycles (Hawkes et al., 2011). In this study, changes in sea-level over the last 700 years are reconstructed, with plotted raw data and respective modelled ages capturing sharp RSL change after two prehistorical events (Fig. 2.10a). At Port Alberni, RSL rose at an average rate of 0.59 ± 0.35 mm/year (95% confidence interval) over the last 700 years. Beginning in the 20th Century and continuing today, the rate of RSL change has increased to 0.69 ± 0.45 mm/year. This mean value is less than the global predicted rate of ~ 4 mm/year for the 20th

Century. This study adds critical datapoints to the sparse records of coseismic subsidence on Vancouver Island and will help to improve CSZ earthquake models. Modelled age-depth estimates from C1 refine the reoccurrence rate of great earthquakes and tsunami events prior to 1700 C.E. Port Alberni, located far inland on Vancouver Island, records no significant land-level change resulting from the 1700 C.E. earthquake. This is in contrast to an increase in RSL following the 1340-1402 C.E. event. Contrasting subsidence estimates have broad implications for CSZ plate boundary behaviour. This study supports a full-trench heterogeneous rupture model at 1700 C.E. (e.g., Wang et al., 2013), but results for the 1340-1402 C.E. event suggest the multiple-rupture sequence model of Melgar (2021) is pertinent, with the CSZ producing smaller ruptures over multiple decades.

This study refines the seismic hazard (magnitude and reoccurrence interval) for Vancouver Island and helps validate current full-trench or multi-rupture rupture models. The improved spatial and chronological resolution of lithostratigraphic and microfossil records from Port Alberni will help coastal communities and populations better prepare for future seismic hazards along the CSZ.

3.2. Future work

With the thesis objectives achieved, additional geologic investigations will further improve coastal hazard assessments along the Northern part of Cascadia. Three recommendations and future study directions compliment the research objectives accomplished in this thesis. Avenues for future research include: (1) further refinement of the *Cascadia 2* training set through the addition of more modern foraminifera training sets from Northern Vancouver Island; (2) incorporating oral histories of Indigenous communities on Vancouver Island that document the 1700 C.E. and older events along the northernmost extent of the CSZ; and (3) mapping and quantification of coseismic and, or afterslip subsidence resulting from the 1340-1402 C.E. event in Northern Cascadia. Incorporating Indigenous knowledge and oral records with the traditional and innovative methods of Western science will strengthen the predictive power of current rupture models of Cascadia to better represent future events.

The great 1700 C.E. earthquake is the most intensively mapped paleoearthquake along the PNW coast of North America. Some 59 sites contain tsunami records (Peters et al., 2003; Goff et al., 2020), 14 RSL reconstructions use foraminifera to quantify coseismic subsidence (Kemp et al., 2018), and 40 known sites contain oral histories (Ludwin et al., 2005; Goff et al., 2020). These extremely robust datasets contribute to the refinement of rupture models for the 1700 C.E. great earthquake and understanding of plate boundary processes along the CSZ.

The 1700 C.E. event was initially modelled as a homogenous rupture with uniform slip along the entire Cascadia fault zone (Wang et al., 2013). With the addition of more high-resolution geological evidence from numerous, spatially separated sites, and statistical advancements, more realistic rupture models now better represent the available geologic data. Nevertheless, there are still gaps in the modern foraminifera dataset at the northernmost extent of CSZ on Vancouver Island. The addition of a Port Alberni modern foraminifera dataset into an updated *Cascadia 2* training set addresses this knowledge gap, but improvements can always be made. Additional modern foraminifera training set from northern Vancouver Island and coastal British Columbia will better delimit the spatial extent and dynamics of the CSZ. Expanding and extending the modern foraminifera training set in northern CSZ will help to refine RSL reconstructions and quantify the extent of rupture and coseismic subsidence associated with the 1700 C.E. event.

Site selection is an important consideration when extending the *Cascadia 2* training set in the northern part of Cascadia. Recognizing field sites with known oral records that document the 1700 C.E. event in long-standing First Nations communities will lead to better integration of Indigenous knowledge with geologic evidence, and direct researchers to important locations to be incorporated in hazard maps and models. Goff et al. (2020) mention the many oral histories that document the 1700 C.E. event in coastal British Columbia, but these contain no quantified geologic evidence of earthquakes and tsunamis. The northernmost locations containing oral histories of the 1700 C.E. earthquake is on the lands of the Nuxalk Nations (mainland British Columbia, Bella Coola), Wuikinuxv Nation (Mainland British Columbia, Oweekeno), and Kwakwaka'wakw First Nations (Vancouver Island, Alert Bay) (Goff et al., 2020). Nuxalk and Wuikinuxv Nations, for example,

document histories of water covering the country, while peoples of the Sheshaht Nation (Port Alberni, Vancouver Island) drifted in their canoes to distant parts (Thrush & Ludwin, 2007). The oral histories of these coastal dwellers document serious flooding and strong waves that may be preserved in the geologic record, and that can be quantified and used for hazard assessment. Focusing on field sites previously unaccounted for in CSZ rupture models will help Indigenous communities to be better prepared for future events, guided by their oral histories and verified with modern geoscience methods.

When compared to the 1700 C.E. great earthquake, the 1340-1402 C.E. event does not contain a wealth of geological information. The geographic extent is currently restricted to central Vancouver Island and Northern Washington (Clague and Bobrowsky, 1994b; Clague et al., 2000; Williams et al., 2005; Garrison-Laney, 2017; Garrison-Laney and Miller, 2017; Tanigawa et al., 2017; Goff et al., 2020; Tanigawa et al., 2022). The addition of reconstructions that map and quantify coseismic subsidence in the northern part of CSZ will confirm whether the 1340-1402 C.E. event was part of the northern-wide rupture proposed by Melgar (2021).

In conclusion, I believe the intentions for writing science are to carve a path for future researchers, and to consider who benefits from such earthly knowledge and how geoscience is used applied for safer communities and resilient infrastructure. This thesis provides answers that contribute local understanding to a regional coastal hazard mystery. The addition of a modern foraminifera database and training set to the CSZ database, in combination with oral histories from Indigenous communities leads to a better understanding of prehistorical earthquake hazards on Vancouver Island. Incorporating field sites at the northernmost extent of the CSZ helps to quantify tsunami inundation and coseismic subsidence associated with the 1700 C.E. and 1340-1402 C.E. earthquakes on the west coast of Vancouver Island.

I hope that my master's thesis inspires you, the reader, to continue (or start) your creative and impactful journey in science.

References

- Aguirre, B. E. (2018). A retrospective account of the impacts of the 1960 Valdivia, Chile, earthquake and tsunami and the lack of business continuity planning. (1st ed). Routledge. <https://doi.org/10.4324/9781315629520-6>
- Ao, Y., Zhang, H., Yang, L., Wang, Y., Martek, I., & Wang, G. (2021). Impacts of earthquake knowledge and risk perception on earthquake preparedness of rural residents. *Natural Hazards*, 107(2), 1287–1310. <https://doi.org/10.1007/s11069-021-04632-w>
- Atwater, B. F. (1987). Evidence for great Holocene earthquakes along the outer coast of Washington state. *Science*, 236(4804), 942–944. <https://doi.org/10.1126/science.236.4804.942>
- Atwater, B. F. (1992). Geologic evidence for earthquakes during the past 2000 years along the Copalis River, southern coastal Washington. *J. Geophys. Res.*, 97(B2), 1901–1919. <https://doi.org/10.1029/91JB02346>.
- Atwater, B. F. (Ed.). (2005). The orphan tsunami of 1700: Japanese clues to a parent earthquake in North America. U.S. Geological Survey; In association with University of Washington Press.
- Atwater, B. F., & Hemphill-Haley, E. (1997). Recurrence intervals for great earthquakes of the past 3,500 years at northeastern Willapa Bay, Washington. USGS Professional Paper, 1576. <https://doi.org/https://doi.org/10.3133/pp1576>
- Atwater, B. F., Nelson, A. R., Clague, J. J., Carver, G. A., Yamaguchi, D. K., Bobrowsky, P. T., Bourgeois, J., Darienzo, M. E., Grant, W. C., Hemphill-Haley, E., Kelsey, H. M., Jacoby, G. C., Nishenko, S. P., Palmer, S. P., Peterson, C. D., & Reinhart, M. A. (1995). Summary of coastal geologic evidence for past great earthquakes at the Cascadia subduction zone. *Earthquake Spectra*, 11(1), 1–18. <https://doi.org/10.1193/1.1585800>
- Atwater, B. F., Ten Brink, U. S., Buckley, M., Halley, R. S., Jaffe, B. E., López-Venegas, A. M., Reinhardt, E. G., Tuttle, M. P., Watt, S., & Wei, Y. (2012). Geomorphic and stratigraphic evidence for an unusual tsunami or storm a few centuries ago at Anegada, British Virgin Islands. *Natural Hazards*, 63(1), 51–84. <https://doi.org/10.1007/s11069-010-9622-6>
- Avnaim-Katav, S., Roland Gehrels, W., Brown, L. N., Fard, E., & MacDonald, G. M. (2017). Distributions of salt-marsh foraminifera along the coast of SW California, USA: Implications for sea-level reconstructions. *Marine Micropaleontology*, 131, 25–43. <https://doi.org/10.1016/j.marmicro.2017.02.001>
- Ball, D. F. (1964). Loss-on-ignition as an estimate of organic matter and organic carbon in non-calcareous soils. *Journal of Soil Science*, 15(1), 84–92. <https://doi.org/10.1111/j.1365-2389.1964.tb00247.x>

- Barlow, N. L. M., Shennan, I., Long, A. J., Gehrels, W. R., Saher, M. H., Woodroffe, S. A., & Hillier, C. (2013). Salt marshes as late Holocene tide gauges. *Global and Planetary Change*, 106, 90–110. <https://doi.org/10.1016/j.gloplacha.2013.03.003>
- Benson, B. E., Clague, J. J., & Grimm, K. A. (1999). Relative sea-level change inferred from intertidal sediments beneath marshes on Vancouver Island, British Columbia. *Quaternary International*, 60(1), 49–54. [https://doi.org/10.1016/S1040-6182\(99\)00006-3](https://doi.org/10.1016/S1040-6182(99)00006-3)
- Benson, B. E., Grimm, K. A., & Clague, J. J. (1997). Tsunami deposits beneath tidal marshes on northwestern Vancouver Island, British Columbia. *Quaternary Research*, 48(2), 192–204. <https://doi.org/10.1006/qres.1997.1911>
- Blais-Stevens, A., & Patterson, R. T. (1998). Environmental indicator potential of Foraminifera from Saanich Inlet, Vancouver Island, British Columbia, Canada. *Cushman Foundation for Foraminiferal Research*, 28(2), 201–219.
- Bondevik, S., Svendsen, J. I., Johnsen, G., Mangerud, J., & Kaland, P. E. (1997). The Storegga tsunami along the Norwegian coast, its age and run up. *Boreas*, 26(1), 29–53. <https://doi.org/10.1111/j.1502-3885.1997.tb00649.x>
- Briggs, R. W., Engelhart, S. E., Nelson, A. R., Dura, T., Kemp, A. C., Haeussler, P. J., Corbett, D. R., Angster, S. J., & Bradley, L.-A. (2014). Uplift and subsidence reveal a nonpersistent megathrust rupture boundary (Sitkinak island, Alaska): COSEISMIC LAND-LEVEL CHANGE, SITKINAK. *Geophysical Research Letters*, 41(7), 2289–2296. <https://doi.org/10.1002/2014GL059380>
- British Columbia Ministry of Environment. (2016). *Air Quality in Port Alberni: A Summary of Trends and Patterns in Meteorology, and Common Air Pollutants* (pp. 1–71). British Columbia Ministry of Environment; June 20, 2024. <https://www2.gov.bc.ca/assets/gov/environment/air-land-water/air/reports-pub/port-alberni-aq-report.pdf>
- Cahill, N., Kemp, A. C., Horton, B. P., & Parnell, A. C. (2016). A Bayesian hierarchical model for reconstructing relative sea level: From raw data to rates of change. *Climate of the Past*, 12(2), 525–542. <https://doi.org/10.5194/cp-12-525-2016>
- Charman, D. J. (2001). Biostratigraphic and palaeoenvironmental applications of testate amoebae. *Quaternary Science Reviews*, 20(16–17), 1753–1764. [https://doi.org/10.1016/S0277-3791\(01\)00036-1](https://doi.org/10.1016/S0277-3791(01)00036-1)
- Chien, C.-W., Huang, C.-Y., Luo, S.-D., Jiang, S.-Y., Liu, C., & Yang, K.-M. (2018). Calcareous and agglutinated foraminifera ratio: Chemical interface tracer for Pliocene Chiahsien Paleoseep, SW Taiwan. *Terrestrial, Atmospheric and Oceanic Sciences*, 29(4), 417–428. <https://doi.org/doi:10.3319/TAO.2017.12.07.01>
- Chmura, G. L., & Aharon, P. (1995). Stable carbon isotope signatures of sedimentary carbon in coastal wetlands as indicators of salinity regime. *Journal of Coastal Research*, 11, 124–135.

- City of Port Alberni. (2016). Sewage Treatment Background Report. <https://portalberni.ca/liquid-waste-management-plan>
- Clague, J., Harper, J. R., Hebda, R. J., & Howes, D. E. (1982). Late Quaternary Sea levels and crustal movements, coastal British Columbia. *Canadian Journal of Earth Sciences*, 19(3), 597–618. <https://doi.org/10.1139/e82-048>
- Clague, J. J. (1997). Evidence for large earthquakes at the Cascadia subduction zone. *Reviews of Geophysics*, 35(4), 439–460. <https://doi.org/10.1029/97RG00222>
- Clague, J. J., & Bobrowsky, P. T. (1994a). Evidence for a large earthquake and tsunami 100–400 years ago on western Vancouver Island, British Columbia. *Quaternary Research*, 41(2), 176–184. <https://doi.org/10.1006/qres.1994.1019>
- Clague, J. J., & Bobrowsky, P. T. (1994b). Tsunami deposits beneath tidal marshes on Vancouver Island, British Columbia. *Geological Society of America Bulletin*, 106(10), 1293–1303. [https://doi.org/10.1130/0016-7606\(1994\)106<1293:TDBTMO>2.3.CO;2](https://doi.org/10.1130/0016-7606(1994)106<1293:TDBTMO>2.3.CO;2)
- Clague, J. J., Bobrowsky, P. T., & Hamilton, T. S. (1994). A sand sheet deposited by the 1964 Alaska tsunami at Port Alberni, British Columbia. *Estuarine, Coastal and Shelf Science*, 38(4), 413–421. <https://doi.org/10.1006/ecss.1994.1028>
- Clague, J. J., Bobrowsky, P. T., & Hutchinson, I. (2000). A review of geological records of large tsunamis at Vancouver Island, British Columbia, and implications for hazard. *Quaternary Science Reviews*, 19(9), 849–863. [https://doi.org/10.1016/S0277-3791\(99\)00101-8](https://doi.org/10.1016/S0277-3791(99)00101-8)
- Clague, J. J., Hutchinson, I., Matthews, R. W., & Patterson, R. T. (1999). Evidence for Late Holocene Tsunamis at Catala Lake, British Columbia. *Journal of Coastal Research*, 15, 45–60.
- Clark, K., Howarth, J., Litchfield, N., Cochran, U., Turnbull, J., Dowling, L., Howell, A., Berryman, K., & Wolfe, F. (2019). Geological evidence for past large earthquakes and tsunamis along the Hikurangi subduction margin, New Zealand. *Marine Geology*, 412, 139–172. <https://doi.org/10.1016/j.margeo.2019.03.004>
- Cochran, U., Berryman, K., Zachariassen, J., Mildenhall, D., Hayward, B., Southall, K., Hollis, C., Barker, P., Wallace, L., Alloway, B., & Wilson, K. (2006). Paleocological insights into subduction zone earthquake occurrence, eastern North Island, New Zealand. *Geological Society of America Bulletin*, 118(9–10), 1051–1074. <https://doi.org/10.1130/B25761.1>
- Cooper, S., Gaiser, E. E., & Wachnicka, A. (2010). Estuarine paleoenvironmental reconstructions using diatoms. In Smol, J.P. Stoermer, E.F. (Eds.), *The Diatoms: Applications for the Environmental and Earth Sciences* (pp. 324–345). Cambridge University Press.

- Dallimore, A., Enkin, R. J., Pienitz, R., Southon, J. R., Baker, J., Wright, C. A., Pedersen, T. F., Calvert, S. E., Ivanochko, T., & Thomson, R. E. (2008). Postglacial evolution of a Pacific coastal fjord in British Columbia, Canada: Interactions of sea-level change, crustal response, and environmental fluctuations — results from MONA core MD02-2494. This article is one of a series of papers published in this Special Issue on the theme Polar Climate Stability Network. *Canadian Journal of Earth Sciences*, 45(11), 1345–1362. <https://doi.org/10.1139/E08-042>
- Darrieno, M. E., & Peterson, C. D. (1990). Episodic tectonic subsidence of late Holocene salt marshes, northern Oregon central Cascadia margin. *Tectonics*, 9(1), 1–22. <https://doi.org/10.1029/TC009i001p00001>
- Darrieno, M. E. (1991). Late Holocene Paleoseismicity along the Northern Oregon Coast [Portland State University]. 10.15760/etd.1146
- Darrieno, M. E., Peterson, C. D., & Clough, C. (1994). Stratigraphic Evidence for Great Subduction-Zone Earthquakes at Four Estuaries in Northern Oregon, U.S.A. *Journal of Coastal Research*, 10(4), 850–876.
- Darrieno, M., & Peterson, C. (1995). Magnitude and Frequency of Subduction-Zone Earthquakes Along the Northern Oregon Coast IN the Past 3,000 Years. *Geology*, 57(1), 3–12.
- De Rijk, S. (1995). Salinity control on the distribution of salt marsh foraminifera (Great marshes, Massachusetts). *The Journal of Foraminiferal Research*, 25(2), 156–166. <https://doi.org/10.2113/gsjfr.25.2.156>
- DeLaune, R. D., Reddy, K. R., Richardson, C. J., & Megonigal, J. P. (Eds.). (2013). *Methods in biogeochemistry of wetlands (Vol. 2)*. Soil Science Society of America. Madison, Wisconsin, USA. 21-40. DOI:10.2136/sssabookser10
- DeMets, C., Gordon, R. G., & Argus, D. F. (2010). Geologically current plate motions. *Geophysical Journal International*, 181(1), 1–80. <https://doi.org/10.1111/j.1365-246X.2009.04491.x>
- Douglas, B. C. (1991). Global sea level rise. *Journal of Geophysical Research: Oceans*, 96(C4), 6981–6992. <https://doi.org/10.1029/91JC00064>
- Douglas, T. J., Schuerholz, G., & Juniper, S. K. (2022). Blue Carbon Storage in a Northern Temperate Estuary Subject to Habitat Loss and Chronic Habitat Disturbance: Cowichan Estuary, British Columbia, Canada. *Frontiers in Marine Science*, 9. <https://doi.org/https://doi.org/10.3389/fmars.2022.857586>
- Dura, T., Engelhart, S. E., Vacchi, M., Horton, B. P., Kopp, R. E., Peltier, W. R., & Bradley, S. (2016). The Role of Holocene Relative Sea-Level Change in Preserving Records of Subduction Zone Earthquakes. *Current Climate Change Reports*, 2(3), 86–100. <https://doi.org/10.1007/s40641-016-0041-y>

- Edwards, R. J., Wright, A. J., & Van De Plassche, O. (2004). Surface distributions of salt-marsh foraminifera from Connecticut, USA: Modern analogues for high-resolution sea level studies. *Marine Micropaleontology*, 51(1–2), 1–21. <https://doi.org/10.1016/j.marmicro.2003.08.002>
- Edwards, R., & Wright, A. J. (2015). Foraminifera, in: *In Handbook of Sea-Level Research*, edited by: Shannon, I., Long, A. J. , and Horton, B. P. , (John Wiley & Sons).
- Engelhart, S. E., Horton, B. P., Nelson, A. R., Hawkes, A. D., Witter, R. C., Wang, K., Wang, P.-L., & Vane, C. H. (2013). Testing the use of microfossils to reconstruct great earthquakes at Cascadia. *Geology*, 41(10), 1067–1070. <https://doi.org/10.1130/G34544.1>
- Engelhart, S. E., Horton, B. P., Vane, C. H., Nelson, A. R., Witter, R. C., Brody, S. R., & Hawkes, A. D. (2013). Modern foraminifera, $\delta^{13}\text{C}$, and bulk geochemistry of central Oregon tidal marshes and their application in paleoseismology. *Palaeogeography, Palaeoclimatology, Palaeoecology*, 377, 13–27. <https://doi.org/10.1016/j.palaeo.2013.02.032>
- Engelhart, S. E., Vacchi, M., Horton, B. P., Nelson, A. R., & Kopp, R. E. (2015). A sea-level database for the Pacific coast of central North America. *Quaternary Science Reviews*, 113, 78–92. <https://doi.org/10.1016/j.quascirev.2014.12.001>
- Environment Canada. (2023). Canadian Climate Normals. Online: https://climate.weather.gc.ca/climate_normals/index_e.html
- Fisheries and Oceans Canada (DFO). (2023). Station Inventory Data; Government of Canada. <https://www.isdm-gdsi.gc.ca/isdm-gdsi/twl-mne/inventory-inventaire/sd-ds-eng.asp?no=8575&user=isdm-gdsi®ion=PAC>
- Friele, P. A., & Hutchinson, I. (1993). Holocene sea-level change on the central west coast of Vancouver Island, British Columbia. *Canadian Journal of Earth Sciences*, 30(4), 832–840. <https://doi.org/10.1139/e93-069>
- Garrett, E., Brain, M. J., Hayward, B. W., Newnham, R., Morey, C. J., & Gehrels, W. R. (2023). Resolving uncertainties in foraminifera-based relative sea-level reconstruction: A case study from southern New Zealand. *Journal of Foraminiferal Research*, 53(1), 78–89. <https://doi.org/10.2113/gsjfr.53.1.78>
- Garrison-Laney, C. (2017). Tsunamis and sea levels of the past millennium in Puget Sound, Washington [Unpublished PhD thesis]. University of Washington, USA.
- Garrison-Laney, C., & Miller, I. M. (2017). Tsunamis in the Salish Sea: Recurrence, sources, hazards. 49, 67–78. [https://doi.org/10.1130/2017.0049\(04\)](https://doi.org/10.1130/2017.0049(04))
- Gehrels, W. R. (1994). Determining relative sea-level change from salt-marsh foraminifera and plant zones on the coast of Maine, U.S.A. *Journal of Coastal Research*, 10, 990–1009.

- Gehrels, W. R., Roe, H. M., & Charman, D. J. (2001). Foraminifera, testate amoebae, and diatoms as sea-level indicators in UK saltmarshes: A quantitative multiproxy approach. *Journal of Quaternary Science*, 16(3), 201–220. <https://doi.org/10.1002/jqs.588>
- Goff, J., Bobrowsky, P., Huntley, D., Sawai, Y., & Tanagawa, K. (2020). Palaeotsunamis along Canada's Pacific coast. *Quaternary Science Reviews*, 237, 106309. <https://doi.org/10.1016/j.quascirev.2020.106309>
- Goff, J., Chagué-Goff, C., Nichol, S., Jaffe, B., & Dominey-Howes, D. (2012). Progress in palaeotsunami research. *Sedimentary Geology*, 243–244, 70–88. <https://doi.org/10.1016/j.sedgeo.2011.11.002>
- Goldfinger, C., Nelson, C. H., Morey, A. E., Johnson, J. E., Patton, J. R., Karabanov, E. B., Gutierrez-Pastor, J., Eriksson, A. T., Gracia, E., Dunhill, G., Enkin, R. J., Dallimore, A., & Vallier, T. (2012). Turbidite event history—Methods and implications for Holocene paleoseismicity of the Cascadia subduction zone. Dept. of the Interior, U.S. Geological Survey.
- Graehl, N. A., Kelsey, H. M., Witter, R. C., Hemphill-Haley, E., & Engelhart, S. E. (2015). Stratigraphic and microfossil evidence for a 4500-year history of Cascadia subduction zone earthquakes and tsunamis at Yaquina River estuary, Oregon, USA. *GSA Bulletin*, 127(1/2), 211–226. <https://doi.org/10.1130/B31074.1>
- Guilbault, J.-P., Clague, J. J., & Lapointe, M. (1995). Amount of subsidence during a late Holocene earthquake—Evidence from fossil tidal marsh foraminifera at Vancouver Island, west coast of Canada. *Palaeogeography, Palaeoclimatology, Palaeoecology*, 118(1–2), 49–71. [https://doi.org/10.1016/0031-0182\(94\)00135-U](https://doi.org/10.1016/0031-0182(94)00135-U)
- Guilbault, J.-P., Clague, J. J., & Lapointe, M. (1996). Foraminiferal evidence for the amount of coseismic subsidence during a late Holocene earthquake on Vancouver Island, West Coast of Canada. *Quaternary Science Reviews*, 15(8–9), 913–937. [https://doi.org/10.1016/S0277-3791\(96\)00058-3](https://doi.org/10.1016/S0277-3791(96)00058-3)
- Hamilton, S., & Shennan, I. (2005). Late Holocene relative sea-level changes and the earthquake deformation cycle around upper Cook Inlet, Alaska. *Quaternary Science Reviews*, 24(12–13), 1479–1498. <https://doi.org/10.1016/j.quascirev.2004.11.003>
- Hawkes, A. D., Horton, B. P., Nelson, A. R., & Hill, D. F. (2010). The application of intertidal foraminifera to reconstruct coastal subsidence during the giant Cascadia earthquake of AD 1700 in Oregon, USA. *Quaternary International*, 221(1–2), 116–140. <https://doi.org/10.1016/j.quaint.2009.09.019>
- Hawkes, A. D., Horton, B. P., Nelson, A. R., Vane, C. H., & Sawai, Y. (2011). Coastal subsidence in Oregon, USA, during the giant Cascadia earthquake of AD 1700. *Quaternary Science Reviews*, 30(3–4), 364–376. <https://doi.org/10.1016/j.quascirev.2010.11.017>

- Hawkes, A. D., Scott, D. B., Lipps, J. H., & Combellick, R. (2005). Evidence for possible precursor events of megathrust earthquakes on the west coast of North America. *Geological Society of America Bulletin*, 117(7), 996. <https://doi.org/10.1130/B25455.1>
- He, X., Montillet, J.-P., Fernandes, R., Melbourne, T. I., Jiang, W., & Huang, Z. (2022). Sea level rise estimation on the pacific coast from southern California to Vancouver Island. *Remote Sensing*, 14(17), 4339. <https://doi.org/10.3390/rs14174339>
- Heathfield, D. K., Walker, I. J., & Atkinson, D. E. (2013). Erosive water level regime and climatic variability forcing of beach–dune systems on south-western Vancouver Island, British Columbia, Canada. *Earth Surface Processes and Landforms*, 38(7), 751–762. <https://doi.org/10.1002/esp.3350>
- Hemphill-Haley, E. (1995). Diatom evidence for earthquake-induced subsidence and tsunami 300 yr ago in southern coastal Washington. *GSA Bulletin*, 107(3), 367–378.
- Hill, M. O., & Gauch, H. G. (1980). Detrended correspondence analysis: An improved ordination technique. *Vegetation*, 42(1–3), 47–58. <https://doi.org/10.1007/BF00048870>
- Hong, I., Horton, B. P., Hawkes, A. D., O'Donnell, R. J., Padgett, J. S., Dura, T., & Engelhart, S. E. (2021). Diatoms of the intertidal environments of Willapa Bay, Washington, USA as a sea-level indicator. *Marine Micropaleontology*, 167, 102033. <https://doi.org/10.1016/j.marmicro.2021.102033>
- Horton, B. P., & Edwards, R. J. (2003). Seasonal distributions of foraminifera and their implications for sea-level studies, Cowpen Marsh, UK. *Micropaleontological Proxies for Sea-Level Change and Stratigraphic Discontinuities*, 75, 21–30.
- Horton, B. P., & Edwards, R. J. (2005). The application of local and regional transfer functions to the reconstruction of Holocene sea levels, north Norfolk, England. *The Holocene*, 15(2), 216–228. <https://doi.org/10.1191/0959683605hl787rp>
- Horton, B. P., & Edwards, R. J. (2006). Quantifying Holocene sea-level change using intertidal foraminifera: Lessons from the British Isles. *Anuário Do Instituto de Geociências*, 29(1), 541–542. https://doi.org/10.11137/2006_1_541-542
- Horton, B. P., Edwards, R. J., & Lloyd, J. M. (1999). A foraminiferal-based transfer function: Implications for sea-level studies. *Journal of Foraminiferal Research*, 29(2), 117–129.
- Hu, Y., Wang, K., He, J., Klotz, J., & Khazaradze, G. (2004). Three-dimensional viscoelastic finite element model for postseismic deformation of the great 1960 Chile earthquake. *Journal of Geophysical Research*, 109 (B12). <https://doi.org/https://doi.org/10.1029/2004JB003163>
- Hughes, J. F., & Mathewes, R. W. (2003). A modern analogue for plant colonization of palaeotsunami sands in Cascadia, British Columbia, Canada. *The Holocene*, 13(6), 877–886. <https://doi.org/10.1191/0959683603hl670rp>

- Huntley, D. J., & Clague, J. J. (1996). Optical dating of tsunami-laid sands. *Quaternary Research*, 46(2), 127–140. <https://doi.org/10.1006/qres.1996.0053>
- Hutchinson, I., & Clague, J. (2017). Were they all giants? Perspectives on late Holocene plate-boundary earthquakes at the northern end of the Cascadia subduction zone. *Quaternary Science Reviews*, 169, 29–49. <https://doi.org/10.1016/j.quascirev.2017.05.015>
- Imbrie, J., & Kipp, N. G. (1971). A new micro paleontological method for quantitative paleoclimatology: Application to a late Pleistocene Caribbean core. In *The Late Cenozoic Glacial Ages* (Ed K.K. Turekian), 77–81. Yale University Press, New Haven.
- Ishizawa, T., Goto, K., Yokoyama, Y., & Miyairi, Y. (2019). Non-destructive analyses to determine appropriate stratigraphic level for dating of tsunami deposits. *Marine Geology*, 412, 19–26. <https://doi.org/10.1016/j.margeo.2019.02.009>
- Jaffe, B. E., & Gelfenbaum, G. (2007). A simple model for calculating tsunami flow speed from tsunami deposits. *Sedimentary Geology*, 200(3–4), 347–361. <https://doi.org/10.1016/j.sedgeo.2007.01.013>
- Jawanda, B. S. (1954). A geographical study of Vancouver Island [University of British Columbia]. Retrieved from: <https://open.library.ubc.ca/collections/ubctheses/831/items/1.0106645>
- Jennings, A. E., & Nelson, A. R. (1992). Foraminiferal assemblage zones in Oregon tidal marshes; relation to marsh floral zones and sea level. *The Journal of Foraminiferal Research*, 22(1), 13–29. <https://doi.org/10.2113/gsjfr.22.1.13>
- Jonasson, K. E., & Patterson, R. T. (1992). Preservation potential of salt marsh foraminifera from the Fraser River delta, British Columbia. *Micropaleontology*, 38(3), 289. <https://doi.org/10.2307/1485793>
- Jones, G. D., & Ross, C. A. (1979). Seasonal Distribution of Foraminifera in Samish Bay, Washington. *Journal of Paleontology*, 53(2), 245–257.
- Kanamori, H. (1977). The energy release in great earthquakes. *Journal of Geophysical Research*, 82(20), 2981–2987. <https://doi.org/10.1029/JB082i020p02981>
- Kassambara, A., & Mundt, F. (2016). Package ‘factoextra’. Extract and visualize the results of multivariable data analysis. [Computer software].
- Kaufman, L., & Rousseeuw, P. J. (2005). Finding groups in data: An introduction to cluster analysis. Wiley.
- Kelsey, H. M., Witter, R. C., & Hemphill-Haley, E. (2002). Plate-boundary earthquakes and tsunamis of the past 5500 yr, Sixes River estuary, southern Oregon. *Geological Society of America Bulletin*, 114(3), 298–314. [https://doi.org/10.1130/0016-7606\(2002\)114<0298:PBEATO>2.0.CO;2](https://doi.org/10.1130/0016-7606(2002)114<0298:PBEATO>2.0.CO;2)

- Kemp, A. C., Cahill, N., Engelhart, S. E., Hawkes, A. D., & Wang, K. (2018). Revising estimates of spatially variable subsidence during the a. D. 1700 Cascadia earthquake using a Bayesian foraminiferal transfer function. *Bulletin of the Seismological Society of America*, 108(2), 654–673. <https://doi.org/10.1785/0120170269>
- Kemp, A. C., Horton, B. P., Corbett, D. R., Culver, S. J., Edwards, R. J., & Van De Plassche, O. (2009). The relative utility of foraminifera and diatoms for reconstructing late Holocene sea-level change in North Carolina, USA. *Quaternary Research*, 71(1), 9–21. <https://doi.org/10.1016/j.yqres.2008.08.007>
- Kemp, A. C., Horton, B. P., Vann, D. R., Engelhart, S. E., Grand Pre, C. A., Vane, C. H., Nikitina, D., & Anisfeld, S. C. (2012). Quantitative vertical zonation of salt-marsh foraminifera for reconstructing former sea level; an example from New Jersey, USA. *Quaternary Science Reviews*, 54, 26–39. <https://doi.org/10.1016/j.quascirev.2011.09.014>
- Kemp, A. C., Telford, R. J., Horton, B. P., Anisfeld, S. C., & Sommerfield, C. K. (2013). Reconstructing Holocene Sea level using salt-marsh foraminifera and transfer functions: Lessons from New Jersey, USA. *Journal of Quaternary Science*, 28(6), 617–629. <https://doi.org/10.1002/jqs.2657>
- Kemp, A. C., Vane, C. H., Horton, B. P., Engelhart, S. E., & Nikitina, D. (2012). Application of stable carbon isotopes for reconstructing salt-marsh floral zones and relative sea level, New Jersey, USA: STABLE CARBON ISOTOPES IN SALT MARSH FLORAL ZONES. *Journal of Quaternary Science*, 27(4), 404–414. <https://doi.org/10.1002/jqs.1561>
- Kemp, A. C., Wright, A. J., & Cahill, N. (2020). Enough is enough, or more is more? Testing the influence of foraminiferal count size on reconstructions of paleo-marsh elevation. *Journal of Foraminiferal Research*, 50(3), 266–278. <https://doi.org/10.2113/gsjfr.50.3.266>
- Lamb, A. L., Wilson, G. P., & Leng, M. J. (2006). A review of coastal palaeoclimate and relative sea-level reconstructions using $\delta^{13}\text{C}$ and C/N ratios in organic material. *Earth-Science Reviews*, 75(1–4), 29–57. <https://doi.org/10.1016/j.earscirev.2005.10.003>
- Leonard, L. J., Currie, C. A., Mazzotti, S., & Hyndman, R. D. (2010). Rupture area and displacement of past Cascadia great earthquakes from coastal coseismic subsidence. *Geological Society of America Bulletin*, 122(11–12), 2079–2096. <https://doi.org/10.1130/B30108.1>
- Leonard, L. J., Hyndman, R. D., & Mazzotti, S. (2004). Coseismic subsidence in the 1700 great Cascadia earthquake: Coastal estimates versus elastic dislocation models. *Geological Society of America Bulletin*, 116(5), 655. <https://doi.org/10.1130/B25369.1>
- Letham, B., Fedje, D., Hebda, C. F. G., Dyck, A., Stafford, J., Hutchinson, I., Southon, J., Fedje, B., & McLaren, D. (2024). Postglacial relative sea level histories of northern Vancouver Island, Canada. *Quaternary Science Reviews*, 326, 108415. <https://doi.org/10.1016/j.quascirev.2023.108415>

- Lloyd, J. M., & Evans, J. R. (2002). Contemporary and fossil foraminifera from isolation basins in northwest Scotland. *Journal of Quaternary Science*, 17(5–6), 431–443. <https://doi.org/10.1002/jqs.719>
- Long, A. J., Woodroffe, S. A., Milne, G. A., Bryant, C. L., Simpson, M. J. R., & Wake, L. M. (2012). Relative sea-level change in Greenland during the last 700 yrs. and ice sheet response to the Little Ice Age. *Earth and Planetary Science Letters*, 315–316, 76–85. <https://doi.org/10.1016/j.epsl.2011.06.027>
- Ludwin, R. S., Dennis, R., Carver, D., McMillan, A. D., Losey, R., Clague, J., Jonientz-Trisler, C., Bovechop, J., Wray, J., & James, K. (2005). Dating the 1700 Cascadia earthquake: Great coastal earthquakes in native stories. *Seismological Research Letters*, 76(2), 140–148. <https://doi.org/10.1785/gssrl.76.2.140>
- Luo, H., & Wang, K. (2022). Finding simplicity in the complexity of postseismic coastal uplift and subsidence following great subduction earthquakes. *Journal of Geophysical Research: Solid Earth*, 127(10). <https://doi.org/10.1029/2022JB024471>
- Maechler, M., Rousseeuw, P. J., Struyf, A., & Hubert, M. (2012). *Cluster: Cluster Analysis Basics and Extensions*, R Package. [Computer software].
- Masson-Delmotte, V., Zhai, P., Pirani, A., Connors, S.L., Péan, C., Berger, C., Caud, N., Chen, Y., Goldfarb, L., Gomis, M.L., Huang, M., Leitzell, K., Lonnoy, E., Matthews, J.B.R., Maycock, T.K., Waterfield, T., Yu, O., Yelekçi, R., and Zhou, B. (2021) ‘Summary for Policymakers. In: *Climate Change 2021: The Physical Science Basis. Contribution of Working Group I to the Sixth Assessment Report of the Intergovernmental Panel on Climate Change*’, Cambridge University Press.
- McLaren, D., Fedje, D., Hay, M. B., Mackie, Q., Walker, I. J., Shugar, D. H., Eamer, J. B. R., Lian, O. B., & Neudorf, C. (2014). A post-glacial sea level hinge on the central Pacific coast of Canada. *Quaternary Science Reviews*, 97, 148–169. <https://doi.org/10.1016/j.quascirev.2014.05.023>
- McMillan, A. D., & Hutchinson, I. (2002). When the mountain dwarfs danced: Aboriginal traditions of paleoseismic events along the Cascadia subduction zone of western North America. *Ethnohistory*, 49(1), 41–68. <https://doi.org/10.1215/00141801-49-1-41>
- Melnick, D., Moreno, M., Motagh, M., Cisternas, M., & Wesson, R. L. (2012). Splay fault slip during the Mw 8.8 2010 Maule Chile earthquake. *Geology*, 40(3), 251–254. <https://doi.org/https://doi.org/10.1130/G32712.1>
- Milker, Y., Horton, B. P., Nelson, A. R., Engelhart, S. E., & Witter, R. C. (2015). Variability of intertidal foraminiferal assemblages in a salt marsh, Oregon, USA. *Marine Micropaleontology*, 118, 1–16. <https://doi.org/10.1016/j.marmicro.2015.04.004>
- Milker, Y., Horton, B. P., Vane, C. H., Engelhart, S. E., Nelson, A. R., Witter, R. C., Khan, N. S., & Bridgeland, W. T. (2015). Annual and seasonal distribution of intertidal foraminifera and stable carbon isotope geochemistry, Bandon Marsh, Oregon, USA. *The Journal of Foraminiferal Research*, 45(2), 146–155. <https://doi.org/10.2113/gsjfr.45.2.146>

- Milker, Y., Nelson, A. R., Horton, B. P., Engelhart, S. E., Bradley, L.-A., & Witter, R. C. (2016). Differences in coastal subsidence in southern Oregon (USA) during at least six prehistoric megathrust earthquakes. *Quaternary Science Reviews*, 142, 143–163. <https://doi.org/10.1016/j.quascirev.2016.04.017>
- Mori, N., Takahashi, T., Yasuda, T., & Yanagisawa, H. (2011). Survey of 2011 Tohoku earthquake tsunami inundation and run-up: SURVEY OF 2011 TOHOKU EARTHQUAKE TSUNAMI. *Geophysical Research Letters*, 38(7), n/a-n/a. <https://doi.org/10.1029/2011GL049210>
- Morris, S., & Leaney, Adelle. J. (1980). The Somas River estuary: Status of environmental knowledge to 1980: Canada Department of Fisheries and Oceans and Canada Department of Environment, Pacific, and Yukon Region, Special Estuary Series. 374.
- Murray, J. W. (1991). *Ecology and palaeoecology of benthic foraminifera*. Longman Scientific and Technical; Wiley.
- Murray, J. W., & Alve, E. (1999). Natural dissolution of modern shallow water benthic foraminifera: Taphonomic effects on the palaeoecological record. *Palaeogeography, Palaeoclimatology, Palaeoecology*, 146(1–4), 195–209. [https://doi.org/10.1016/S0031-0182\(98\)00132-1](https://doi.org/10.1016/S0031-0182(98)00132-1)
- Natawidjaja, D. H., Sieh, K., Galetzka, J., Suwargadi, B. W., Cheng, H., Edwards, R. L., & Chlieh, M. (2007). Interseismic deformation above the Sunda Megathrust recorded in coral microatolls of the Mentawai islands, West Sumatra. *Journal of Geophysical Research: Solid Earth*, 112(B2), 2006JB004450. <https://doi.org/10.1029/2006JB004450>
- Nelson, A., Hawkes, A. D., Sawai, Y., Engelhart, S., Witter, R., Grant-Walter, W. C., Bradley, L.-A., Dura, T., Cahill, N., & Horton, B. (2020). Identifying the Greatest Earthquakes of the Past 2000 Years at the Nehalem River Estuary, Northern Oregon Coast, USA. *Open Quaternary*, 6(2), 1–30. [https://doi.org/DOI: https://doi.org/10.5334/oq.70](https://doi.org/DOI:https://doi.org/10.5334/oq.70)
- Nelson, A. R., Sawai, Y., Jennings, A. E., Bradley, L. A., Gerson, L., Sherrod, B. L., Sabeau, J., & Horton, B. P. (2008). Great-earthquake paleogeodesy and tsunamis of the past 2000 years at Alsea Bay, central Oregon coast, USA. *Quaternary Science Reviews*, 27, 747–768.
- Nelson, A. R., Shennan, I., & Long, A. J. (1996). Identifying coseismic subsidence in tidal-wetland stratigraphic sequences at the Cascadia subduction zone of western North America. *Journal of Geophysical Research: Solid Earth*, 101(B3), 6115–6135. <https://doi.org/10.1029/95JB01051>
- NOAA Tides & Currents. (2023). https://tidesandcurrents.noaa.gov/datum_options.html
- Oksanen, J., Kindt, R., Legendre, P., O'Hara, B., Stevens, M., & Oksanen, M. (2007). The vegan package. Community ecology package [Computer software]. <https://cran.ism.ac.jp/web/packages/vegan/vegan.pdf>

- Padgett, J. S., Engelhart, S. E., Kelsey, H. M., Witter, R. C., Cahill, N., & Hemphill-Haley, E. (2021). Timing and amount of southern Cascadia earthquake subsidence over the past 1700 years at northern Humboldt Bay, California, USA. *GSA Bulletin*, 133(9–10), 2137–2156. <https://doi.org/10.1130/B35701.1>
- Palmer, A. J., & Abbott, W. H. (1986). *Diatoms as Indicators of Sea-Level Change*. Springer, Sea-Level Research, 457–487.
- Parish, R., & Thomson, S. M. (1994). *Tree book: Learning to recognize trees of British Columbia*. Canadian Forest Service.
- Patterson, R. T., Dalby, A. P., Roe, H. M., Guilbault, J.-P., Hutchinson, I., & Clague, J. J. (2005). Relative utility of foraminifera, diatoms and macrophytes as high-resolution indicators of paleo-sea level in coastal British Columbia, Canada. *Quaternary Science Reviews*, 24(18–19), 2002–2014. <https://doi.org/10.1016/j.quascirev.2004.11.013>
- Patterson, R. T., Guilbault, J.-P., & Clague, J. J. (1999). Taphonomy of tidal marsh foraminifera: Implications of surface sample thickness for high-resolution sea-level studies. *Palaeogeography, Palaeoclimatology, Palaeoecology*, 149(1–4), 199–211. [https://doi.org/10.1016/S0031-0182\(98\)00201-6](https://doi.org/10.1016/S0031-0182(98)00201-6)
- Patterson, R. T., & Kumar, A. (2002). A review of current testate rhizopod (Thecamoebian) research in Canada. *Palaeogeography, Palaeoclimatology, Palaeoecology*, 180(1–3), 225–251. [https://doi.org/10.1016/S0031-0182\(01\)00430-8](https://doi.org/10.1016/S0031-0182(01)00430-8)
- Peters, R., Jaffe, B., & Gelfenbaum, G. (2007). Distribution and sedimentary characteristics of tsunami deposits along the Cascadia margin of western North America. *Sedimentary Geology*, 200(3–4), 372–386. <https://doi.org/10.1016/j.sedgeo.2007.01.015>
- Peters, R., Jaffe, B., & Peterson, C. (2003). *Cascadia Tsunami Deposit Database (2003–13; Open-File Report)*. 10.3133/ofr0313
- Peterson, C. D., Clague, J. J., Carver, G. A., & Cruikshank, K. M. (2013). Recurrence intervals of major paleotsunamis as calibrated by historic tsunami deposits in three localities: Port Alberni, Cannon Beach, and Crescent City, along the Cascadia margin, Canada and USA. *Natural Hazards*, 68, 321–336. <https://doi.org/10.1007/s11069-013-0622-1>
- Peterson, M. D., Moschetti, M. P., Powers, P. M., Mueller, C. S., Haller, K. M., & et al. (2014). *Documentation for the 2014 update of the United States National Seismic Hazard Maps*. (Open File Rep. 2014-1091).
- Pilarczyk, J. E., Horton, B. P., Witter, R. C., Vane, C. H., Chagué-Goff, C., & Goff, J. (2012). Sedimentary and foraminiferal evidence of the 2011 Tōhoku-oki tsunami on the Sendai coastal plain, Japan. *Sedimentary Geology*, 282, 78–89. <https://doi.org/https://doi.org/10.1016/j.sedgeo.2012.08.011>

- Pilarczyk, J. E., Sawai, Y., Namegaya, Y., Tamura, T., Tanigawa, K., Matsumoto, D., Shinozaki, T., Fujiwara, O., Shishikura, M., Shimada, Y., Dura, T., Horton, B. P., Parnell, A. C., & Vane, C. H. (2021). A further source of Tokyo earthquakes and Pacific Ocean tsunamis. *Nature Geoscience*, 14(10), 796–800. <https://doi.org/10.1038/s41561-021-00812-2>
- Pilarczyk, J., Sawai, Y., Matsumoto, D., Namegaya, Y., Nishida, N., Ikehara, K., Fujiwara, O., Gouramanis, C., Dura, T., & Horton, B. P. (2020). Constraining sediment provenance for tsunami deposits using distributions of grain size and foraminifera from the Kujukuri coastline and shelf, Japan. *Sedimentology*, 67(3), 1373–1392. <https://doi.org/https://doi.org/10.1111/sed.12591>
- Plassche, O. van de. (1986). *Sea-level research: A manual for the collection and evaluation of data*. Geo Books.
- Pojar, J., & Alaback, P. B. (Eds.). (1994). *Plants of the Pacific Northwest Coast: Washington, Oregon, British Columbia & Alaska* (1. print). Lone Pine Publ.
- Reimer, P. J., Austin, W. E. N., Bard, E., Bayliss, A., Blackwell, P. G., Bronk Ramsey, C., Butzin, M., Cheng, H., Edwards, R. L., Friedrich, M., Grootes, P. M., Guilderson, T. P., Hajdas, I., Heaton, T. J., Hogg, A. G., Hughen, K. A., Kromer, B., Manning, S. W., Muscheler, R., ... Talamo, S. (2020). The IntCal20 Northern Hemisphere radiocarbon age calibration curve (0–55 cal. kBP). *Radiocarbon*, 62(4), 725–757. <https://doi.org/10.1017/RDC.2020.41>
- Riou, L., Nasser, N. A., Patterson, R. T., Gregory, B. R. B., Galloway, J. M., & Falck, H. (2021). Lacustrine arcellinida (Testate lobose amoebae) as bioindicators of arsenic concentration within the Yellowknife city gold project, Northwest Territories, Canada. *Limnologia*, 87, 125862. <https://doi.org/10.1016/j.limno.2021.125862>
- Röbke, B. R., & Vött, A. (2017). The tsunami phenomenon. *Progress in Oceanography*, 159, 296–322. <https://doi.org/10.1016/j.pocan.2017.09.003>
- Roe, H. M., Doherty, C. T., Patterson, R. T., & Milne, G. A. (2013). Isolation basin records of late Quaternary sea-level change, central mainland British Columbia, Canada. *Quaternary International*, 310, 181–198. <https://doi.org/10.1016/j.quaint.2013.01.026>
- Roe, H. M., Doherty, C. T., Patterson, R. T., & Swindles, G. T. (2009). Contemporary distributions of saltmarsh diatoms in the Seymour–Belize Inlet complex, British Columbia, Canada: Implications for studies of sea-level change. *Marine Micropaleontology*, 70(3–4), 134–150. <https://doi.org/10.1016/j.marmicro.2008.12.001>
- Sabeau, J. (2004). *Applications of foraminifera to detecting land level change associated with great earthquakes along the west coast of North America* [M.Sc. Thesis]. Department of Earth Sciences, Simon Fraser University.
- Satake, K., & Atwater, B. F. (2007). Long-term perspectives on giant earthquakes and tsunamis at subduction zones. *Annual Review of Earth and Planetary Sciences*, 35(1), 349–374. <https://doi.org/10.1146/annurev.earth.35.031306.140302>

- Sawai, Y. (2020). Subduction zone paleoseismology along the Pacific coast of northeast Japan—Progress and remaining problems. *Earth-Science Reviews*, 208, 103261.
<https://doi.org/10.1016/j.earscirev.2020.103261>
- Sawai, Y., Satake, K., Kamataki, T., Nasu, H., Shishikura, M., Atwater, B. F., Horton, B. P., Kelsey, H. M., Nagumo, T., & Yamaguchi, M. (2004). Transient uplift after a 17th-century earthquake along the Kuril subduction zone. *Science*, 306(5703), 1918–1920.
<https://doi.org/10.1126/science.1104895>
- Scott, D. B., Collins, E. S., Duggan, J., Asioli, A., Saito, T., & Hasegawa, S. (1996). Pacific Rim Marsh Foraminiferal Distributions: Implications for Sea-Level Studies. *Journal of Coastal Research*, 12(4), 850–861.
- Scott, D. B., & Hermelin, J. O. R. (1993). A device for precision splitting of micropaleontological samples in liquid suspension. *Journal of Paleontology*, 67(1), 151–154.
<https://doi.org/10.1017/S0022336000021302>
- Scott, D. B., & Medioli, F. S. (1980). Quantitative studies of marsh foraminiferal distributions in Nova Scotia: Implications for sea level studies. *Cushman Found. Foram. Res. Spec.*, 17(58).
- Scott, D. B., & Medioli, F. S. (1986). Foraminifera as sea- level indicators. *A Manual for the Collection and Evaluation of Data*, 435–456.
- Scott, D. B., Medioli, F. S., & Schafer, C. T. (2001). *Monitoring in coastal environments using Foraminifera and Thecamoebian indicators*. Cambridge University Press.
- Scott, D. B., Schafer, C. T., & Medioli, F. S. (1980). Eastern Canadian estuarine foraminifera; a framework for comparison. *The Journal of Foraminiferal Research*, 10(3), 205–234.
<https://doi.org/10.2113/gsjfr.10.3.205>
- Scott, D. B., Williamson, M. A., & Duffett, T. E. (1981). Marsh foraminifera of Prince Edward Island: Their recent distribution and application for former sea level studies. *Atlantic Geology*, 17(3). <https://doi.org/10.4138/1380>
- Scott, D. S., & Medioli, F. S. (1978). Vertical zonations of marsh foraminifera as accurate indicators of former sea-levels. *Nature*, 272(5653), 528–531.
<https://doi.org/10.1038/272528a0>
- Shennan, I., Long, A., & Horton, B. P. (2015). *Handbook of sea-level research* (1st ed.). Wiley-Blackwell.
- Shennan, I., Long, A. J., Rutherford, M. M., Green, F. M., Innes, J. B., Lloyd, J. M., Zong, Y., & Walker, K. J. (1996). Tidal marsh stratigraphy, sea-level change, and large earthquakes, i: A 5000-year record in Washington, U.S.A. *Quaternary Science Reviews*, 15(10), 1023–1059. [https://doi.org/10.1016/S0277-3791\(96\)00007-8](https://doi.org/10.1016/S0277-3791(96)00007-8)
- Shroder, J., & Shroder, J. F. (2013). *Treatise on Geomorphology*.

- Shugar, D. H., Walker, I. J., Lian, O. B., Eamer, J. B. R., Neudorf, C., McLaren, D., & Fedje, D. (2014). Post-glacial sea-level change along the Pacific coast of North America. *Quaternary Science Reviews*, 97, 170–192. <https://doi.org/10.1016/j.quascirev.2014.05.022>
- Southall, K. E., Gehrels, W. R., & Hayward, B. W. (2006). Foraminifera in a New Zealand salt marsh and their suitability as sea-level indicators. *Marine Micropaleontology*, 60(2), 167–179. <https://doi.org/10.1016/j.marmicro.2006.04.005>
- Spiske, M., Piepenbreier, J., Benavente, C., & Bahlburg, H. (2013). Preservation potential of tsunami deposits on arid siliciclastic coasts. *Earth-Science Reviews*, 126, 58–73. <https://doi.org/10.1016/j.earscirev.2013.07.009>
- Staisch, L.M., Witter, R.C., Watt, J.T., Grant, A.R., Walton, M.A., Brothers, D., Davis, E., Dura, C., Engelhart, S., Enkin, R., Garrison-Laney, C.E, Goldfinger, C., Hamilton, T., Hawkes, A., Hill, J.C., Hong, I.J., Jaffe, B.E., Kelsey, H., Lahusen, S.R, La Selle, S.M, Nelson, A.R, Nieminski, N.M, Padgett, J.S, Patton, J., Pearl, J.K, Pilarczyk, J., Sherrod, B., and Stanton, K., 2024, Compiled onshore and offshore paleoseismic data along the Cascadia Subduction Zone: U.S. Geological Survey data release, <https://doi.org/10.5066/P13OJQYW>.
- Station Inventory Data. (2022). Fisheries and Oceans Canada. charts.gc.ca
- Statistics Canada. (2023). Census Profile, 2021 Census of Population. Statistics Canada Catalogue No. 98-316-X2021001. <https://www12.statcan.gc.ca/census-recensement/2021/dp-pd/prof/index.cfm?Lang=E>
- Tanigawa, K., Sawai, Y., Bobrowsky, P., Huntley, D., Goff, J., Shinozaki, T., & Ito, K. (2022). A new chronology for tsunami deposits prior to the 1700 CE Cascadia earthquake from Vancouver Island, Canada. *Scientific Reports*, 12(1), 12527. <https://doi.org/10.1038/s41598-022-16842-8>
- Tanigawa, K., Sawai, Y., Bobrowsky, P., Huntley, D. H., Goff, J., & Shinozaki, T. (2017). Geological evidence for tsunamis prior to the 1700 Cascadia earthquake from Vancouver Island, Canada. 302545. <https://doi.org/10.1130/abs/2017AM-302545>
- Thrush, C., & Ludwin, R. S. (2007). Finding fault: Indigenous seismology, colonial science, and the rediscovery of earthquakes and tsunamis in Cascadia. *American Indian Culture and Research Journal*, 31(4), 1–24. <https://doi.org/10.17953/aicr.31.4.3374595624774617>
- Troels-Smith, J. (1955). Characterization of Unconsolidated Sediments. Geological Survey of Denmark IV.
- Upton, M., Parnell, A., & Cahill, N. (2023). reslr: An R package for relative sea level modelling. arXiv:2306.10847. <https://doi.org/10.48550/arXiv.2306.10847>
- U.S. Census Bureau. (2022). Quick Facts United States Population Estimate Charts. U.S. Census Bureau. <https://www.census.gov/quickfacts/geo/chart/US/PST045222>

- Vázquez Riveiros, N., Babalola, A. O., Boudreau, R. E. A., Patterson, R. T., Roe, H. M., & Doherty, C. (2007). Modern distribution of salt marsh foraminifera and thecamoebians in the Seymour–Belize Inlet complex, British Columbia, Canada. *Marine Geology*, 242(1–3), 39–63. <https://doi.org/10.1016/j.margeo.2006.08.009>
- Walker, J. S., Cahill, N., Khan, N. S., Shaw, T. A., Barber, D., Miller, K. G., Kopp, R. E., & Horton, B. P. (2020). Incorporating temporal and spatial variability of salt-marsh foraminifera into sea-level reconstructions. *Marine Geology*, 429, 106293. <https://doi.org/10.1016/j.margeo.2020.106293>
- Walton, M. A. L., Staisch, L. M., Dura, T., Pearl, J. K., Sherrod, B., Gomberg, J., Engelhart, S., Tréhu, A., Watt, J., Perkins, J., Witter, R. C., Bartlow, N., Goldfinger, C., Kelsey, H., Morey, A. E., Sahakian, V. J., Tobin, H., Wang, K., Wells, R., & Wirth, E. (2021). Toward an integrative geological and geophysical view of Cascadia subduction zone earthquakes. *Annual Review of Earth and Planetary Sciences*, 49(1), 367–398. <https://doi.org/10.1146/annurev-earth-071620-065605>
- Wang, P.-L., Engelhart, S. E., Wang, K., Hawkes, A. D., Horton, B. P., Nelson, A. R., & Witter, R. C. (2013). Heterogeneous rupture in the great Cascadia earthquake of 1700 inferred from coastal subsidence estimates: GREAT CASCADIA EARTHQUAKE OF 1700. *Journal of Geophysical Research: Solid Earth*, 118(5), 2460–2473. <https://doi.org/10.1002/jgrb.50101>
- Watcham, E. P., Shennan, I., & Barlow, N. L. M. (2013). Scale considerations in using diatoms as indicators of sea-level change: Lessons from Alaska. *Journal of Quaternary Science*, 28(2), 165–179. <https://doi.org/10.1002/jqs.2592>
- Wesson, R. L., Melnick, D., Cisternas, M., Moreno, M., & Ely, L. L. (2015). Vertical deformation through a complete seismic cycle at Isla Santa María, Chile. *Nature Geoscience*, 8(7), 547–551. <https://doi.org/10.1038/ngeo2468>
- Williams, H. F. L., Hutchinson, I., & Nelson, A. R. (2005). Multiple sources for late-Holocene tsunamis at discovery bay, Washington state, USA. *The Holocene*, 15(1), 60–73. <https://doi.org/10.1191/0956683605hl784rp>
- Williams, S., Garrett, E., Moss, P., Bartlett, R., & Gehrels, R. (2021). Development of a training set of contemporary salt-marsh foraminifera for late Holocene sea-level reconstructions in southeastern Australia. *Open Quaternary*, 7(1), 4. <https://doi.org/10.5334/oq.93>
- Wirth, E. A., Frankel, A. D., Marafi, N., Vidale, J., & Stephenson, W. J. (2018). Broadband synthetic seismograms for magnitude 9 earthquakes on the Cascadia megathrust based on 3D simulations and stochastic synthetics, part 2: Rupture parameters and variability. *Bulletin of the Seismological Society of America*, 108(5A), 2370–2388. <https://doi.org/https://doi.org/10.1785/0120180029>
- Witter, R. C., Kelsey, H. M., & Hemphill-Haley, E. (2003). Great Cascadia earthquakes and tsunamis of the past 6700 years, Coquille River estuary, southern coastal Oregon. *Geological Society of America Bulletin*, 115(10), 1289. <https://doi.org/10.1130/B25189.1>

- Witter, R. C., Zhang, Y. J., Wang, K., Priest, G. R., Goldfinger, C., Stimely, L., English, J. T., & Ferro, P. A. (2013). Simulated tsunami inundation for a range of Cascadia megathrust earthquake scenarios at Bandon, Oregon, USA. *Geosphere*, 9(6), 1783–1803. <https://doi.org/10.1130/GES00899.1>
- Wright, A. J., Edwards, R. J., & Van De Plassche, O. (2011). Reassessing transfer-function performance in sea-level reconstruction based on benthic salt-marsh foraminifera from the Atlantic coast of NE North America. *Marine Micropaleontology*, 81(1–2), 43–62. <https://doi.org/10.1016/j.marmicro.2011.07.003>
- Yorath, C. J. (2005). *The geology of southern Vancouver Island* (Rev. 2005). Harbour Pub.

Appendix A.

Supporting Information for Chapter 2

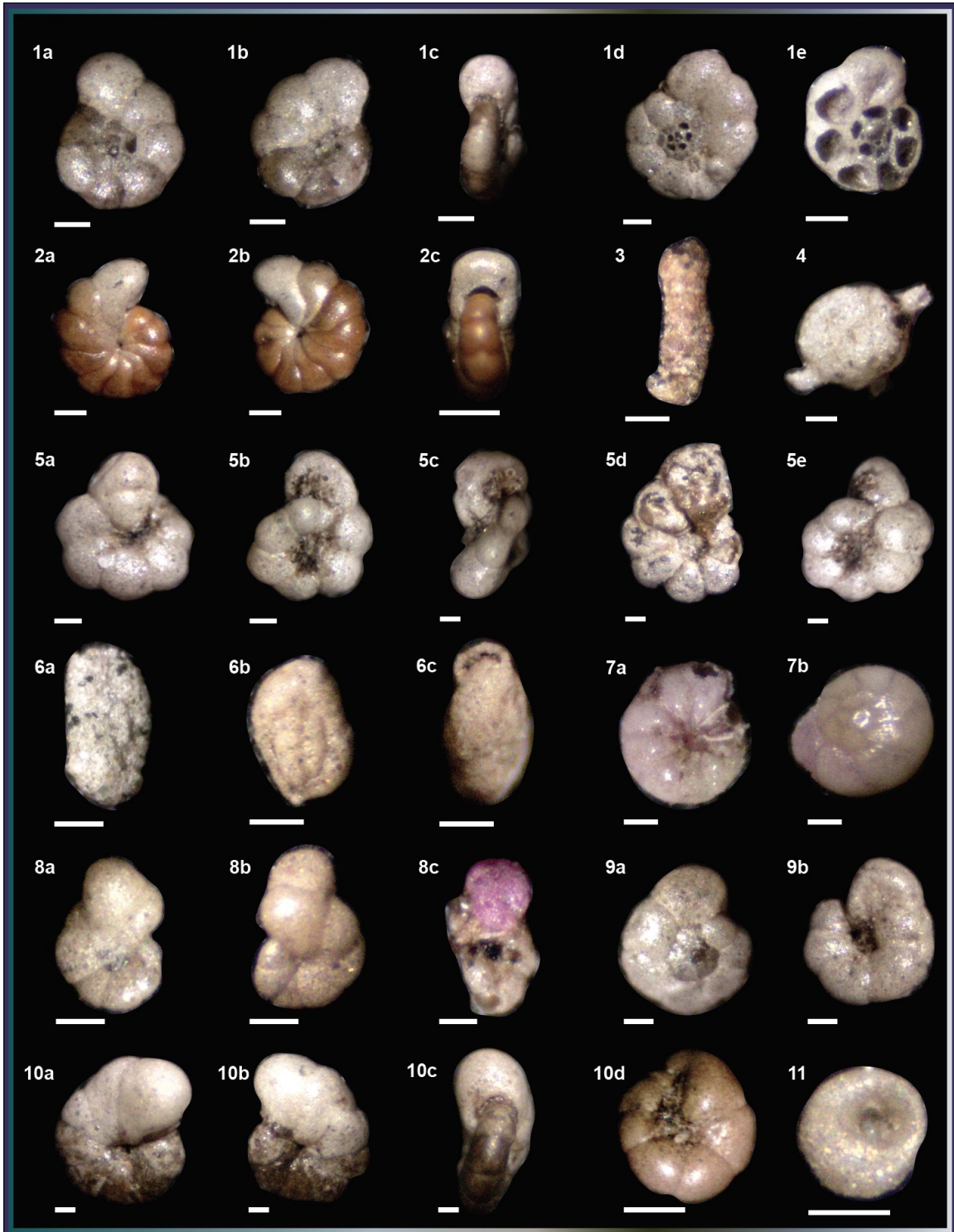
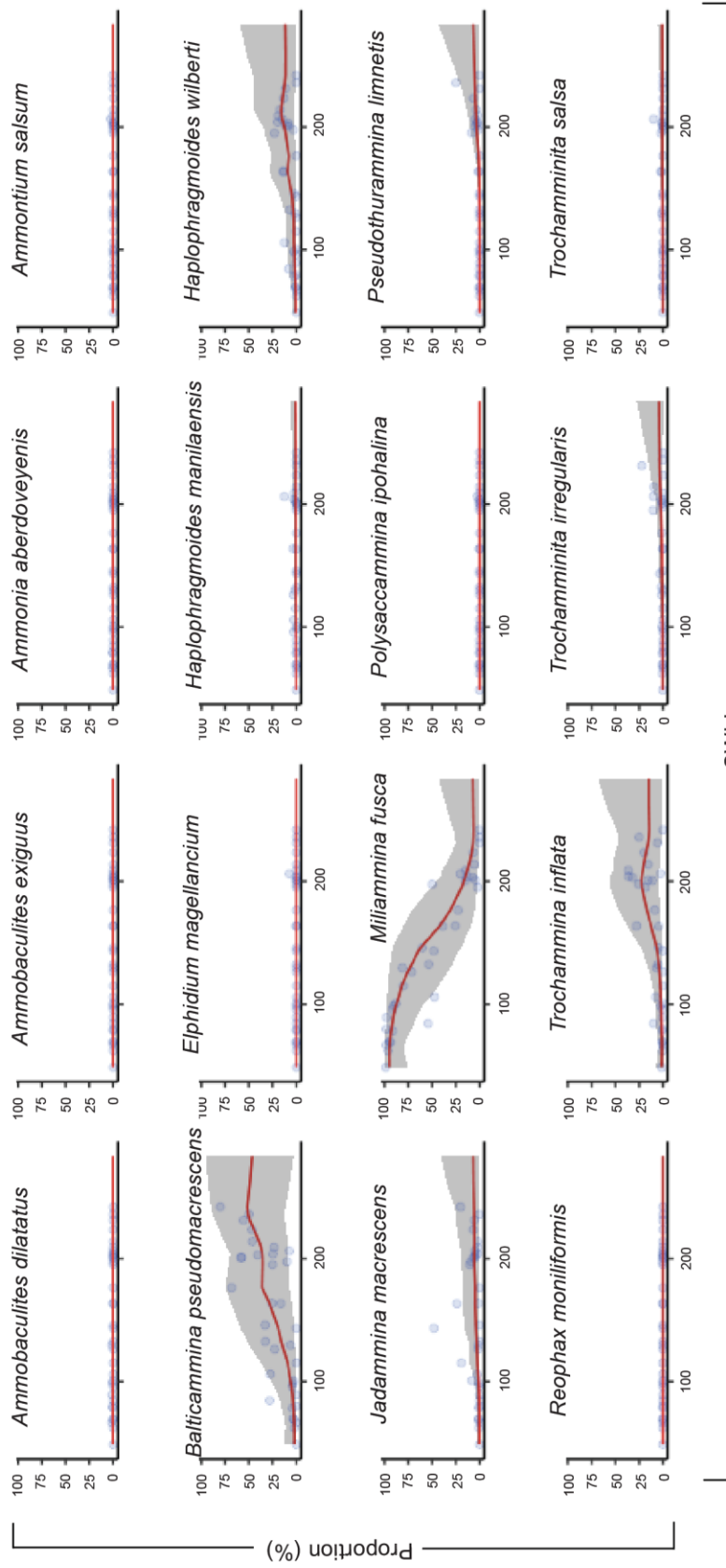


Figure A.1. Images of Foraminifera with 100 μm scale bar in white. (1a) *Balticammina pseudomacrescens*, dorsal view, (1b) *Balticammina pseudomacrescens*, ventral view, (1c) *Balticammina pseudomacrescens*, apertural view, (1d) *Balticammina pseudomacrescens*, dorsal view, (1e) (1a) *Balticammina pseudomacrescens*, dorsal view with collapsed chambers, (2a-b) *Haplophragmoides manilaensis*, (2c) *Haplophragmoides manilaensis*, apertural view, (3), *Reophax nana*, (4) *Pseudothuramina limnetis*, (5a) *Jadammina macrescens*, ventral side, (5b) *Jadammina macrescens*, dorsal side, (5c) *Jadammina macrescens*, apertural side, (5d) *Jadammina macrescens*, dorsal side, (5e) *Jadammina macrescens*, dorsal side, (6a,b) *Miliammina fusca*, (6c) *Miliammina fusca*, apertural view, (7a) *Ammobaculites diltatus*, ventral side, (7b) *Ammobaculites diltatus*, dorsal side, (8a,b) *Trochamminita irregularis*, (8c) *Trochamminita irregularis*, apertural side, (9a) *Trochammina inflata*, dorsal side, (9b) *Trochammina inflata*, ventral side, (10a,b,d) *Haplophragmoides wilberi*, (10c) *Haplophragmoides wilberi*, apertural view, (11) testate amoebae *Centropyxis aculeata*.

Species Response Curves

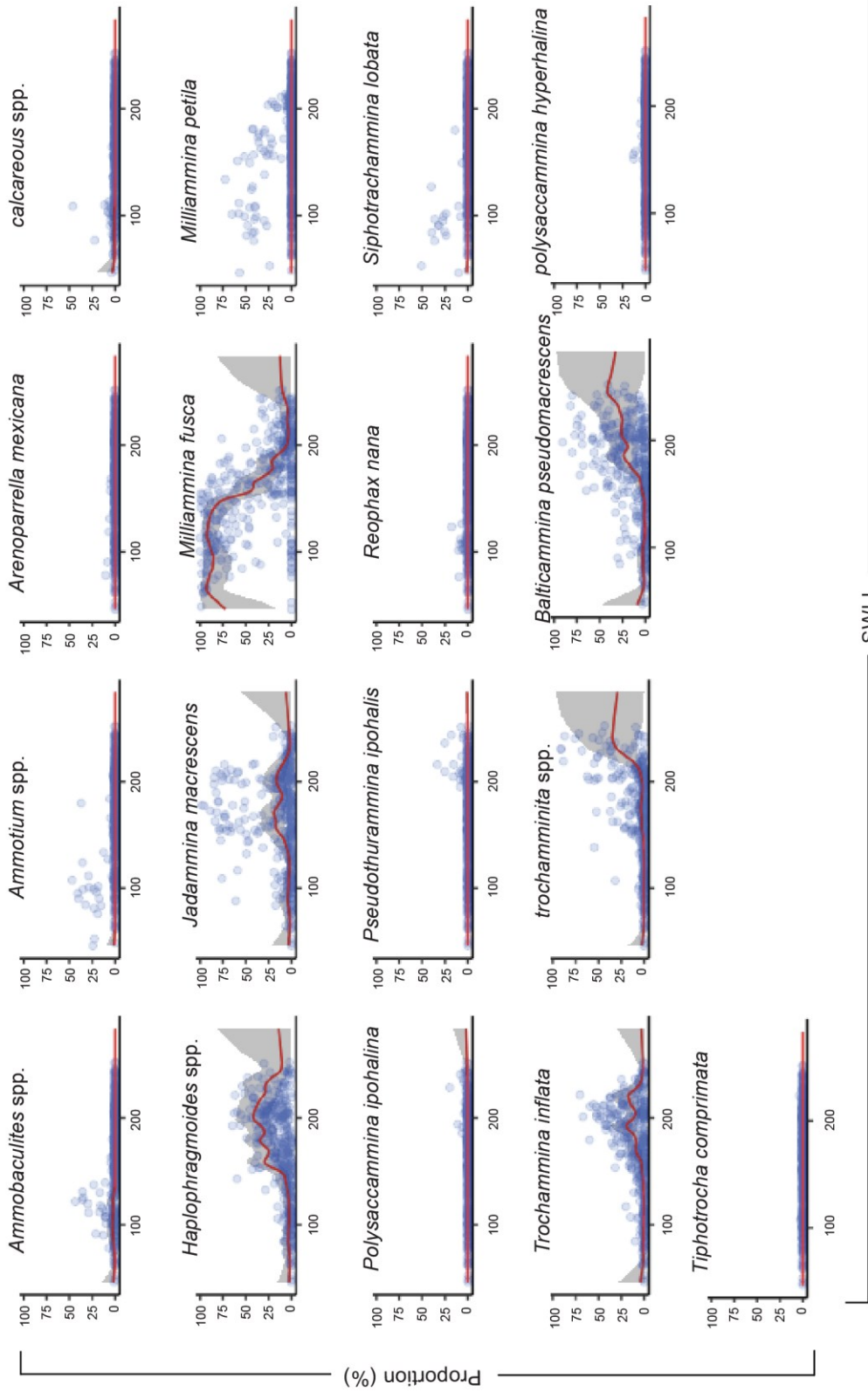


SWLI

— Mean model estimates ■ 95% credible interval ● Local observed dataset (Port Alberni)

Figure A.2. Modelled species response curve of all observed local Port Alberni foraminifera training set from the Bayesian transfer function relative to elevation (SWLI). The observed foraminifera species are shown in the blue dots, the mean model is shown in the red solid line and the 95% credible intervals is shown in the grey shaded area.

Species Response Curves



— Mean model estimates ■ 95% credible interval ● Regional observed dataset (Cascadia 2)

Figure A.3. Modelled species response curve of all observed local regional *Cascadia* foraminifera training set from the Bayesian transfer function relative to elevation (SWLI). The observed foraminifera species are shown in the blue dots, the mean model is shown in the red solid line and the 95% credible intervals is shown in the grey shaded area.

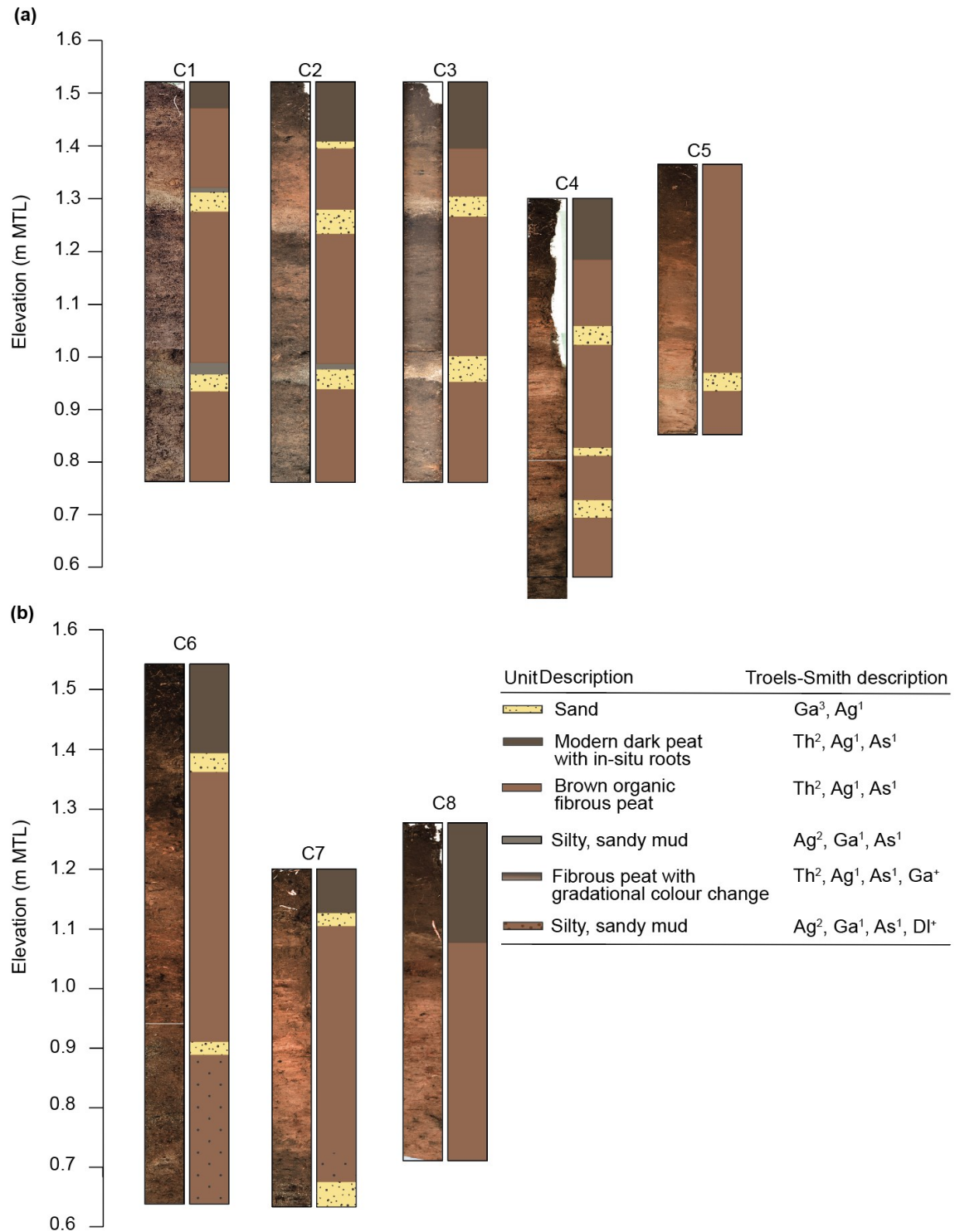


Figure A.4. Zoomed in photo of Fig. 2.7. Optical images of Port Alberni Marsh sediment cores and corresponding stratigraphic log based on Troels-Smith classification of eight sediment cores. Elevation is relative to MTL, m.

Table A.1. Modern observation at the Port Alberni salt marsh. Elevation (MTL, SWLI), location, vegetation, LOI %, relative abundance of foraminifera, and total counts per 1 cm³.

Louise Riou MS.c. Master Datasheet of Port Alberni modern foraminifera. September 2021- May 2024						
Station	St.1	St.2	St.3	St.4	St.5	St.6
Transect	T1	T1	T1	T1	T1	T1
Easting	366962.85	366963.64	366963.72	366963.64	366963.51	366963.39
Northing	5457163.80	5457164.80	5457165.72	5457167.17	5457168.37	5457169.39
Marsh zone	tidal flat	tidal flat	low	low	low	low
Elevation (m MTL)	0.95	1.009	1.186	1.324	1.535	1.782
SWLI	95.86	100.66	115.05	126.27	143.42	163.49
Vegetation	zp	zp	cl	jb, cl, pp, ds	jb, pp, ds	jb, pp, ds, gm
LOI Carbon (%)	12.21%	28.42%	23.10%	24.51%	42.30%	33.66%
Foraminifera relative abundance						
<i>Balticamina pseudomacresens</i>	0.042	0.032	0.004	0.227	0.000	0.154
<i>Trochammina irregularis</i>	0.000	0.012	0.000	0.009	0.027	0.000
<i>Haplophragmoides wilberti</i>	0.006	0.000	0.000	0.000	0.004	0.126
<i>Trochammina inflata</i>	0.003	0.004	0.000	0.004	0.000	0.047
<i>Jadammina macrescens</i>	0.003	0.084	0.189	0.018	0.469	0.238
<i>Miliammina fusca</i>	0.920	0.868	0.796	0.693	0.481	0.383
<i>Trochammina salsa</i>	0.000	0.000	0.000	0.000	0.000	0.019
<i>Polysaccamina ipohalina</i>	0.000	0.000	0.000	0.000	0.000	0.000
<i>Eggerella advena</i>	0.000	0.000	0.000	0.000	0.000	0.000
<i>Lobatula fletcheri</i>	0.000	0.000	0.000	0.004	0.000	0.000
<i>Pseudothurammina limnetis</i>	0.000	0.000	0.000	0.000	0.004	0.019
<i>Reophax nana</i>	0.000	0.000	0.000	0.000	0.000	0.000
<i>Reophax moniliformis</i>	0.000	0.000	0.000	0.000	0.000	0.000
<i>Ammobaculites exiguus</i>	0.000	0.000	0.000	0.000	0.000	0.000
<i>Ammonia aberdoveyensis</i>	0.000	0.000	0.000	0.000	0.000	0.000
<i>Ammontium salsum</i>	0.000	0.000	0.000	0.000	0.000	0.000
<i>Elphidium magellanicum</i>	0.000	0.000	0.000	0.000	0.000	0.000
<i>Haplophragmoides manilaensis</i>	0.026	0.000	0.011	0.031	0.004	0.005
<i>Ammobaculites dilatatus</i>	0.000	0.000	0.000	0.000	0.004	0.000
<i>Testate amoebae</i>	0.000	0.000	0.000	0.013	0.008	0.009
Total foraminifera count per 1 cm ³	499	100	106	72	59	68
Vegetation abbreviation (organized from most to least abundant: zp... <i>Zostera sp</i> ; cl... <i>Carex lyngbyei</i> ; pp... <i>Potentilla pacifica</i> ; jb... <i>Juncus balticus</i> ; ds... <i>Distichlis spicata</i> ; sa... <i>Scirpus americanus</i> ; gm... <i>Glaux maritima</i> ; ss... <i>Symphyotrichum subspicatum</i> ; ca... <i>Cirsium arvense</i> ; rn... <i>Rosa nutkana</i> ; pb... <i>Populus balsamifera</i> ; cg...common grass; ds... <i>Deschampsia cespitosa</i> ; sm... <i>Soligago multiradiata</i>)						

Louise Riou MS.c. Master Datasheet of Port Alberni modern foraminifera. September 2021- May 2024						
Station	St.7	St.8	St.9	St.10	St.11	St.12
Transect	T1	T1	T1	T1	T1	T1
Easting	366963.09	366962.05	366960.88	366965.57	366975.67	366973.60
Northing	5457170.67	5457172.44	5457177.91	5457189.60	5457209.12	5457242.41
Marsh zone	low	high	high	high	high	high
Elevation (m MTL)	2.202	2.28	2.343	2.244	2.309	2.27
SWL	197.63	203.98	209.10	201.05	206.33	203.16
Vegetation	jb, pp, ds, gm	ds, pp, ca	cl, pp, ds	cl, pp, ds, ss	pp, ds, ss	cg
LOI Carbon (%)	54.56%	62.63%	54.28%	58.94%	68.66%	54.24%
Foraminifera relative abundance						
<i>Balticammina pseudomacresens</i>	0.096	0.244	0.225	0.564	0.080	0.414
<i>Trochammina irregularis</i>	0.004	0.004	0.004	0.000	0.112	0.009
<i>Haplophragmoides wilberti</i>	0.032	0.194	0.199	0.103	0.160	0.084
<i>Trochammina inflata</i>	0.253	0.360	0.369	0.142	0.016	0.316
<i>Jadammina macrescens</i>	0.092	0.025	0.025	0.059	0.056	0.037
<i>Miliammina fusca</i>	0.502	0.136	0.140	0.044	0.192	0.070
<i>Trochammina salsa</i>	0.000	0.000	0.000	0.005	0.088	0.009
<i>Polysaccharina ipohalina</i>	0.000	0.000	0.000	0.000	0.024	0.000
<i>Eggerella advena</i>	0.000	0.000	0.000	0.000	0.000	0.000
<i>Lobatula fletcheri</i>	0.000	0.000	0.000	0.000	0.000	0.000
<i>Pseudothurammina limnetis</i>	0.016	0.017	0.017	0.044	0.056	0.033
<i>Reophax nana</i>	0.000	0.000	0.000	0.000	0.008	0.000
<i>Reophax moniliformis</i>	0.004	0.000	0.000	0.000	0.000	0.000
<i>Ammobaculites exiguus</i>	0.000	0.000	0.000	0.000	0.000	0.000
<i>Ammonia aberdoveyensis</i>	0.000	0.000	0.000	0.000	0.000	0.000
<i>Ammontium salsum</i>	0.000	0.000	0.000	0.000	0.016	0.000
<i>Elphidium magellanicum</i>	0.000	0.000	0.000	0.000	0.064	0.000
<i>Haplophragmoides manilaensis</i>	0.000	0.017	0.017	0.000	0.120	0.009
<i>Ammobaculites dilatatus</i>	0.000	0.000	0.000	0.000	0.000	0.005
<i>Testate amoebae</i>	0.000	0.004	0.004	0.039	0.008	0.014
Total foraminifera count per 1 cm ³	133	97	47	47	40	69
Vegetation abbreviation (organized from most to least abundant: zp... <i>Zostera</i> sp; cl... <i>Carex lyngbyei</i> ; pp... <i>Potentilla pacifica</i> ; jb... <i>Juncus balticus</i> ; ds... <i>Distichlis spicata</i> ; sa... <i>Scirpus americanus</i> ; gm... <i>Glaux maritima</i> ; ss... <i>Symphotrichum subspicatum</i> ; ca... <i>Cirsium arvense</i> ; rn... <i>Rosa nutkana</i> ; pb... <i>Populus balsamifera</i> ; cg...common grass; ds... <i>Deschampsia cespitosa</i> ; sm... <i>Soligago multiradiata</i>)						

Louise Riou M.S.c. Master Datasheet of Port Alberni modern foraminifera. September 2021- May 2024						
Station	St.13	St.14	St.15	St.16	St.17	St.18
Transect	T1	T1	T1	T1	T1	T1
Easting	366963.44	366957.79	366954.93	366950.85	366949.60	366947.78
Northing	5457254.80	5457260.07	5457260.88	5457262.23	5457264.54	5457264.59
Marsh zone	high	high	high	high	upland	upland
Elevation (m MTL)	2.52	2.675	2.987	3.26	3.413	3.841
SWLI	223.48	236.08	261.44	283.64	296.072	330.86
Vegetation	cg	ds, sa, ca	ds, ca	pb, rn	pb	pb
LOI Carbon (%)	54.99%	45.00%	85.11%	46.26%	49.25%	40.05%
Foraminifera relative abundance						
<i>Balticammina pseudomacresens</i>	0.444	0.500	0.000	0.000	0.000	0.000
<i>Trochammina irregularis</i>	0.000	0.000	0.000	0.000	0.000	1.000
<i>Haplophragmoides wilberti</i>	0.131	0.071	0.000	0.000	0.000	0.000
<i>Trochammina inflata</i>	0.181	0.143	0.000	0.000	0.000	0.000
<i>Jadammina macrescens</i>	0.075	0.000	0.000	0.000	0.000	0.000
<i>Miliammina fusca</i>	0.056	0.000	0.000	0.000	0.000	0.000
<i>Trochammina salsa</i>	0.006	0.000	0.000	0.000	0.000	0.000
<i>Polysaccammina ipohalina</i>	0.000	0.000	0.059	0.000	0.000	0.000
<i>Eggerella advena</i>	0.000	0.000	0.000	0.000	0.000	0.000
<i>Lobatula fletcheri</i>	0.000	0.000	0.000	0.000	0.000	0.000
<i>Pseudothurammina limnetis</i>	0.056	0.143	0.000	0.000	0.000	0.000
<i>Reophax nana</i>	0.000	0.000	0.000	0.000	0.000	0.000
<i>Reophax moniliformis</i>	0.000	0.000	0.000	0.000	0.000	0.000
<i>Ammobaculites exiguus</i>	0.000	0.000	0.000	0.000	0.000	0.000
<i>Ammonia aberdoveyensis</i>	0.000	0.000	0.000	0.000	0.000	0.000
<i>Ammonium salsum</i>	0.000	0.000	0.000	0.000	0.000	0.000
<i>Elphidium magellanicum</i>	0.000	0.000	0.000	0.000	0.000	0.000
<i>Haplophragmoides manilaensis</i>	0.000	0.000	0.000	0.000	0.000	0.000
<i>Ammobaculites dilatatus</i>	0.000	0.000	0.000	0.000	0.000	0.000
<i>Testate amoebae</i>	0.050	0.143	0.941	1.000	0.000	0.000
Total foraminifera count per 1 cm ³	32	4	7	2	0	0
Vegetation abbreviation (organized from most to least abundant: zp... <i>Zostera</i> sp; cl... <i>Carex lyngbyei</i> ; pp... <i>Potentilla pacifica</i> ; jb... <i>Juncus balticus</i> ; ds... <i>Distichlis spicata</i> ; sa... <i>Scirpus americanus</i> ; gm... <i>Glaux maritima</i> ; ss... <i>Symphyotrichum subspicatum</i> ; ca... <i>Cirsium arvense</i> ; rn... <i>Rosa nutkana</i> ; pb... <i>Populus balsamifera</i> ; cg...common grass; ds... <i>Deschampsia cespitosa</i> ; sm... <i>Solidago multiradiata</i>)						

Louise Riou MS.c. Master Datasheet of Port Alberni modern foraminifera. September 2021- May 2024						
Station	St.1	St.2	St.3	St.4	St.5	St.6
Transect	T2	T2	T2	T2	T2	T2
Easting	366623.91	366631.64	366636.07	366637.66	366639.48	366642.57
Northing	5457035.28	5457023.05	5457014.50	5457011.91	5457009.69	5457004.29
Marsh zone	tidal flat	tidal flat	tidal flat	tidal flat	tidal flat	low
Elevation (m MTL)	0.37	0.592	0.751	0.869	0.985	1.365
SWLI	48.72	66.76	79.69	89.28	98.71	129.60
Vegetation	n/a	n/a	zp	zp	zp	jb
LOI Carbon (%)	4.36%	9.58%	9.68%	3.65%	8.62%	26.78%
Foraminifera relative abundance						
<i>Balticamina pseudomacresens</i>	0.000	0.000	0.000	0.000	0.033	0.063
<i>Trochammina irregularis</i>	0.000	0.000	0.000	0.000	0.000	0.000
<i>Haplophragmoides wilberti</i>	0.004	0.000	0.000	0.004	0.027	0.008
<i>Trochammina inflata</i>	0.011	0.000	0.003	0.004	0.027	0.060
<i>Jadammina macrescens</i>	0.000	0.000	0.000	0.000	0.000	0.016
<i>Miliammina fusca</i>	0.982	0.982	0.979	0.981	0.900	0.790
<i>Trochammina salsa</i>	0.000	0.000	0.000	0.000	0.000	0.012
<i>Polysaccammina ipohalina</i>	0.000	0.000	0.000	0.000	0.000	0.000
<i>Eggerella advena</i>	0.000	0.000	0.000	0.000	0.000	0.000
<i>Lobatula fletcheri</i>	0.000	0.000	0.000	0.000	0.000	0.000
<i>Pseudothuramina limnetis</i>	0.000	0.000	0.000	0.000	0.000	0.000
<i>Reophax nana</i>	0.000	0.000	0.000	0.000	0.000	0.000
<i>Reophax moniliformis</i>	0.000	0.000	0.000	0.000	0.000	0.000
<i>Ammobaculites exiguus</i>	0.000	0.000	0.000	0.000	0.003	0.000
<i>Ammonia aberdoveyensis</i>	0.000	0.004	0.009	0.000	0.000	0.000
<i>Ammontium salsum</i>	0.000	0.000	0.000	0.000	0.000	0.000
<i>Elphidium magellanicum</i>	0.000	0.000	0.000	0.000	0.000	0.000
<i>Haplophragmoides manilaensis</i>	0.000	0.000	0.000	0.000	0.000	0.016
<i>Ammobaculites dilatatus</i>	0.000	0.014	0.009	0.011	0.010	0.008
<i>Testate amoebae</i>	0.004	0.000	0.000	0.000	0.000	0.028
Total foraminifera count per 1 cm ³	73	151	263	426	240	81
Vegetation abbreviation (organized from most to least abundant: zp... <i>Zostera sp</i> ; cl... <i>Carex lyngbyei</i> ; pp... <i>Potentilla pacifica</i> ; jb... <i>Juncus balticus</i> ; ds... <i>Distichlis spicata</i> ; sa... <i>Scirpus americanus</i> ; gm... <i>Glaux maritima</i> ; ss... <i>Symphyotrichum subspicatum</i> ; ca... <i>Cirsium arvense</i> ; rn... <i>Rosa nutkana</i> ; pb... <i>Populus balsamifera</i> ; cg...common grass; ds... <i>Deschampsia cespitosa</i> ; sm... <i>Soligago multiradiata</i>)						

Louise Riou MS.c. Master Datasheet of Port Alberni modern foraminifera. September 2021- May 2024						
Station	St.7	St.8	St.9	St.10	St.11	St.1
Transect	T2	T2	T2	T2	T2	T3
Easting	366643.57	366648.06	366663.89	366670.54	366678.21	366236.06
Northing	5457001.52	5456996.87	5456984.98	5456975.88	5456940.48	5456610.19
Marsh zone	low	high	high	high	high	tidal
Elevation (m MTL)	1.785	2.038	2.403	2.616	2.749	0.536
SWLI	163.74	195.11	213.97	231.29	242.10	62.21
Vegetation	jb	ds, pp, cg	sm	rn, pp	cg, jb, dc	zp
LOI Carbon (%)	45.69%	44.31%	52.88%	62.17%	49.32%	10.14%
Foraminifera relative abundance						
<i>Balticammina pseudomacresens</i>	0.252	0.242	0.449	0.515	0.889	0.016
<i>Trochammina irregularis</i>	0.000	0.108	0.098	0.186	0.000	0.006
<i>Haplophragmoides wilberti</i>	0.137	0.238	0.174	0.124	0.000	0.000
<i>Trochammina inflata</i>	0.274	0.179	0.143	0.072	0.000	0.003
<i>Jadammina macrescens</i>	0.015	0.096	0.023	0.052	0.111	0.003
<i>Miliammina fusca</i>	0.256	0.029	0.057	0.000	0.000	0.958
<i>Trochammina salsa</i>	0.026	0.017	0.000	0.010	0.000	0.000
<i>Polysaccammina ipohalina</i>	0.000	0.000	0.000	0.000	0.000	0.000
<i>Eggerella advena</i>	0.000	0.000	0.000	0.000	0.000	0.000
<i>Lobatula fletcheri</i>	0.000	0.000	0.000	0.000	0.000	0.000
<i>Pseudothurammina limnetis</i>	0.004	0.079	0.045	0.000	0.000	0.000
<i>Reophax nana</i>	0.000	0.000	0.000	0.000	0.000	0.000
<i>Reophax moniliformis</i>	0.000	0.000	0.000	0.000	0.000	0.000
<i>Ammobaculites exiguus</i>	0.000	0.000	0.000	0.000	0.000	0.000
<i>Ammonia aberdoveyensis</i>	0.000	0.000	0.000	0.000	0.000	0.000
<i>Ammontium salsum</i>	0.000	0.000	0.000	0.000	0.000	0.000
<i>Elphidium magellanicum</i>	0.000	0.000	0.000	0.000	0.000	0.000
<i>Haplophragmoides manilaensis</i>	0.033	0.000	0.000	0.010	0.000	0.000
<i>Ammobaculites dilatatus</i>	0.000	0.000	0.000	0.000	0.000	0.000
<i>Testate amoebae</i>	0.004	0.013	0.011	0.031	0.000	0.013
Total foraminifera count per 1 cm ³	86	48	53	19	5	165
Vegetation abbreviation (organized from most to least abundant: zp... <i>Zostera sp.</i> ; cl... <i>Carex lyngbyei</i> ; pp... <i>Potentilla pacifica</i> ; jb... <i>Juncus balticus</i> ; ds... <i>Distichlis spicata</i> ; sa... <i>Scirpus americanus</i> ; gm... <i>Glaux maritima</i> ; ss... <i>Symphotrichum subspicatum</i> ; ca... <i>Cirsium arvense</i> ; rn... <i>Rosa nutkana</i> ; pb... <i>Populus balsamifera</i> ; cg...common grass; ds... <i>Deschampsia cespitosa</i> ; sm... <i>Solidago multiradiata</i>)						

Louise Riou MS.c. Master Datasheet of Port Alberni modern foraminifera. September 2021- May 2024						
Station	St.2	St.3	St.4	St.5	St.6	St.7
Transect	T3	T3	T3	T3	T3	T3
Easting	366238.45	366241.46	366243.47	366245.69	366247.56	366249.05
Northing	5456611.59	5456612.93	5456613.82	5456615.06	5456616.14	5456617.51
Marsh zone	tidal flat	tidal flat	tidal flat	low	low	low
Elevation (m MTL)	0.63	0.621	0.733	0.809	1.073	1.401
SWLI	69.85	69.12	78.23	84.40	105.86	132.52
Vegetation	zp	zp	zp	zp	jb, cl	jb, cl
LOI Carbon (%)	12.47%	5.14%	1.99%	2.52%	7.39%	6.21%
Foraminifera relative abundance						
<i>Balticamina pseudomacresens</i>	0.034	0.023	0.045	0.263	0.278	0.323
<i>Trochammina irregularis</i>	0.000	0.004	0.004	0.008	0.010	0.019
<i>Haplophragmoides wilberti</i>	0.007	0.008	0.019	0.076	0.132	0.061
<i>Trochammina inflata</i>	0.000	0.008	0.004	0.097	0.068	0.046
<i>Jadammina macrescens</i>	0.007	0.008	0.004	0.000	0.015	0.008
<i>Miliammina fusca</i>	0.949	0.936	0.900	0.500	0.473	0.521
<i>Trochammina salsa</i>	0.000	0.004	0.000	0.000	0.000	0.000
<i>Polysaccamina ipohalina</i>	0.000	0.000	0.000	0.000	0.000	0.000
<i>Eggerella advena</i>	0.000	0.000	0.000	0.000	0.000	0.000
<i>Lobatula fletcheri</i>	0.000	0.000	0.000	0.000	0.000	0.000
<i>Pseudothuramina limnetis</i>	0.000	0.000	0.000	0.000	0.000	0.000
<i>Reophax nana</i>	0.000	0.000	0.000	0.000	0.000	0.000
<i>Reophax moniliformis</i>	0.000	0.000	0.000	0.000	0.000	0.000
<i>Ammobaculites exiguus</i>	0.000	0.000	0.000	0.000	0.000	0.000
<i>Ammonia aberdoveyensis</i>	0.000	0.000	0.000	0.000	0.000	0.000
<i>Ammonium salsum</i>	0.000	0.000	0.000	0.000	0.000	0.000
<i>Elphidium magellanicum</i>	0.000	0.000	0.000	0.000	0.000	0.000
<i>Haplophragmoides manilaensis</i>	0.000	0.000	0.000	0.000	0.015	0.008
<i>Ammobaculites dilatatus</i>	0.000	0.000	0.000	0.000	0.000	0.000
<i>Testate amoebae</i>	0.003	0.011	0.026	0.055	0.010	0.015
Total foraminifera count per 1 cm ³	118	213	143	54	41	60
Vegetation abbreviation (organized from most to least abundant: zp... <i>Zostera</i> sp; d... <i>Carex lyngbyei</i> ; pp... <i>Potentilla pacifica</i> ; jb... <i>Juncus balticus</i> ; ds... <i>Distichlis spicata</i> ; sa... <i>Scirpus americanus</i> ; gm... <i>Glaux maritima</i> ; ss... <i>Symphotrichum subspicatum</i> ; ca... <i>Cirsium arvense</i> ; rn... <i>Rosa nutkana</i> ; pb... <i>Populus balsamifera</i> ; cg...common grass; ds... <i>Deschampsia cespitosa</i> ; sm... <i>Solidago multiradiata</i>)						

Louise Riou MS.c. Master Datasheet of Port Alberni modern foraminifera. September 2021- May 2024			
Station	St.8	St.9	St.10
Transect	T3	T3	T3
Easting	366250.35	366250.74	366252.00
Northing	5456618.29	5456618.70	5456620.54
Marsh zone	low	high	high
Elevation (m MTL)	1.566	1.942	2.24
SWLI	145.94	176.50	200.72
Vegetation	cl, jb	cl, jb	cl, jb
LOI Carbon (%)	9.16%	34.63%	34.54%
Foraminifera relative abundance			
<i>Balticammina pseudomacresens</i>	0.310	0.678	0.540
<i>Trochamminita irregularis</i>	0.000	0.007	0.011
<i>Haplophragmoides wilberti</i>	0.016	0.004	0.077
<i>Trochammin inflata</i>	0.041	0.082	0.103
<i>Jadammina macrescens</i>	0.000	0.000	0.040
<i>Miliammina fusca</i>	0.563	0.225	0.136
<i>Trochamminita salsa</i>	0.000	0.000	0.004
<i>Polysaccammina ipohalina</i>	0.000	0.000	0.000
<i>Eggerella advena</i>	0.000	0.000	0.000
<i>Lobatula fletcheri</i>	0.000	0.000	0.000
<i>Pseudothurammina limnetis</i>	0.000	0.000	0.015
<i>Reophax nana</i>	0.000	0.000	0.000
<i>Reophax moniliformis</i>	0.000	0.000	0.000
<i>Ammobaculites exiguus</i>	0.000	0.000	0.000
<i>Ammonia aberdoveyensis</i>	0.000	0.000	0.000
<i>Ammontium salsum</i>	0.000	0.000	0.000
<i>Elphidium magellanicum</i>	0.000	0.000	0.000
<i>Haplophragmoides manilaensis</i>	0.000	0.000	0.000
<i>Ammobaculites dilatatus</i>	0.000	0.000	0.000
<i>Testate amoebae</i>	0.069	0.004	0.073
Total foraminifera count per 1 cm ³	98	107	87
Vegetation abbreviation (organized from most to least abundant: zp... <i>Zostera</i> sp; cl... <i>Carex lyngbyei</i> ; pp... <i>Potentilla pacifica</i> ; jb... <i>Juncus balticus</i> ; ds... <i>Distichlis spicata</i> ; sa... <i>Scirpus americanus</i> ; gm... <i>Glaux maritima</i> ; ss... <i>Symphotrichum subspicatum</i> ; ca... <i>Cirsium arvense</i> ; rn... <i>Rosa nutkana</i> ; pb... <i>Populus balsamifera</i> ; cg...common grass; ds... <i>Deschampsia cespitosa</i> ; sm... <i>Soligago multiradiata</i>)			

Table A.2. C1 information. Depth of samples collected at 1 cm intervals, LOI carbon, prior information given to samples intervals (SWLI), relative abundance of foraminifera, and total counts per 1 cm³.

depth (cm)	0-1	1-2	2-3	3-4	4-5	5-6	6-7	7-8	8-9
LOI carbon (%)	0.00%	64.54%	63.13%	60.84%	53.18%	48.56%	54.16%	41.41%	48.62%
Prior SWLI range	143-223								
Foraminifera relative abundance									
<i>Balticammina pseudomacresens</i>	0	0.570	0.463	0.372	0.338	0.545	0.523	0.630	0.683
<i>Trochammina irregularis</i>	0	0.035	0.043	0.007	0.092	0.032	0.053	0.023	0.012
<i>Haplophragmoides wilberti</i>	0	0.227	0.220	0.285	0.262	0.156	0.159	0.104	0.183
<i>Trochammina inflata</i>	0	0.006	0.055	0.088	0.123	0.026	0.033	0.029	0.012
<i>Jadammina macrescens</i>	0	0.052	0.104	0.088	0.046	0.136	0.126	0.104	0.049
<i>Miliammina fusca</i>	0	0.052	0.043	0.109	0.077	0.032	0.026	0.040	0.024
<i>Trochammina salsa</i>	0	0.041	0.018	0.015	0.008	0.019	0.013	0.023	0.037
<i>Pseudothuramina limnetis</i>	0	0.017	0.030	0.022	0.031	0.006	0.000	0.006	0.000
<i>Haplophragmoides manilaensis</i>	0	0.000	0.024	0.015	0.015	0.026	0.053	0.023	0.000
<i>Testate amoebae</i>	0	0.000	0.000	0.000	0.008	0.019	0.013	0.017	0.000
Total foraminifera count per 1 cm ³	0	55	44	55	42	41	60	69	131

depth (cm)	9-10	10-11	11-12	12-13	13-14	14-15	15-16	16-17	17-18
LOI carbon (%)	32.29%	26.88%	34.15%	42.93%	42.9%	46.7%	43.09%	38.15%	33.51%
Prior SWLI range	143-223								
Foraminifera relative abundance									
<i>Balticammina pseudomacresens</i>	0.608	0.568	0.619	0.679	0.806	0.764	0.673	0.732	0.625
<i>Trochammina irregularis</i>	0.023	0.007	0.026	0.024	0.026	0.047	0.005	0.000	0.016
<i>Haplophragmoides wilberti</i>	0.159	0.142	0.160	0.131	0.077	0.058	0.050	0.061	0.049
<i>Trochammina inflata</i>	0.023	0.000	0.026	0.018	0.000	0.000	0.000	0.000	0.000
<i>Jadammina macrescens</i>	0.148	0.189	0.139	0.101	0.052	0.082	0.256	0.171	0.255
<i>Miliammina fusca</i>	0.000	0.000	0.005	0.006	0.000	0.011	0.005	0.006	0.000
<i>Trochammina salsa</i>	0.040	0.095	0.021	0.042	0.026	0.035	0.005	0.030	0.054
<i>Pseudothuramina limnetis</i>	0.000	0.000	0.000	0.000	0.000	0.000	0.000	0.000	0.000
<i>Haplophragmoides manilaensis</i>	0.000	0.000	0.000	0.000	0.000	0.000	0.000	0.000	0.000
<i>Testate amoebae</i>	0.000	0.000	0.005	0.000	0.013	0.000	0.005	0.000	0.000
Total foraminifera count per 1 cm ³	141	118	155	54	83	136	106	87	294

depth (cm)	18-19	19-20	20-21	21-22	22-23	23-24	24-25	25-26	26-27
LOI carbon (%)	30.76%	38.04%	22.54%	10.12%	6.22%	5.98%	14.86%	58.76%	63.40%
Prior SWLI range	143-223	143-223	100-223	0-100	0-100	0-100	0-100	143-223	143-223
Foraminifera relative abundance									
<i>Balticammina pseudomacresens</i>	0.607	0.756	0.741	0.524	0.692	0.625	0.753	0.827	0.762
<i>Trochamminita irregularis</i>	0.006	0.005	0.007	0.000	0.000	0.031	0.017	0.022	0.018
<i>Haplophragmoides wilberti</i>	0.104	0.118	0.116	0.048	0.154	0.219	0.167	0.086	0.101
<i>Trochammin inflata</i>	0.000	0.000	0.000	0.048	0.000	0.000	0.000	0.000	0.000
<i>Jadammina macrescens</i>	0.233	0.118	0.095	0.143	0.077	0.125	0.057	0.058	0.113
<i>Miliammina fusca</i>	0.000	0.005	0.007	0.238	0.077	0.000	0.006	0.000	0.000
<i>Trochamminita salsa</i>	0.049	0.000	0.034	0.000	0.000	0.000	0.000	0.000	0.006
<i>Pseudothurammina limnetis</i>	0.000	0.000	0.000	0.000	0.000	0.000	0.000	0.000	0.000
<i>Haplophragmoides manilaensis</i>	0.000	0.000	0.000	0.000	0.000	0.000	0.000	0.000	0.000
<i>Testate amoebae</i>	0.000	0.000	0.000	0.000	0.000	0.000	0.000	0.007	0.000
Total foraminifera count per 1 cm ³	130	177	39	6	8	10	46	74	90

depth (cm)	27-28	28-29	29-30	30-31	31-32	32-33	33-34	34-35	35-36
LOI carbon (%)	61.43%	47.59%	40.10%	35.57%	26.64%	23.20%	26.29%	29.27%	33.70%
Prior SWLI range	143-223	143-223	143-223	143-223	100-223	100-223	100-223	100-223	200-223
Foraminifera relative abundance									
<i>Balticammina pseudomacresens</i>	0.730	0.683	0.71	0.84	0.83	0.93	0.91	0.92	0.79
<i>Trochamminita irregularis</i>	0.010	0.014	0.01	0.00	0.01	0.00	0.02	0.00	0.02
<i>Haplophragmoides wilberti</i>	0.069	0.079	0.06	0.07	0.07	0.01	0.02	0.05	0.03
<i>Trochammin inflata</i>	0.000	0.000	0.00	0.00	0.00	0.02	0.01	0.00	0.03
<i>Jadammina macrescens</i>	0.176	0.180	0.14	0.08	0.04	0.04	0.03	0.01	0.02
<i>Miliammina fusca</i>	0.000	0.007	0.01	0.00	0.00	0.00	0.01	0.00	0.03
<i>Trochamminita salsa</i>	0.010	0.036	0.07	0.01	0.04	0.00	0.01	0.00	0.00
<i>Pseudothurammina limnetis</i>	0.000	0.000	0.00	0.00	0.00	0.00	0.00	0.00	0.00
<i>Haplophragmoides manilaensis</i>	0.000	0.000	0.00	0.00	0.00	0.00	0.00	0.00	0.00
<i>Testate amoebae</i>	0.005	0.000	0.00	0.00	0.01	0.00	0.00	0.01	0.09
Total foraminifera count per 1 cm ³	163	222	88.00	53.87	60.80	54.40	119.20	111.20	46.00

depth (cm)	36-37	37-38	38-39	39-40	40-41	41-42	42-43
LOI carbon (%)	28.89%	29.64%	34.95%	30.31%	36.80%	30.10%	26.04%
Prior SWLI range	100-223	200-223	143-223	143-223	143-223	143-223	100-223
Foraminifera relative abundance							
<i>Balticammina pseudomacresens</i>	0.89	0.85	0.93	0.88	0.89	0.91	0.90
<i>Trochamminita irregularis</i>	0.00	0.00	0.00	0.02	0.01	0.03	0.03
<i>Haplophragmoides wilberti</i>	0.04	0.04	0.01	0.05	0.04	0.00	0.00
<i>Trochammin inflata</i>	0.02	0.00	0.00	0.00	0.00	0.01	0.01
<i>Jadammina macrescens</i>	0.03	0.00	0.02	0.00	0.03	0.02	0.02
<i>Miliammina fusca</i>	0.00	0.03	0.02	0.01	0.01	0.01	0.01
<i>Trochamminita salsa</i>	0.00	0.00	0.00	0.00	0.01	0.01	0.01
<i>Pseudothurammina limnetis</i>	0.00	0.00	0.00	0.00	0.00	0.00	0.00
<i>Haplophragmoides manilaensis</i>	0.00	0.00	0.00	0.00	0.00	0.00	0.00
<i>Testate amoebae</i>	0.03	0.08	0.00	0.05	0.02	0.01	0.01
Total foraminifera count per 1 cm ³	35.20	58.13	119.20	111.20	46.00	35.20	58.13

depth (cm)	43-44	44-45	45-46	46-47	47-48	48-49	49-50
LOI carbon (%)	28.08%	23.79%	26.10%	28.22%	34.88%	15.25%	8.45%
Prior SWLI range	100-223	100-223	100-223	100-223	143-223	100-223	143-223
Foraminifera relative abundance							
<i>Balticammina pseudomacresens</i>	0.88	0.74	0.83	0.88	0.85	0.85	0.765
<i>Trochamminita irregularis</i>	0.01	0.00	0.00	0.00	0.02	0.01	0.022
<i>Haplophragmoides wilberti</i>	0.07	0.06	0.08	0.07	0.08	0.10	0.156
<i>Trochammin inflata</i>	0.01	0.01	0.01	0.01	0.03	0.00	0.000
<i>Jadammina macrescens</i>	0.02	0.01	0.00	0.03	0.01	0.00	0.045
<i>Miliammina fusca</i>	0.02	0.07	0.02	0.00	0.02	0.03	0.006
<i>Trochamminita salsa</i>	0.00	0.00	0.02	0.01	0.00	0.00	0.000
<i>Pseudothurammina limnetis</i>	0.00	0.00	0.00	0.00	0.00	0.00	0.000
<i>Haplophragmoides manilaensis</i>	0.00	0.00	0.00	0.00	0.00	0.00	0.000
<i>Testate amoebae</i>	0.01	0.10	0.04	0.00	0.00	0.01	0.006
Total foraminifera count per 1 cm ³	96.00	77.60	87.20	180.80	58.67	124.80	143

depth (cm)	50-51	51-52	52-53	53-54	54-55	55-56	56-57	57-58	58-59
LOI carbon (%)	20.36%	7.12%	3.81%	2.47%	4.19%	23.94%	41.26%	36.87%	43.58%
Prior SWLI range	100-223	143-223	200-223	0-100	0-100	0-100	0-100	0-100	200-223
Foraminifera relative abundance									
<i>Balticammina pseudomacresens</i>	0.896	0.904	0.831	0.641	0.273	0.500	0.350	0.576	0.653
<i>Trochamminita irregularis</i>	0.010	0.017	0.007	0.031	0.000	0.000	0.000	0.000	0.003
<i>Haplophragmoides wilberti</i>	0.045	0.025	0.061	0.109	0.273	0.000	0.100	0.054	0.090
<i>Trochammin inflata</i>	0.000	0.000	0.000	0.000	0.000	0.000	0.000	0.011	0.000
<i>Jadammina macrescens</i>	0.035	0.029	0.027	0.078	0.000	0.250	0.000	0.011	0.063
<i>Miliammina fusca</i>	0.005	0.008	0.000	0.094	0.455	0.250	0.350	0.283	0.010
<i>Trochamminita salsa</i>	0.000	0.000	0.000	0.000	0.000	0.000	0.000	0.000	0.000
<i>Pseudothurammina limnetis</i>	0.000	0.000	0.000	0.000	0.000	0.000	0.000	0.000	0.000
<i>Haplophragmoides manilaensis</i>	0.000	0.000	0.000	0.000	0.000	0.000	0.000	0.000	0.000
<i>Testate amoebae</i>	0.010	0.017	0.074	0.047	0.000	0.000	0.200	0.065	0.180
Total foraminifera count per 1 cm ³	322	382	237	13	4	2	8	18	480

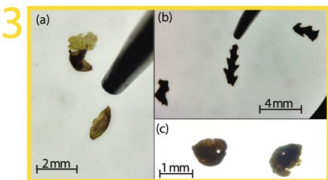
LOI results from 54-55 cm to 63-64 have been changed to match up the core stratigraphy in Core 1

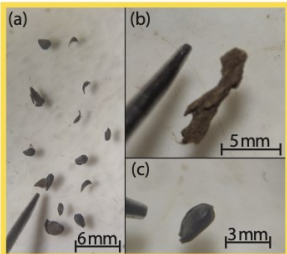
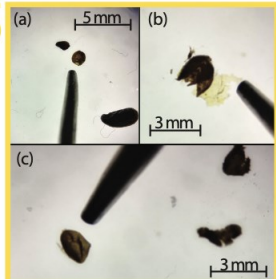
depth (cm)	59-60	60-61	61-62	62-63	63-64
LOI carbon (%)	0.00%	0.00%	0.00%	0.00%	0.00%
Prior SWLI range	200-223	200-223	200-223		
Foraminifera relative abundance					
<i>Balticammina pseudomacresens</i>	0.515	0.671	0.819	0.732	0.792
<i>Trochamminita irregularis</i>	0.009	0.033	0.024	0.038	0.007
<i>Haplophragmoides wilberti</i>	0.126	0.038	0.090	0.108	0.020
<i>Trochammin inflata</i>	0.000	0.000	0.000	0.000	0.000
<i>Jadammina macrescens</i>	0.052	0.038	0.036	0.051	0.027
<i>Miliammina fusca</i>	0.004	0.042	0.024	0.064	0.128
<i>Trochamminita salsa</i>	0.000	0.000	0.000	0.000	0.000
<i>Pseudothurammina limnetis</i>	0.000	0.000	0.000	0.000	0.000
<i>Haplophragmoides manilaensis</i>	0.000	0.000	0.000	0.000	0.000
<i>Testate amoebae</i>	0.294	0.179	0.006	0.006	0.027
Total foraminifera count per 1 cm ³	370	96	53	126	238




LOI results from 54-55 cm to 63-64 have been changed to match up the core stratigraphy in Core 1

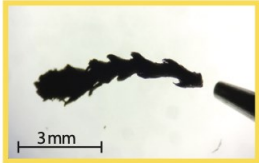
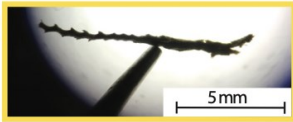
Table A.3. Bacon modelled ages for C1 including images of dates material.

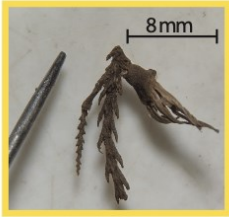
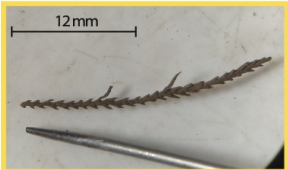
Depth (cm)	Minimum modelled age (C.E.)	maximum modelled age (C.E.)	Median modelled age (C.E.)	Mean modelled age (C.E.)	Stratigraphy	Image of radiocarbon samples
0	2018	2023	2021	2021	Peat	
1	1984	2020	2009	2007	Peat	
2	1972	2013	1993	1993	Peat	
3	1964	1997	1976	1977	Peat	
4	1960	1970	1964	1964	Peat	
5	1919	1963	1951	1948	Peat	
6	1888	1956	1932	1930	Peat	
7	1866	1946	1916	1913	Peat	
8	1847	1936	1899	1897	Peat	
9	1827	1925	1882	1880	Peat	
10	1812	1913	1867	1866	Peat	
11	1795	1900	1850	1850	Peat	
12	1781	1882	1833	1832	Peat	
13	1769	1867	1816	1817	Peat	
14	1754	1852	1799	1799	Peat	
15	1740	1834	1782	1783	Peat	
16	1729	1815	1765	1767	Peat	
17	1719	1795	1748	1750	Peat	
18	1710	1769	1730	1733	Peat	
19	1701	1751	1716	1718	Peat	Sample 1: Bulk peat sampling
20	1692	1732	1708	1708	Mud	Sample 2: Bulk peat sampling
21	1682	1721	1699	1699	Mud	
21.0001	1682	1721	1699	1699	Tsunami sand	

22	1682	1721	1699	1699	Tsunami sand	
22	1682	1721	1699	1699	Tsunami sand	
23	1682	1721	1699	1699	Tsunami sand	
24	1682	1721	1699	1699	Tsunami sand	
25	1682	1721	1699	1699	Tsunami sand	
25.000 1	1682	1721	1699	1699	Tsunami sand	
26	1671	1712	1690	1690	Peat	<p>3</p>  <p>(a) Seed casing at 27.5-28 cm, (b) three Triglochin rhizome at 27.5-28 cm, and (c) seed casing at 28.5-29 cm. Total interval sample is 27.5-29 cm. Sample weight 1 mg.</p>
27	1661	1703	1680	1681	Peat	
28	1652	1692	1669	1670	Peat	

29	1642	1670	1656	1656	Peat	<p>4</p>  <p>(a) ~5 seed fragmented seed casings, (b) Triglochin rizome, (c) Juncus balticus seed. Total sample weight 1 mg at intervals 29-29.5 cm.</p>
30	1627	1661	1646	1646	Peat	<p>5</p>  <p>(a) Seed casing at 30-30.5 cm, (b) seed casing at 31-31.5 cm, and (c) seed casing at 29.5-30 cm. Total interval sample is 29.5-31.5 cm. Sample weight 1 mg.</p>
31	1599	1653	1633	1631	Peat	
32	1579	1644	1618	1616	Peat	
33	1562	1635	1603	1601	Peat	
34	1544	1625	1586	1586	Peat	
35	1530	1613	1571	1571	Peat	
36	1514	1600	1556	1556	Peat	
37	1502	1585	1540	1541	Peat	
38	1491	1572	1525	1527	Peat	

39	1480	1558	1510	1511	Peat	<p>6</p>  <p>Triglochin rhizome at 39.5-40 cm, total weight is 6 mg.</p>
40	1468	1544	1497	1498	Peat	
41	1455	1527	1484	1486	Peat	
42	1445	1510	1472	1473	Peat	
43	1434	1495	1460	1461	Peat	
44	1426	1479	1447	1449	Peat	
45	1418	1462	1436	1437	Peat	<p>7</p>  <p>Triglochin rhizome at 45.5-46 cm, total weight is 2 mg.</p>
46	1410	1450	1428	1428	Peat	
47	1401	1442	1422	1422	Peat	
48	1387	1436	1416	1416	Peat	
49	1373	1429	1410	1410	Peat	
50	1359	1421	1405	1404	Peat	<p>8</p>  <p>Triglochin rhizome at 50.5-51 cm, total weight is 3 mg.</p>

51	1350	1416	1400	1399	Peat	10  Triglochin rhizome at 50.5-51 cm, total weight is 3 mg.
52	1344	1409	1394	1392	Peat	
53	1340	1402	1385	1383	Mud	
53.000 1	1340	1402	1385	1383	Mud	
54	1340	1402	1385	1383	Mud	
55	1340	1402	1385	1383	Mud	
56	1340	1402	1385	1383	Mud	
57	1340	1402	1385	1383	Tsunami sand	
58	1340	1402	1385	1383	Tsunami sand	
58.000 1	1340	1402	1385	1383	Tsunami sand	
59	1333	1394	1374	1372	Peat	
60	1328	1384	1363	1362	Peat	
61	1322	1373	1352	1351	Peat	9  Triglochin rhizome at 51.5-52 cm, total weight is 1 mg.

62	1314	1360	1342	1341	Peat	<p>11</p>  <p>Triglochin rhizome at 62.5-63 cm, total weight is 8 mg.</p>
63	1307	1351	1332	1331	Peat	
64	1297	1343	1321	1320	Peat	
65	1290	1334	1309	1310	Peat	
66	1283	1321	1299	1299	Peat	
67	1276	1305	1289	1289	Peat	<p>12</p>  <p>Triglochin rhizome at 67-67.5 cm, total weight is 2 mg.</p>

**Table A.4. The *Cascadia 2* training set can be found at:
<https://figshare.com/account/home#/projects/186118>**

Table A.5. Output data from RESLR.

Age (C.E)	Pred (m)	upr (m)	Lwr (m)	rate_pred (mm/yr)	rate_upr (mm/yr)	rate_lwr (mm/year)	CI
1351	-0.4206722	-0.601679	-0.2375558	0.50302017	-0.6210333	1.59585655	95%
1376	-0.4080246	-	-0.2429927	0.50841832	-0.533575	1.52444005	95%
		0.5711425					
1401	-0.3952263	-	-0.2471585	0.515096	-0.4561282	1.46822636	95%
		0.5425318					
1426	-0.3822587	-	-0.2463557	0.52189059	-0.3718354	1.3614679	95%
		0.5166557					
1451	-0.3691141	-0.494227	-0.245479	0.52927025	-0.2694614	1.30389323	95%
1476	-0.355781	-	-0.2408836	0.53691911	-0.2018387	1.22848919	95%
		0.4716033					
1501	-0.3422548	-	-0.233347	0.54475589	-0.1105644	1.17573534	95%
		0.4497774					
1526	-0.3285241	-	-0.2231486	0.55326167	-0.0500061	1.1327539	95%
		0.4337616					
1551	-0.3145787	-0.417433	-0.2127831	0.56190442	0.01843339	1.09231352	95%
1576	-0.3004118	-	-0.2013563	0.57091695	0.06225464	1.05864207	95%
		0.4021137					
1601	-0.2860246	-	-0.18956	0.57957498	0.09611728	1.04029335	95%
		0.3876448					
1626	-0.2714093	-	-0.1761809	0.58916221	0.12972423	1.03477321	95%
		0.3712838					
1651	-0.256557	-	-0.1618682	0.59845922	0.15520018	1.03834176	95%
		0.3554685					
1676	-0.2414699	-	-0.1473453	0.6079891	0.17213959	1.04275503	95%
		0.3385582					
1701	-0.2261442	-	-0.1340658	0.61743477	0.18825018	1.04522565	95%
		0.3229009					
1726	-0.2105901	-	-0.1171618	0.62628623	0.19537334	1.06047523	95%
		0.3070442					
1751	-0.1948108	-0.291443	-0.1037854	0.63555171	0.18614431	1.09093455	95%
1776	-0.178798	-	-0.0884482	0.64484133	0.16836376	1.13232877	95%
		0.2750036					
1801	-0.1625535	-	-0.0714781	0.65404145	0.15603122	1.18631125	95%
		0.2599147					
1826	-0.1460866	-0.245644	-0.0499729	0.66261222	0.13201179	1.25953879	95%
1851	-0.1294136	-	-0.0291635	0.67059667	0.09638749	1.33213611	95%
		0.2310553					
1876	-0.1125413	-0.217773	-0.0095173	0.67850695	0.06856587	1.40773831	95%
1901	-0.0954786	-	0.01554878	0.68581453	0.0258243	1.48092354	95%
		0.2062092					
1926	-0.0782357	-	0.0420751	0.6928898	-0.0121322	1.57224286	95%
		0.1964639					
1951	-0.0608279	-	0.07267169	0.69891174	-0.0669368	1.68518096	95%
		0.1903566					
1976	-0.0432888	-0.18391	0.10571601	0.70344323	-0.1338797	1.78427586	95%
2043	0.00420456	-0.177939	0.21829083	0.71265672	-0.2814971	2.06112214	95%

Appendix B.

Supporting Code

B.1 Partitioning Around Medoids and Detrended Correspondence Analysis statistical analysis of modern foraminifera

The code used to compute Partitioning Around Medoids (PAM), and Detrended Correspondence Analysis (DCA) was used in RStudio (version 22.12.0+353), with the following code used for Transect 1:

#PAM analysis for transect 1

#Load packages

```
library(cluster)
library(factoextra)
library(tidyverse)
library(vegan)
library(plyr)
library(vegan)
library(ggplot2)
```

#Determine the number of clusters for transect 1

#x is the Excel file containing the relative abundance of foraminifera for all stations

```
x<-Transect1_stat[1:17,1:16]
```

```
fviz_nbclust(
  x,
  FUNcluster = pam,
  method = c("silhouette"),
  diss = NULL,
  k.max = 8,
  nboot = 100,
  verbose = interactive(),
  print.summary = TRUE,
)
```

#PAM silhouette cluster for transect 1

```
data(Transect1_stat[1:17,1:16])
pr2 <- pam(Transect1_stat[1:17,1:16],4)
str(si <- silhouette(pr2))
ssi <- summary(si)
plot(si)
```

#DCA for transect 1

```

data(Transect1_stat[1:17,1:16])
vare.dca <- decorana(Transect1_stat[1:17,1:16])
vare.dca
summary(vare.dca)
plot(vare.dca)

#Load data and call column species
species<-Transect1_stat[1:17,1:16]
elevation1<-as.data.frame(Transect1_stat$elevation)

#Run DCA of species data
ord <- decorana(species)

#plot DCA
plot(ord)
summary(ord)

ord.fit <- envfit(ord ~ Transect1_stat$elevation, data=elevation1, perm = 999)
ord.fit

si <- as.data.frame(si)

data.scores <- as.data.frame(site_scores)
data.scores$endgroup <- as.factor(pam(si$cluster, 4)$clustering)

find_hull <- function(df) df[chull(data.scores$DCA1, data.scores$DCA2), ]
hulls <- NULL
for(i in 1:length(unique(data.scores$endgroup))){
  endgroup_coords <- data.scores[data.scores$endgroup == i,]
  hull_coords <- data.frame(
    endgroup_coords[chull(endgroup_coords[endgroup_coords$endgroup == i,]$DCA1,
      endgroup_coords[endgroup_coords$endgroup == i,]$DCA2),]
  hulls <- rbind(hulls,hull_coords)
}

data.scores$numbers <- 1:length(data.scores$endgroup)

PA1_St <- c("St.1", "St.2", "St.3", "St.4", "St.5", "St.6", "St.7", "St.8", "St.9", "St.10", "St.11",
"St.12", "St.13","St.14","St.15","St.16")
PA1_Zone <- c("Tidal flat/low", "Tidal flat/low ", "Tidal flat/low ", "Tidal flat/low ", "Tidal
flat/low ", "Tidal flat/low ", "Tidal flat/low ", "High Marsh", "High Marsh", "High Marsh", "High
Marsh", "High Marsh", "High Marsh", "High Marsh", "Upland", "Upland")
data.scores$Station <- PA1_St
data.scores$Zone <- PA1_Zone
data.scores

dca <- ggplot() +
  geom_point(data=data.scores,aes(x=DCA1,y=DCA2,colour=endgroup, shape = Zone),size=3) +
  geom_text(data=data.scores,aes(x=DCA1-0.03,y=DCA2,colour=endgroup,label=Station))+
  geom_point(data=Species_score_t1,aes(x=DCA1,y=DCA2),size=4,pch=3,alpha=0.8)+
  geom_text(data=Species_score_t1,aes(x=DCA1,y=DCA2),label = Species_score_t1$Species)+

```

```
geom_polygon(data = hulls,aes(x=DCA1,y=DCA2,fill=endgroup), alpha = 0.25)+  
geom_segment(data=elevation_score1,aes(x = 0, y = 0, xend=DCA1*2,yend=DCA2*2), arrow  
= arrow(length = unit(0.3, "cm")))+  
coord_fixed()  
dca
```

```
#get rid of background
```

```
dca + theme(panel.grid.major = element_blank(), panel.grid.minor = element_blank(),  
            panel.background = element_blank(), axis.line = element_line(colour = "black"))
```

```
#End here ☺
```

B.2 Bayesian Transfer Function

The code for the Bayesian Transfer Function was developed and ran by Niamh Cahill and can be found at: Cahill N (2022). BTFR: Run the Bayesian Transfer Function. R package version 0.1.0, <https://ncahill89.github.io/BTFR/>.

B.3 Bacon Age-depth model

The code for the Bacon age-depth model was developed by Maarten Blaauw and can be found at: <https://maarten14c.github.io/>

B.4 RESLR

The code for the RESLR was developed by Maeve Upton and can be found at: <https://maeveupton.github.io/reslr/>

RESLR was used in RStudio (version 22.12.0+353), with the following code: